Evaluation of the Reduction Roast – Magnetic Separation Process to Upgrade Low-Grade Ferruginous Manganese Ore Fines

by

Yathil Matabadal

Dissertation submitted in partial fulfilment

of the requirements for the degree

of

Master of Engineering

(Metallurgical Engineering)

Supervised by

Dr R Cromarty

November 2022

Department of Material Science and Metallurgical Engineering

University of Pretoria

Preface

This thesis is submitted to the University of Pretoria as a partial fulfilment of the requirements of the degree Master of Engineering. The work was mainly performed in the department of materials science and metallurgical engineering at the University of Pretoria under the supervision of Dr R. Cromarty, during the period of January to November 2022.

This project was made possible due to financial support from African Rainbow Minerals (ARM) – an industrial research partner.

Ore samples were obtained from the Assmang Nchwaning Manganese Mine in the Northern Cape province of South Africa.

The main aim of this work was to investigate the feasibility of the reduction roast-magnetic separation process as a method to upgrade low grade ferruginous manganese ore fines from the Nchwaning mine to obtain a product suitable for FeMn production.

Acknowledgements

During this project, I have been lucky enough to meet many great people who deserve to be acknowledged. Firstly, I would like to thank my supervisor, Dr Robert Cromarty for the opportunity to pursue this degree and for the countless insightful conversations and pieces of advice. I would also like to thank Mr Dirk Odendall for all the help with the experimental portion of the work.

I have enjoyed my time in the metallurgical engineering department and have met many people whom I consider friends rather than colleagues. I am appreciative of the kindness shown to me over the years. I would also like to thank my office mates, Mbongeni, Victoria and Bafedile for the interesting conversations on useful and not so useful things.

I would also like to thank my parents, Dhinesh and Shamila, for their constant support and motivation. Finally, I would like to thank Yalsha for always being patient, understanding and my biggest support.

Abstract

Manganese is an important raw material in many industries, such as the steel, non-ferrous and battery industries. Manganese ores are typically mined and are then fed to submerged arc furnaces where a manganese ferroalloy, the most common form in which manganese is used, is produced. For economic ferromanganese production, the ore used should have a manganese grade above 40% and a Mn/Fe ratio greater than 7,5. With the increase demand for manganese in recent years, resources for high grade manganese ores are gradually being depleted. In order to deal with the demand, it has now become imperative to make use of lower grade manganese ores which have historically been dumped due to selective mining of higher-grade ores. Many processes have previously been investigated in order to upgrade these manganese ores, such as physical methods, pyro- and hydrometallurgical methods. One such process that has been investigated has the ability to produce a product with a high manganese grade and Mn/Fe ratio (Elliott & Barati, 2020). This process is the reduction roast – magnetic separation process. In order to upgrade the ore, it is first subject to a carefully controlled reduction process to produce phases with different magnetic susceptibilities, such as MnO and Fe or MnO and Fe_3O_4.

This work focused on the optimization of this process for use with ores obtained from the Nchwaning mine slimes dam. Ore was obtained from the slimes dam, reduced to smaller sample sizes and was then subject to a mineralogical study. XRF and XRD was carried out on the samples, and it indicated that the Mn grade was in the region of 44 wt% Mn, which is typical of a high-grade ore. The Mn/Fe ratio, however, was found to be 3 – much lower than the 7,5 required for economic ferromanganese production. The main manganese minerals were found to be braunite I and braunite II, with a small amount of bixbyite and hausmannite present as well. The main iron mineral was hematite. A significant amount of calcite was also found.

An optimization study was carried out in the form of a central composite design, with the variables investigated being temperature and reductant ratio. The conditions were selected based on the thermodynamics of the reduction to obtain the desired phases. The reduction step for the process was carried out in a retort furnace, after which the reduced briquettes were milled and subject to a wet magnetic separation process

using a Davis Tube. The resultant magnetic and non-magnetic streams were then analysed with XRF and XRD. The results indicated that the reduction roast – magnetic separation process may not be suitable for this specific ore. The best results showed a manganese grade of the product increase from 44% to 47% and the Mn/Fe ratio increase from 3,00 to 3,72. Despite the poor observed separation, the relevant review metrics; namely the Mn/Fe ratio, the percentage Fe removed and the percentage Mn lost, were modelled and response surfaces were developed. Making use of an optimization technique known as desirability functions, it was concluded that the optimized conditions were a temperature between 850K – 900K and a CO content of the reducing gas between 30 – 35 vol%. In order to determine the reasons for the poor separation, SEM and reduction progress tests were carried out. Solid solution phase formation was evident from the SEM images, with the reduction progress tests indicating that the cause of this solid solution formation was not excessive reduction times or temperatures, but due to the mineralogy of the ore itself.

The ore was then subject to a kinetic analysis to understand the reaction mechanisms and rate controlling steps. Two separate kinetic studies were carried out, one with a CO-CO_2 gas mixture and another with a H_2-H_2O gas mixture. The use of hydrogen is growing in popularity due to the formation of water vapour rather than CO_2 in the reduction reaction. The different sets of conditions for both kinetic studies were the same as those used for the optimization study. In the case of the CO kinetic study, it was found that the Avrami model fit experimental data the best. This model describes nucleation and growth as the rate limiting step. In the case of the H_2 kinetic study, the rate limiting step was found to be activation control. A comparison between H_2 and CO reduction indicated that the former occurred at significantly higher rates and reached higher reduction extents than the latter.

Contents

List of figures

List of tables

1 Introduction

Manganese is an important raw material with a wide range of applications. A large proportion of manganese (≈90%) is used in the steel industry, mainly in the form of ferroalloys such as ferromanganese (FeMn). The increased demand for steel in developing countries is causing a rise in the demand for manganese. In addition to applications in the steel industry, manganese is also used in non-ferrous and battery industries. This increased demand for manganese comes at the same time that high grade manganese ores are being rapidly depleted.

In order to keep up with the growing demand for manganese, it has become imperative to make use of vast quantities of manganese ore fines or tailings that have been dumped due to selective mining of higher-grade manganese ores. A large proportion of these discarded ores belong to the low and medium grade categories (20 – 35% Mn and a Mn/Fe < 2.5). According to Elliott & Barati, (2020), for economic ferromanganese production, an ore with a manganese content >40% and with a Mn/Fe >7.5 is typically required.

For this reason, significant interest and commitment has been given to the beneficiation of manganese from these tailing dumps. Several advantages can be realised with the successful implementation of a beneficiation technique: namely, an alternate source of manganese ores given the current depletion of high-grade manganese ores, a reduction in mine solid wastes and effluents and a reduction in soil contamination and ground water pollution. There is also potential for a significant economic advantage in using the discarded ore.

One of the most promising methods for the upgrading of low-grade manganese ores is reduction roasting followed by magnetic separation. The main aim of this project was to optimise the reduction roast – magnetic separation process for application with low grade ferruginous manganese ore fines obtained from the slimes dam at Nchwaning mine in South Africa.

The reduction roast-magnetic separation process entails separating out phases based on differences in magnetic susceptibility. In order to induce different magnetic susceptibilities, the reduction roast stage is closely controlled (mainly in terms of

temperature and reductant ratio) to produce an Fe rich phase which is magnetic and a Mn rich phase which is not magnetic. Based on the thermodynamics of the reduction stage, a product of either elemental iron or magnetite can be produced together with MnO.

1.1 Scope of thesis

This work forms part of the research carried out in the department of metallurgical engineering and materials science in collaboration with African Rainbow Minerals (ARM).

In order to evaluate this process, several important steps were carried out. Firstly, a detailed mineralogical and chemical analysis was carried out to determine the initial grade and Mn/Fe ratio of the ore and to get an idea of the different Mn and Fe phases present. The second part involved an optimization study, in which a central composite experimental design was considered. The final part of the work included a kinetic study to understand and quantify reduction extents under different sets of conditions.

The dissertation includes the following chapters:

Chapter 2 is comprised of an in-depth review of the available literature. This includes manganese ore mineralogy, a thermodynamic review of the $Mn-O_2$ system as well as the production of ferromanganese. The main focus is on the different methods that have been developed and researched for the upgrading of manganese ores and a review of the previous work that was done on the desired process.

Chapter 3 is made up of a chemical and mineralogical study of the obtained ore. The sampling method used by the Nchwaning mine as well as the methods used to decrease sample sizes while maintaining sample integrity is discussed. The analyses done include a PSD to determine the different size fractions. X-ray diffraction (XRD) and x-ray fluorescence (XRF) were then carried out on each size fraction.

Chapter 4 contains the results of the optimization study. The chapter is broken down into several parts. Firstly, a description of the experimental design, procedure, apparatus and review metrics is given. A description on several preliminary tests is then discussed. The bulk of the chapter deals with the results of the optimization study (XRF and XRD results), calculated review metrics, development of models and

response surfaces and optimization through the use of desirability studies. Reasons for poor observed separation between Mn and Fe minerals is also given

Chapter 5 includes a kinetic analysis on the reduction process. In this chapter, reaction kinetics are described for both, CO reduction and H_2 reduction. The development of rate equations and descriptions of rate limiting steps are also given. A comparison between H_2 and CO reduction is also included.

Chapter 6 finalises the dissertation by summarising key finding and conclusions. Recommendations are also given for further work.

2 Literature review

2.1 Manganese ores

2.1.1 Manganese ore reserves

South Africa is the largest producer of manganese ore in the world. According to NS Energy, (2020), South Africa produced ± 6.2 million tonnes of ore in 2019 and this accounted for 33.5% of global manganese ore production. South Africa was then followed by Australia and China (Table 2.1).

Table 2.1 - Global manganese ore production in 2019 (NS Energy, 2020)

Country	Ore Production
South Africa	6.2 million tonnes
Australia	3 million tonnes
China	2.9 million tonnes
Gabon	1.8 million tonnes
Brazil	1 million tonnes

The "Kalahari manganese fields" is an area located approximately 700 km south-west of Johannesburg. This area contains approximately 80% of the world's manganese ore deposits (MiningTechnology, 2019). There are two main mines in operation, namely the Mamatwan mine in the south of the manganese fields and the Wessel mine in the north. A summary of the expected reserves in the Kalahari manganese fields is summarised in Table 2.2.

Table 2.2 - Estimated reserves in the Kalahari manganese fields (Bhalla, 2018)

Wessel Grade (Mt)	Mamatwan Grade (Mt)
>44% Mn = 330 Mt	38-40% Mn = 982 Mt
40-44% Mn = 30 Mt	30-38% Mn = 6284 Mt
36-40% Mn = 18 Mt	20-30% Mn = 5938 Mt
30-40% Mn (5-10% Fe) = 31 Mt	
Subtotal = 409 Mt	Subtotal = 13204 Mt
Total Reserves = 13613 Mt	

The significance of this project is due to the depletion of high-grade manganese ore reserves and the subsequent need to begin making use of lower grade manganese ores.

2.1.2 Manganese ore mineralogy

Manganese ores from the Kalahari manganese fields can be classified according to the mine the ore originated from. There are two main classifications, namely carbonate containing ore (Mamatwan-type) and high manganese and iron containing ore (Wessels-type). These different ore types have significantly different mineralogies (Coetsee, 2019). The Mamatwan-type ore is rich in carbonates such as calcites and dolomite, with the major manganese bearing mineral being braunite. The Wessels-type ore consists mainly of oxides such as hausmannite, bixbyite and hematite and also contains silicates such as braunite and braunite (II). The important manganese minerals found in these deposits is summarised in Table 2.3.

Table 2.3 - Manganese minerals typical of ores from the Kalahari manganese field

Mineral	Chemical Formula
Pyrolusite	MnO_2
Bixbyite	$(Mn,Fe)_2O_3$
Hausmannite	Mn_3O_4
Braunite	$3(Mn,Fe)_2O_3 \cdot MnSiO_3$
Braunite (II)	$7(Mn,Fe)_2O_3 \cdot CaSiO_3$
Cryptomelane	KMn_8O_{16}

Due to the solubility of manganese and iron, they are often in solid solution with each other. This means that some Fe atoms may replace or substitute manganese atoms in certain minerals. This is the cause of minerals like bixbyite having a chemical formula of $(Mn,Fe)_2O_3$ (Larssen, 2020).

2.1.3 Manganese ore grading

There are several different grading values used for manganese ores. The classification used by the Department of Mineral Resources in South Africa describes metallurgical grade manganese ore having a Mn content >35%, ferruginous manganese ore having a Mn content between 15% and 35% and manganiferrous ore having a manganese

content between 5% and 10%. The ore can also be classified as high grade (>44% Mn), medium grade (30-44% Mn) and low grade (<30% Mn) (Ratshomo, 2011).

According to Elliott & Barati, (2020), the grading of manganese ores for ferromanganese production is as follows: high grade ore (>44% Mn), medium grade ore (40-44% Mn) and low grade ore (<40% Mn). The ideal Mn/Fe ratio for ferromanganese production was also stated as 7.5.

For the purposes of this work, the aim is to upgrade the low-grade ore such that it can be suitable for ferromanganese production. Thus, a manganese grade >40% with a Mn/Fe ratio ≈ 7.5 was considered the baseline for the success of the selected upgrading method.

In terms of pricing of different grades of manganese ores, a spot-price from mid-2015 for low grade (36-39% Mn) manganese ore was approximately 94 USD/t and was approximately 141 USD/t for high grade manganese ore (>44% Mn). This means that in order to upgrade a 36% Mn ore to 44% Mn requires a Mn recovery of ±80% to be competitive with natural high-grade ores.

2.1.4 Uses of manganese ore

Manganese is an important industrial metal, with a wide variety of applications. It is consumed in large quantities by all industrialised nations in the world. It is important due to its desirable properties, which include: desulphurizing, deoxidizing and alloying (Bradley et al., 2013). Currently the steel industry is responsible for 85 – 90% of manganese consumption world-wide (W. Zhang & Cheng, 2007). Manganese is also an important alloying element, primarily in the steel industry, but also in the aluminium industry. Other forms of manganese, such as oxides (MnO, Υ-MnO_2) have applications in the battery industry (Singh et al., 2020). Figure 2.1 summarises the industrial uses for manganese (Wellbeloved et al., 2000).
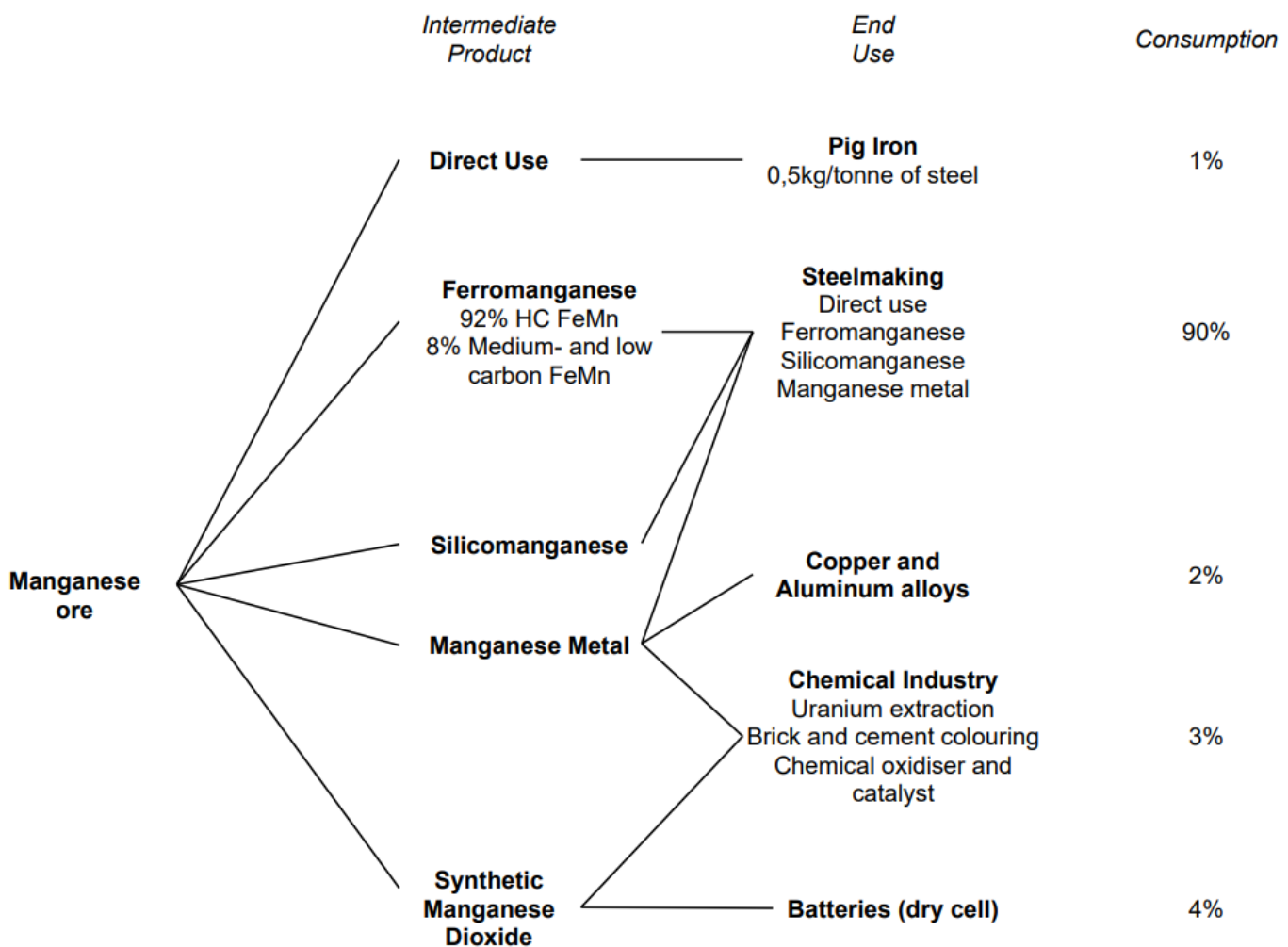
Figure 2.1 - Overview of the industrial uses of manganese (adapted from Wellbeloved et al., 2000)

From Figure 2.1 it is evident that most manganese ores are used to produce ferromanganese and silicomanganese, which are then used in the iron and steel industry.

2.2 The Mn-O_2 system

The range of existing manganese oxides are as follows: Mn_2O_7, MnO_2, Mn_5O_8, Mn_2O_3, Mn_3O_4 and MnO. Of these oxides; MnO_2, Mn_2O_3, Mn_3O_4 and MnO are typically found naturally in manganese ores (Wellbeloved et al., 2000). Wellbeloved et al., (2000) also discussed the crystal structures of the naturally occurring manganese oxides. It was found that MnO_2 occurs as a stable β-MnO_2 under normal conditions. Mn_2O_3 is present as a cubic crystal structure at temperatures above 20 °C. At atmospheric pressure, Mn_3O_4 exists as a tetragonal structure, but undergoes a transformation to a cubic structure at 1170 °C. MnO, which is a nonstoichiometric compound, exists solely with a stable cubic crystal structure. The presence of MnO as a single phase can be depicted by the XRD pattern, in Figure 2.2, of a sample of reduced manganese ore from work by De Villiers, (2020). The different MnO peaks are due to different orientations of MnO within the sample.
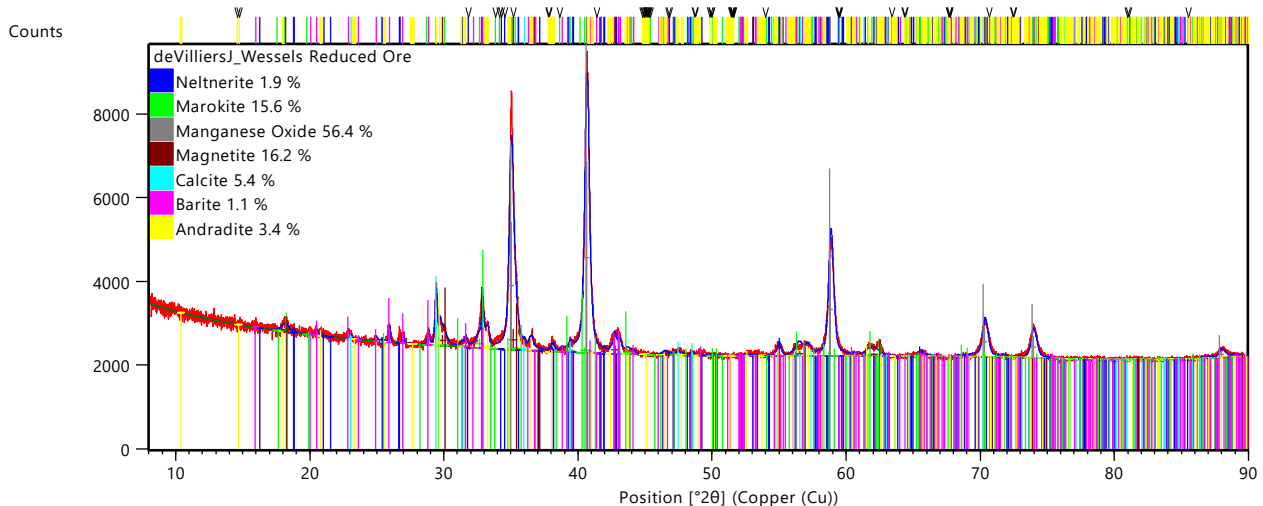
Figure 2.2 - XRD pattern of reduced manganese ore with phase quantities indicated (De Villiers, 2020) *(Used with permission)*

In order to fully understand the manganese-O_2 system, the analysis of the thermal dissociation of the naturally occurring oxides must be looked into. The chemical equations and the corresponding enthalpy values for this thermal dissociation is given below (these equations correspond with the chemical equations used in Figure 2.3):

$$4MnO_2 \rightleftharpoons 2Mn_2O_3 + O_2, \Delta H_{298} = 166.0 \text{ kJ} \qquad 2.1$$

$$6Mn_2O_3 \rightleftharpoons 4Mn_3O_4 + O_2, \Delta H_{298} = 64.8 \text{ kJ} \qquad 2.2$$

$$2Mn_3O_4 \rightleftharpoons 6MnO + O_2, \Delta H_{298} = 450.5 \text{ kJ} \qquad 2.3$$

$$2MnO \rightleftharpoons 2Mn + O_2, \Delta H_{298} = 384 \text{ kJ} \qquad 2.4$$
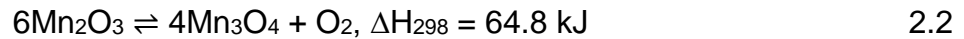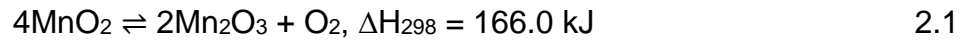
The oxygen partial pressures of these reactions are given as a function of temperature in Figure 2.3. This diagram shows the stability of different manganese oxides at different oxygen partial pressures and temperatures. According to the diagram, higher manganese oxides can be reduced to MnO under atmospheric conditions, however only at extremely high temperatures. The addition of a reductant facilitates this reduction reaction at lower temperatures. According to the diagram, MnO_2 decomposes at a temperature in the order of 750 K and Mn_2O_3 decomposes at approximately 1600 K.
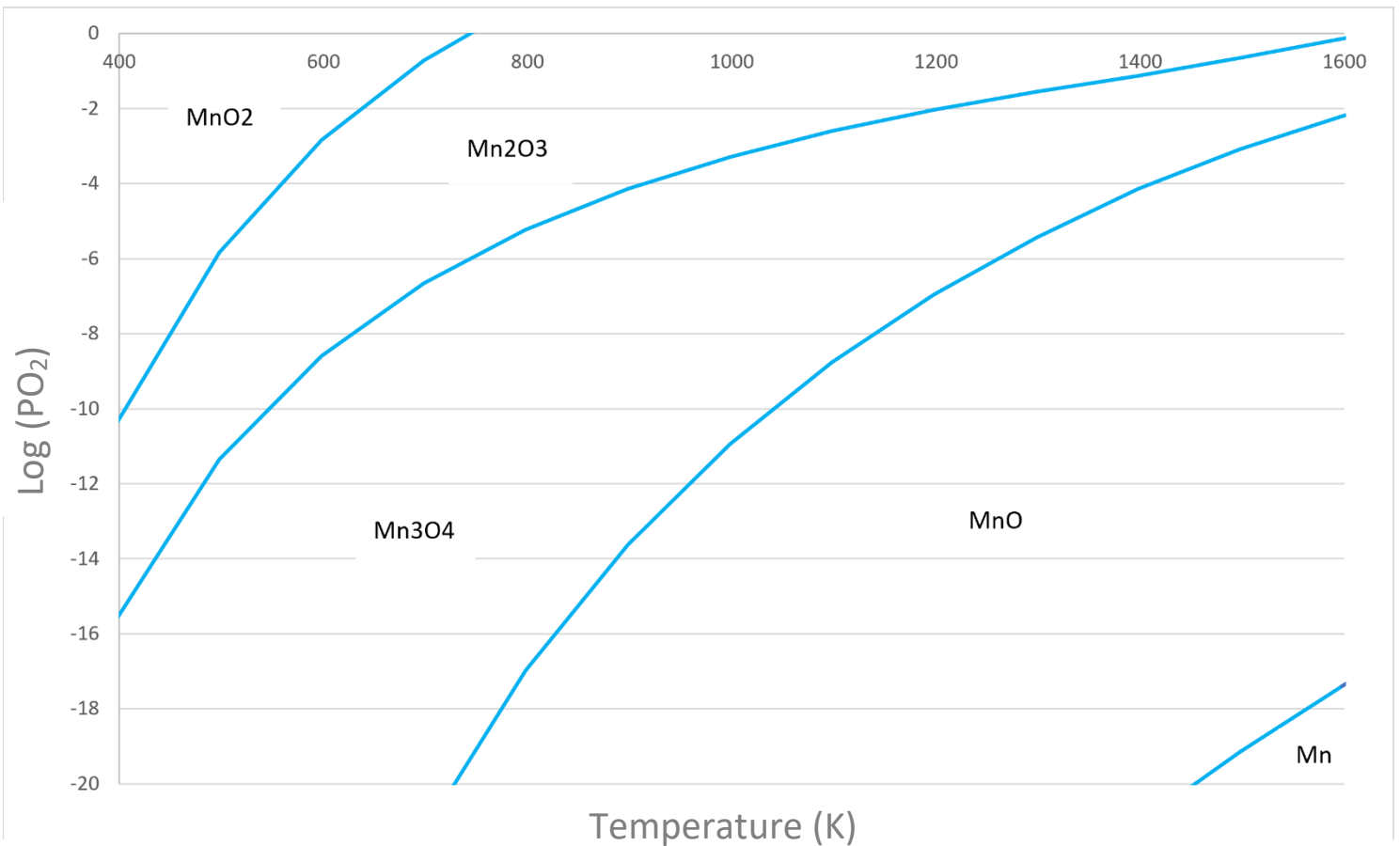
Figure 2.3 - Calculated equilibrium relationships of the Mn-O_2 system. Data obtained from FactSage version 7.3 with databases FToxid and FactPS

The temperatures obtained from this diagram (Figure 2.3) are significantly higher than those obtained from the diagram presented by Larssen, (2020). It is believed to be due to the different databases used to obtain equilibrium constants (for this work, all thermodynamic data was obtained from Factsage, whereas Larssen obtained thermodynamic data from HSC 9). For the decomposition of Mn_3O_4 at atmospheric pressure, a reductant will be required.

2.3 Production of ferromanganese

Manganese alloys, such as ferromanganese, are typically produced in submerged arc furnace made up of 3 triangularly oriented Soderbergh electrodes. The furnace can be broken down into two main zones, known as the pre-reduction zone and the coke bed zone, as depicted in Figure 2.4. (Larssen, 2020).
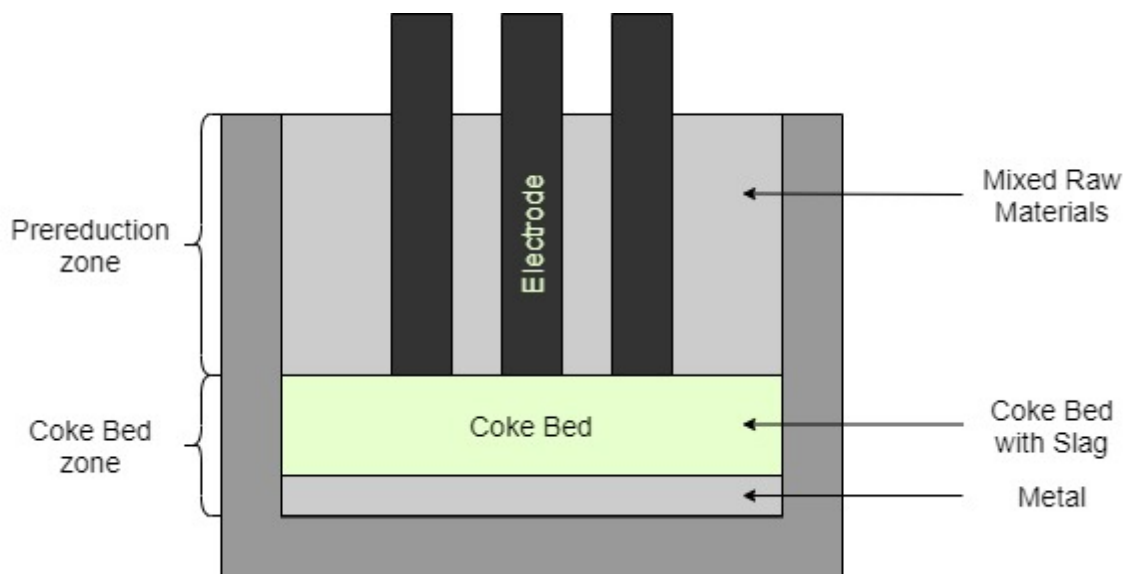
Figure 2.4 - Schematic representation of a submerged arc furnace used to process manganese ores

In the pre-reduction zone, there is no melting and the main aim in this zone is to reduce higher manganese and iron oxides to MnO and metallic iron respectively. The decomposition of carbonates and the dehydration of the ore also takes place in this zone. As the feed material continues to move towards the lower parts of the furnace, melting will begin, and this will result in the formation of a slag layer. This takes place in the coke bed zone. The MnO and SiO_2 from the slag will react with carbon from the coke and be reduced to Mn and Si respectively(Larssen, 2020). The resultant product is either HC FeMn (high carbon ferromanganese) or SiMn (silico manganese), depending on the Si content.

The raw materials fed into the furnace include manganese ores, agglomerated manganese ores such as sinters or briquettes, coke which acts as a reductant and fluxes such as SiO_2. The typical manganese ore grade required for the production of ferromanganese is >40% Mn with a Mn/Fe ratio > 7.5 (Elliott & Barati, 2020).

2.4 Methods to upgrade manganese ores

A significant amount of work has been done and can be found in literature regarding the upgrading of manganese ores. A large variety of processes such as physical beneficiation (gravity separation for example), chemical beneficiation (both hydrometallurgical and pyrometallurgical) and physio-chemical combined processes have been previously evaluated. Each process can be quantified in terms of the achieved manganese recovery, manganese grade of the product and the percentage of iron removed from the product (Mn/Fe ratio).

Significant variability in ore grades and mineralogical characteristics make it difficult to select a proper beneficiation process. Finding the most suitable beneficiation process therefore depends on several key factors. Firstly, the preferred process would depend heavily on the type of manganese ore (oxide, siliceous or carbonate ore), the associated gangue minerals and the degree of liberation of manganese from the gangue minerals. In addition, the process must be cost efficient.

2.4.1 Physical processes

Physical separation processes are commonly used as an initial process in the upgrading of manganese ores. Several physical processes, such as gravity separation, flotation and magnetic separation have been evaluated (Liu et al., 2019).

Gravity separation

Gravity separation works on the principal of density differences between the different minerals in the manganese ore. A list of the densities of common manganese and iron minerals in given in Table 2.4.

Table 2.4 - Densities of common manganese and iron minerals (Liu et al., 2019)

Mineral name	Mineral composition	Density (kg/m³)
Pyrolusite	MnO_2	4700 – 4800
Bixbyite	Mn_2O_3	4900
Hausmannite	Mn_3O_4	4700 – 4800
Braunite I	$3(Mn,Fe)_2O_3.MnSiO_3$	4700 – 5000
Hematite	Fe_2O_3	4900 – 5300
Magnetite	Fe_3O_4	4900 – 5200
Siderite	$FeCO_3$	3700 - 4000

The evaluation of the densities of the common manganese and iron minerals indicate that they are very similar and thus, gravity separation has been found to be an inefficient beneficiation process. A similar conclusion was reached in review papers by Singh et al., (2020). Elliott & Barati, (2020) found that gravity separation may only be useful for the removal of free silica (density – 2650 kg/m³).

Other physical processes

Other physical processes such as flotation and magnetic separation have also been evaluated. According to Singh et al., (2020), flotation of siliceous manganese ores is not a feasible solution. Flotation of oxide manganese ores can be carried out to enhance the grade of the ore by removing clay and other gangue minerals. The removal of iron, however, is difficult. There was a significant amount of interest in the flotation of carbonate manganese ores however, due to chemical association of gangue minerals and low selectivity of carbonate gangue minerals, this process does not produce high grade manganese ore. A study on the efficacy of magnetic separation (without any prior ore treatment) was carried out by Mpho et al., (2013). A 2-stage magnetic separation process was developed, and it was found that the product grade was similar to the feed grade. Due to poor Mn separation and low Mn/Fe ratios, it was concluded that the use of magnetic separation without any ore pre-treatment is not a feasible approach.

2.4.2 Pyrometallurgical processes

Mn-rich slag smelting

This process is the major pyrometallurgical process employed to separate manganese and iron from ferruginous manganese ores. Some advantages of this process include good adaptability with regards to raw materials. This method can also handle large quantities of ore and is highly efficient. Some disadvantages associated with this process are the environmental concerns (large amounts of pollution produced) and the fact that the process is energy and capital intensive.

The separation mechanism in this process is the difference in fusibility between molten iron and the manganese silicate slag that forms. This high temperature smelting process is typically carried out at a temperature range of 1250°C – 1550°C and in either a blast furnace or electric arc furnace. The main smelting furnaces for this process are small blast furnaces with a volume of 9-60 m^3 (Liu et al., 2019).

In the reduction zone of this process, zinc and phosphorus oxides are reduced to their elemental forms. They then form vapours and exit the furnace via the upward gas flow. MnO_2 in the reduction zone is reduced to MnO, which then reacts with SiO_2 to form a Mn-rich slag ($MnO.SiO_2$). Iron oxides and other impurities, such as PbO/Ag_2O, etc., are reduced to their metallic forms. Density differences between the Mn-rich slag and the iron melt allow them to be separated. The Mn-rich slag produced can contain 30-40% manganese and have a Mn/Fe ratio between 10-40. This means that the Mn-rich slag is a suitable raw material for ferromanganese production (Ahmed et al., 2014; El-Faramawy et al., 2004). A plant trial in a 13 m^3 blast furnace was carried out by the "Citic Dameng Ming Industries Limited Company." The results of this plant trial are given in Table 2.5.

Table 2.5 - Results of a plant trial using the Mn-rich slag upgrading method (Liu et al., 2019)

Batch No.	Chemical composition of feed (wt%)					Chemical composition of Mn-rich slag					Reco-very of Mn	Coke consumpt ion (t/t$_{slag}$)
	Mn	Fe	Al$_2$O$_3$	SiO$_2$	Mn/Fe	Mn	Fe	Al$_2$O$_3$	SiO$_2$	Mn/Fe		
1	18.1	32.5	4.6	13.9	0.56	39.5	2.3	11.2	28.6	16.9	95.9	0.7-0.8
2	20.1	30.9	4.4	13.2	0.65	41.3	1.1	10.9	26.3	37.2	92.37	0.7-0.8
3	22.1	29.3	4.1	12.5	0.75	42.1	1.6	11.5	30.9	27.2	87.3	0.7-0.8

Optimization of process parameters can result in the formation of different products. For example, Singh, (2020) carried out investigations on a similar process, and through optimization of the smelting power in an electric arc furnace and slag basicity, products of synthetic manganese ore and Spiegeleisen (high manganese pig iron) could be formed.

2.4.3 Hydrometallurgical processes

Direct reduction leaching

In this type of hydrometallurgical process, the reduction of higher manganese oxides (Mn^{4+}) and the leaching of acid soluble oxides (Mn^{2+}) are done simultaneously. In order to facilitate this reduction, reductants are added. Direct reduction leaching can be carried out with a variety of reductants, such as SO_2 or sulphate salts and even several organic agents such as saw dust and oxalic acid (Dwivedi et al., 2017). This type of process has several advantages such as the high observed recovery of manganese, which has been found to be up to 90% (Liu et al., 2019). The major drawback of this type of process is the co-leaching of iron, which acts as an impurity, with manganese. Several studies, such as those by Lui et al., (2014) and Tang et al., (2014) have found manganese recoveries as high as 90% are often accompanied by iron recoveries of as high as 80%. This leads to significant complications in the downstream purification procedure for the Mn^{2+} solution. For this reason, this type of process is typically used for manganese ores with a low iron content, therefore even with high iron recoveries, the amount of iron in solution remains low.

Other proposed reductive leaching processes which improve the selectivity between iron and manganese, such as leaching processes making use of oxalic acid and methanol are uneconomic due to the high price of the organic reductant. In addition, leaching temperatures of around 150 °C are required which means the process would also be energy intensive (W. Zhang & Cheng, 2007).

2.4.4 Physio-chemical combined processes

Carbothermic reduction roasting and magnetic separation

Carbothermic reduction roasting followed by magnetic separation is a process regarded as a highly effective route to upgrade low-grade manganese ores. The purpose of the reduction roast step is to enlarge the difference in magnetic susceptibility between the manganese oxides and the iron oxides. This is achieved by close control of the temperature and atmosphere of the reduction roast in order to obtain a product that consists of MnO, which is not magnetic, and Fe_3O_4 which is magnetic. This reduction roast product is then fed to a magnetic separation stage. The non-magnetic product from this stage, which is rich in manganese, can be used for ferromanganese production and the magnetic product, which is rich in iron, can be used for ironmaking. The reduction roasting step for this process is typically carried out in a rotary kiln at temperature ranging between 400 - 1000°C (Liu et al., 2018a)

2.5 Overview of selected process – Reduction roast followed by magnetic separation

An overview of the available methods that can be applied to upgrade low-grade manganese ores was carried out in Section 2.4. An analysis of these available methods led to the selection of the most viable method – carbothermal reduction roasting followed by magnetic separation. This method was selected based on the high potential manganese grades and Mn/Fe ratios that can be achieved in the product. This method is also not as capital and energy intensive as some of the other processes. An in-depth review of this process, including a thermodynamic analysis and analyses of past work and relevant literature is carried out in this section.

The simplified flowsheet of the reduction roast and magnetic separation process is depicted in Figure 2.5.
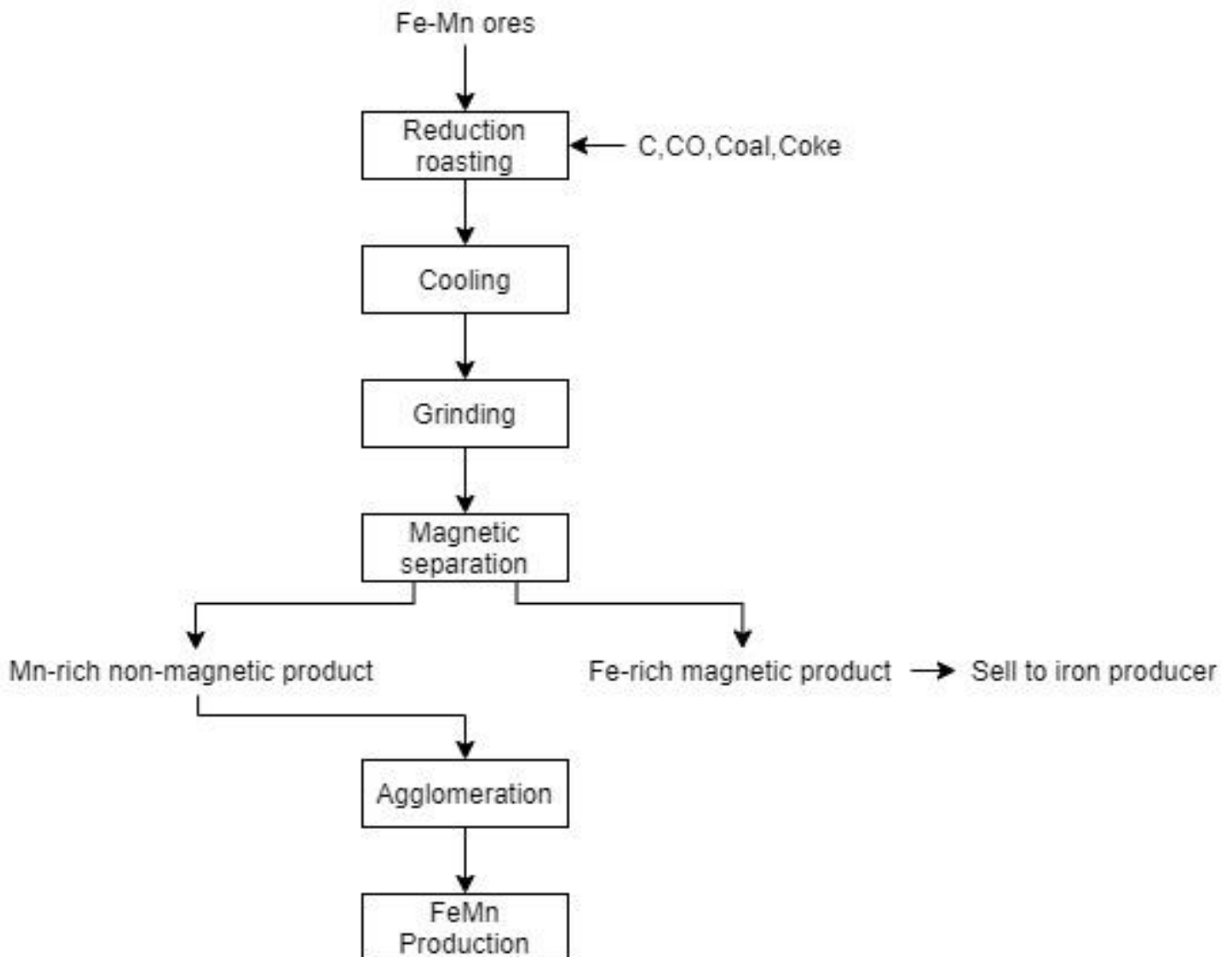
Figure 2.5 - Flowsheet of the reduction roast-magnetic separation process

Some comments regarding the flowsheet:

- A crushing stage is sometimes required prior to reduction roasting. In this project, the ores used were fine ores with a PSD of ±80% passing 300 µm. For this reason, crushing was not required.
- In order to carry out effective magnetic separation, a particle size typically -75 µm is required (Gao et al., 2019).

2.5.1 Phase requirements for magnetic separation

The purpose of the reduction roasting step in this process is to enlarge the difference in magnetic susceptibility between the different manganese and iron oxides. This is done in order to effectively separate the respective oxides from each other. A review of the magnetic susceptibilities of different manganese and iron oxides is therefore relevant in determining the preferred phases to be formed. This analysis can be found in Table 2.6.

Table 2.6 shows the magnetic susceptibilities of different manganese and iron oxides under 1 atm pressure, 25 °C and in a weak magnetic field. Other values for magnetic susceptibility for these minerals may vary to a large extent due to the strength of the applied electric field and the relative amounts of iron in these natural minerals.

Table 2.6 - Magnetic susceptibility of different manganese and iron minerals as reported by the respective studies, measured at 25°C under a weak magnetic field. The room temperature magnetism noted as F – ferromagnetic, P – paramagnetic, A – antiferromagnetic

Mineral Name	Composition	Specific magnetic susceptibility (10^{-8} m^3/kg)	Magnetism	Source
Pyrolusite	MnO_2	0.004	P	(Sant et al., 1981)
Bixbyite	$(Mn,Fe)_2O_3$	0.0002	P	(Grant et al., 1968)
Hausmannite	$(Mn,Fe)_3O_4$	0.006	P	(Kropáček et al., 1975)
Manganosite	MnO	0.01	A	(Bloch et al., 1967)
Braunite	$3(Mn,Fe)_2O_3.MnSiO_3$	0.01	P	(Meisenheimer & Cook, 1959)
Jacobsite	$MnFe_2O_4$	500	F	(Hunt et al., 1995)
Iron	Fe	50000 - 2000000	F	(Hunt et al., 1995)
Manganese	Mn	-	P	(David, 2004)
Hematite	Fe_2O_3	10-760	A/F	(Hunt et al., 1995)
Magnetite	Fe_3O_4	20000 - 110000	F	(Hunt et al., 1995)
Wustite	FeO	0.02	P	(Schrettlea et al., 2012)
Goethite	$FeO.OH$	26-280	A/F	(Hunt et al., 1995)
Limonite	$FeO.OH\ nH_2O$	66-74	P	(Hunt et al., 1995)

Description of magnetism types:

- Ferromagnetism
  - Ferromagnetic materials have a large, positive magnetic susceptibility. This means that they are strongly attracted to a magnetic field. These materials also have the ability to retain their magnetism after the external magnetic field has been removed (Wills, 2016).
- Paramagnetic
  - Paramagnetic materials have a small, positive magnetic susceptibility. This means that they are only slightly attracted to a magnetic field. These materials do not retain their magnetism after the external magnetic field is removed (Wills, 2016).
- Antiferromagnetic
  - Antiferromagnetic materials display a special behaviour in an externally applied magnetic field. At low temperatures, the material shows no response to the magnetic field. As the temperature increases, the material begins to display weak magnetism, reaching a maximum strength at the Neel temperature. Above this temperature, the magnetism decreases as the temperature increases (Chopra, 2011).

According to Elliott & Barati, (2020), as the amount of iron in a mineral increases, so does its magnetic susceptibility. For example, samples of hausmannite that contain 3-11% Fe_2O_3 have been found to be ferromagnetic, while samples that contain less than 3% Fe_2O_3 were not ferromagnetic. Additionally, due to factors such as defects and lattice impurities, natural samples of hematite have been observed to be weakly ferromagnetic, while synthetic hematite is antiferromagnetic.

Based on the work by Mpho et al., (2013) who showed that magnetic separation without any pre-treatment is not a viable upgrading method, the ideal phases would be manganosite (MnO) for manganese mineral as it is antiferromagnetic. The ideal phase for iron oxides would either be elemental iron or magnetite.

2.5.2 Extent of reduction roast

There are two possible options regarding the extent of the reduction roast. In order to obtain an iron rich magnetic stream, iron oxides need to be reduced to either magnetite

(Fe_3O_4) or elemental iron. There are advantages and disadvantages associated with either method.

If the iron oxides are reduced all the way to elemental iron (which is possible using C/CO as reductant) the advantages, described by L. Gao et al., (2020), are a high Mn and Fe recovery. The disadvantages of this method include long roasting times, high temperatures required (both of which make this method energy intensive). Other major disadvantages include excess C reporting to the non-magnetic stream which could decrease the grade of the product and the formation $Mn_{1-x}Fe_xO$ from MnO and FeO, decreasing the efficiency with which Fe and Mn are separated from each other.

If the iron oxides are partially reduced to magnetite, the only major disadvantage is that this process could be difficult to control in industry. Advantages of this process include the fact that it has decreased energy and reductant requirements. For the purposes of this study, the reduction of iron oxides to magnetite is considered. This method was considered in an attempt to reduce fuel and reductant cost and attempt to avoid the formation of undesirable phases.

Once the ore has been reduced, it can then be reground and magnetically separated in order to produce a manganese rich, non-magnetic stream and an iron rich, magnetic stream.

2.5.3 Carbothermal reduction of manganese ores

The reduction of manganese oxides in low-grade manganese ores is essential in order to enlarge the difference in magnetic susceptibility between the manganese and iron oxides. The reduction of manganese oxides to MnO is carried out with the help of a reductant such as CO. The thermodynamics of a reductant like CO is advantageous because higher manganese oxides can be reduced to MnO, but under the operational temperatures, MnO cannot be reduced to manganese metal. This fact is depicted in the Ellingham diagram shown in Figure 2.6. The diagram also indicates that at a temperature greater than about 720 K, MnO_2 would spontaneously decompose, while at temperatures greater than about 1600 K, Mn_2O_3 would spontaneously decompose. This is due to the ΔG value becoming greater than 0 at these temperatures, indicating the spontaneity of the reverse reduction reaction over the forward oxidation reaction. These temperatures are slightly higher than the values reported by (Welham, 2002). This is due to differences in thermodynamic data accessed from different databases.

Welham, (2002) carried out investigations on the MnO_2-C system using a "free energy minimisation technique" and found the following:

- Reduction of MnO_2 is likely to be a multi-stage reduction proceeding via intermediate oxides. $MnO_2 - Mn_2O_3 - Mn_3O_4 - MnO$.

The stepwise reduction of MnO_2 in the presence of CO takes the following steps:

$$2MnO_2 + CO \rightleftharpoons Mn_2O_3 + CO_2 \qquad\qquad 2.5$$

$$3Mn_2O_3 + CO \rightleftharpoons 2Mn_3O_4 + CO_2 \qquad\qquad 2.6$$

$$Mn_3O_4 + CO \rightleftharpoons 3MnO + CO_2 \qquad\qquad 2.7$$
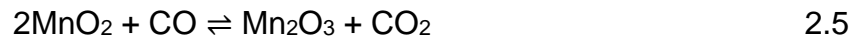
The stepwise reduction has been generally accepted as the mechanism for manganese oxide reduction, however, new work from Schanche et al., (2022), postulates the possibility that the reduction process may go from MnO_2 to MnO in a single step.
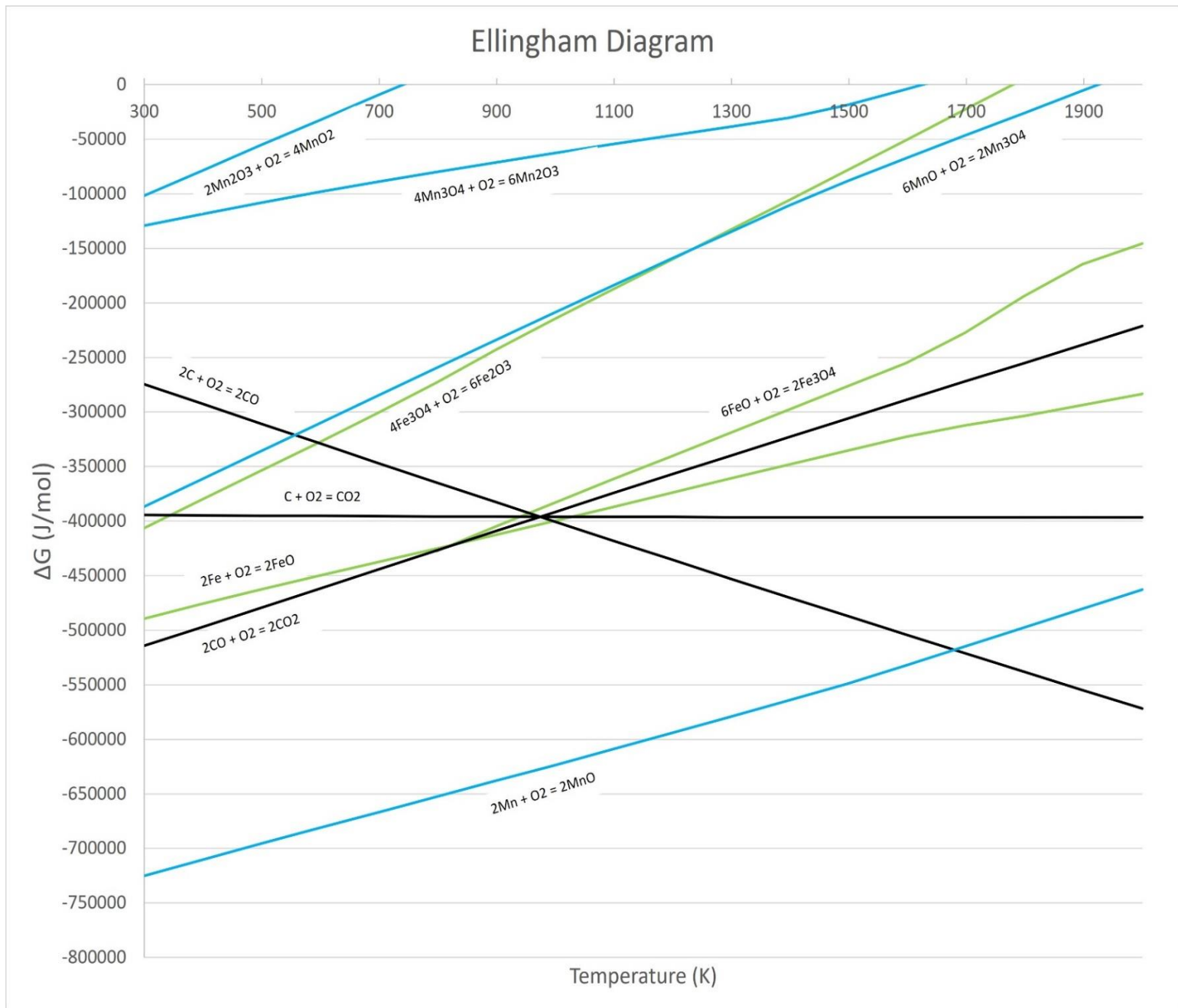
Figure 2.6 - Ellingham diagram for manganese and iron oxides. Data from FactSage version 7.3 with databases FToxid and FactPS

In the reduction roast of ferruginous manganese ores, iron and manganese oxides will simultaneously be reduced to lower oxides. When heated in a CO atmosphere, higher iron oxides undergo a stepwise reduction (similar to that of manganese oxides), according to Equations 2.8 – 2.10. Reaction 2.10 only occurs under specific conditions, displayed in Figure 2.7 (Iron Chaudron diagram).

$$3Fe_2O_3 + CO \rightleftharpoons 2Fe_3O_4 + CO_2 \qquad\qquad 2.8$$

$$Fe_3O_4 + CO \rightleftharpoons 3FeO + CO_2 \qquad\qquad 2.9$$

$$Fe_3O_4 + 4CO \rightleftharpoons 3Fe + 4CO_2 \qquad\qquad 2.10$$

$$FeO + CO \rightleftharpoons Fe + CO_2 \qquad\qquad 2.11$$

The main aim of the reduction roasting step, as discussed previously, is the reduction of higher manganese oxides to MnO, which is non-magnetic, and the reduction of higher iron oxides to Fe_3O_4 which is magnetic. The selection of relevant conditions, namely temperature, CO/CO_2 ratios and pO_2, are important to obtain the desired products. These factors can be evaluated by plotting a graph of CO/CO_2 ratio vs temperature, and a graph of pO_2 vs temperature. These graphs are shown in Figures 2.7 and 2.8 respectively.

Figure 2.7 is made up of an iron Chaudron diagram and a manganese Chaudron diagram. This diagram shows the equilibrium phases that would be present at different temperatures and at different concentrations of CO in a CO/CO_2 atmosphere at a pressure of 1 atm. The aim of the reduction roasting step is to obtain MnO and Fe_3O_4 as products. This means that the existence of an area in which these species co-exist would be ideal. In the iron Chaudron diagram, "Area A" fulfils these requirements. It is thus advisable to operate in conditions expressed in "Area A" in order to obtain the desired products.

Figure 2.8 depicts the equilibrium phases that would exist at different pO_2's and at different temperatures. This figure is made up of the $Mn-O_2$ and $Fe-O_2$ systems superimposed on each other. It can be seen that there exists a large range of temperatures and pO_2's in which MnO and Fe_3O_4 can co-exist.

An analysis of Figures 2.7 and 2.8 together with an Ellingham diagram was used to decide on potential testing conditions for the reduction roast to obtain the desired products.

Fe Chaudron Diagram

Mn Chaudron Diagram
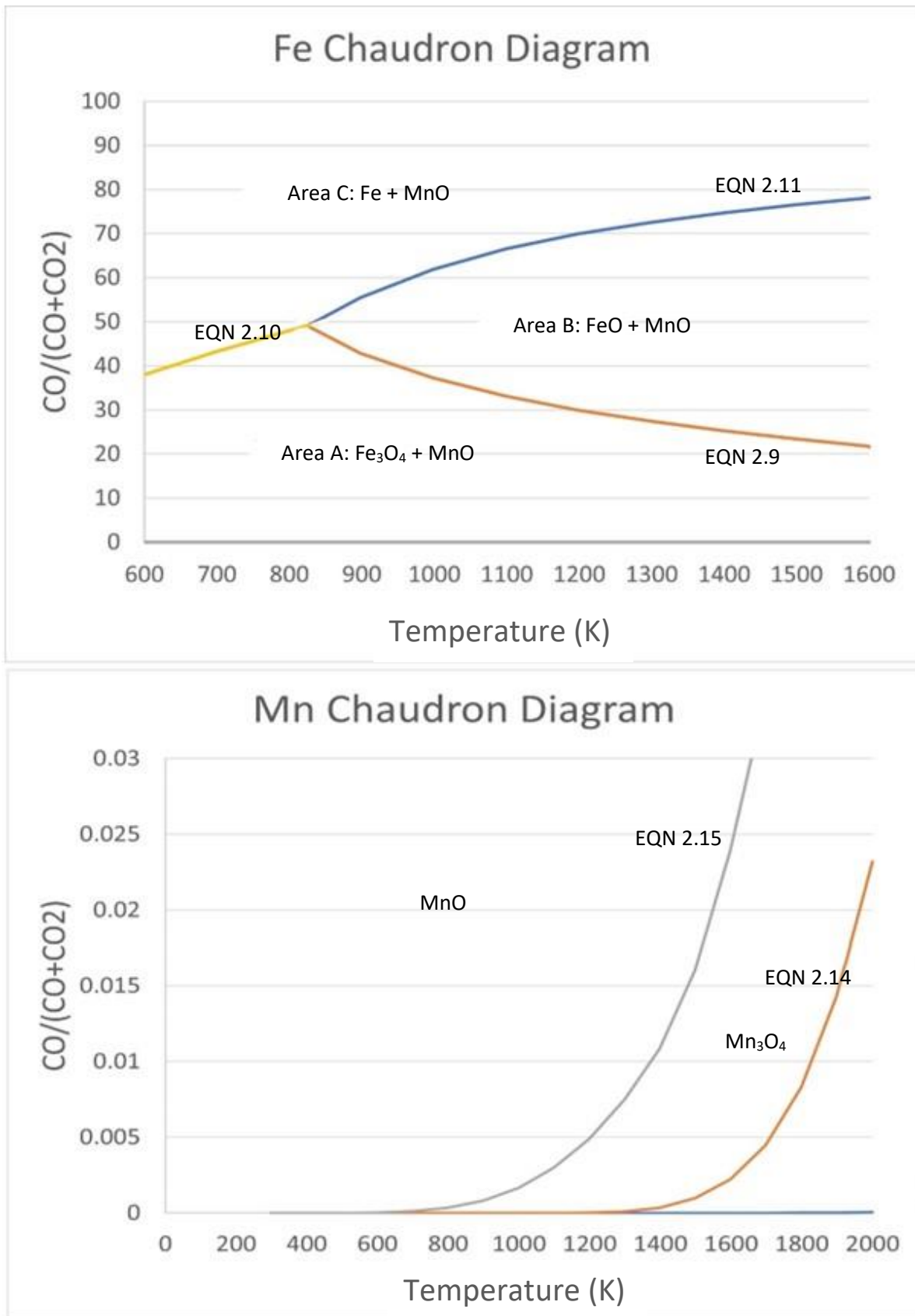
Figure 2.7 - Chaudron diagram of the Fe_2O_3 - MnO_2 - CO - CO_2 system. Data obtained from FactSage version 7.3 with databases FToxid and FactPS. Numbers of the diagram correspond to the respective chemical equations
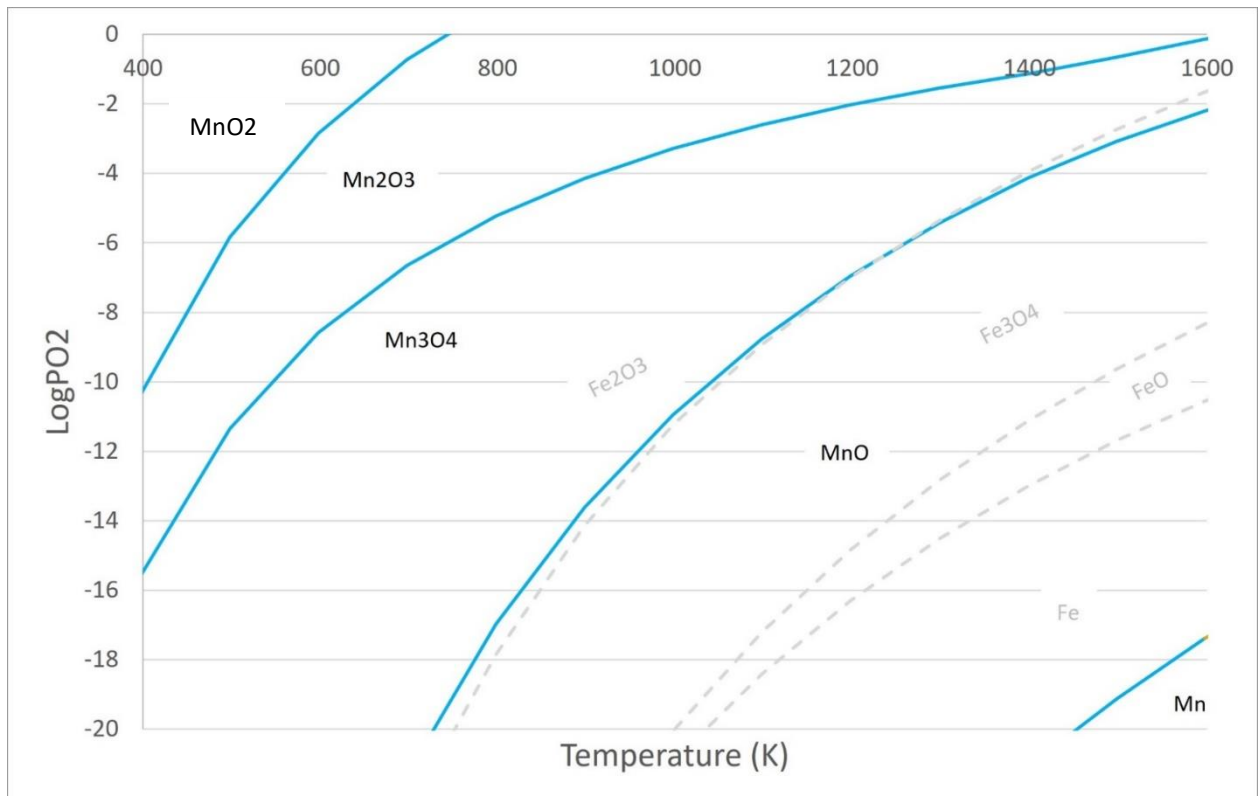
Figure 2.8 - Equilibrium relationship of the Mn-O_2 and Fe-O_2 systems superimposed on one another. Data from FactSage version 7.3 with databases FToxid and FactPS

The Boudouard reaction

The Boudouard reaction is the reduction of CO_2 to CO with solid carbon as the reductant. The Boudouard reaction is an important reaction in many metallurgical processes. The reaction is not studied directly in this project, but due to the fact that all the experimentation is going to be carried out in a CO/CO_2 atmosphere, the occurrence of the Boudouard reaction can be expected.

The stoichiometric Boudouard reaction is as follows:

$$CO_2 + C \rightleftharpoons 2CO \qquad\qquad 2.12$$

Figure 2.9 shows that most of the CO_2 present in a certain system will react with solid carbon to form carbon monoxide at temperatures above 700 °C and the atmosphere will become almost 100% CO at temperatures exceeding 900 °C. These values are only relevant under equilibrium conditions. Aderibigbe & Szekely, (1981) carried out investigations on coke reactivity in CO-CO_2 atmospheres at temperatures ranging from 850 – 1000 °C. It was found that in order for the Boudouard reaction to become kinetically significant, temperatures above 1000 °C are needed.

The impact of alkalis on the kinetics of the Boudouard reaction has been studied intensively. This is relevant to manganese ore processing as there exists manganese minerals, such as cryptomelane (KMn_8O_{16}), that may introduce alkalis such as potassium into the reduction roast. A review paper by Ishak, (2002) mentioned that the reaction rate of the Boudouard reaction is significantly increased by the presence of potassium at temperatures above 800°C. It was also shown that the influence of potassium as a catalyst has a greater impact on reaction rate than temperature, CO_2 partial pressure and particle size.
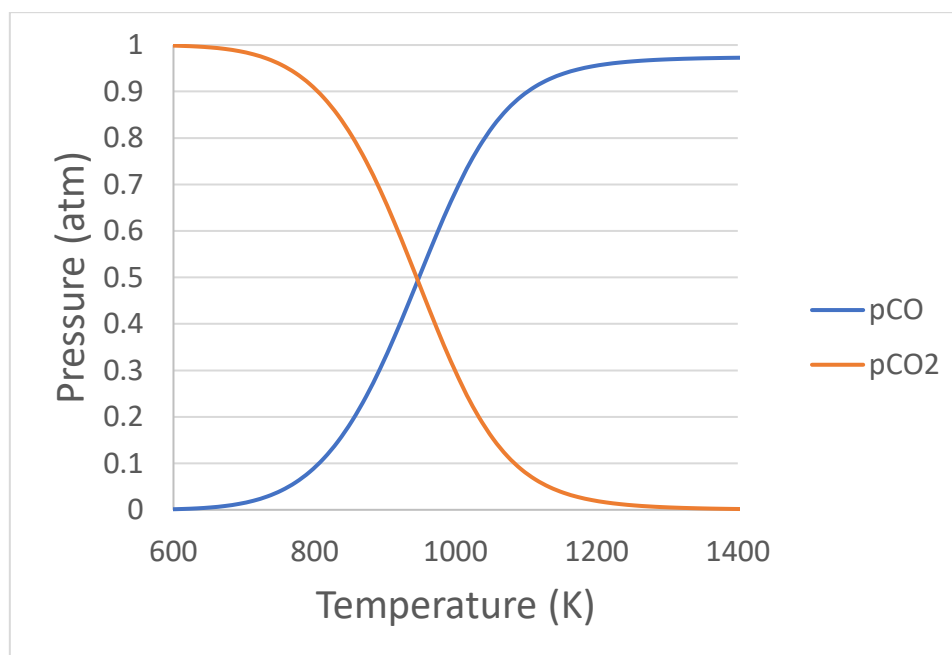
Figure 2.9 - Equilibrium CO and CO_2 partial pressures according to the Boudouard reaction. Data from FactSage version 7.3 with databases FToxid and FactPS

According to Figure 2.9, at temperatures below 700°C, the reverse Boudouard reaction is favoured, i.e., the decomposition of CO to form CO_2 and solid C. This could affect the reduction of manganese ores by carbon deposition. This occurs as solid carbon may deposit on the ore surface and cover reaction sites, thereby preventing further reduction at that specific site. A study by Towhidi & Szekely, (1983) found that carbon deposition was observed at temperatures below 900 °C during the reduction of hematite pellets in a CO, H_2, N_2 atmosphere. It was found that the deposition of carbon and reduction took place simultaneously, but the deposition of carbon was dominating at a temperature range of 500 – 600 °C. It was at these temperatures that the maximum rate of carbon deposition was observed. It was also found that compared

to a pure CO atmosphere, the presence of H_2 had a promoting effect on the carbon deposition.

2.5.4 Hydrogen reduction of manganese ores

An alternate, more environmentally friendly reductant such as hydrogen can also be used for the required application. The requirements of the reduction roast remain the same – reduction of manganese oxides to MnO and the reduction of iron oxides to Fe_3O_4. A thermodynamic analysis of the reduction of manganese and iron oxides by hydrogen was be carried out in order to determine whether the desired phases can co-exist within any range of conditions. In order to do this, iron and manganese Chaudron diagrams were drafted and are shown in Figure 2.10. The corresponding stepwise reduction of the respective manganese and iron oxides are also listed below.

Manganese reduction reactions:

$$2MnO_2 + H_2 \rightleftharpoons Mn_2O_3 + H_2O \qquad\qquad 2.13$$

$$3Mn_2O_3 + H_2 \rightleftharpoons 2Mn_3O_4 + H_2O \qquad\qquad 2.14$$

$$Mn_3O_4 + H_2 \rightleftharpoons 3MnO + H_2O \qquad\qquad 2.15$$

The iron and manganese Chaudron diagrams for hydrogen reduction appear similar to the respective Chaudron diagrams for reduction with CO. Both have a distinct area in which both target phases, MnO and Fe_3O_4 are present. The reduction of manganese ores with hydrogen will have the advantage of producing H_2O instead of CO_2.
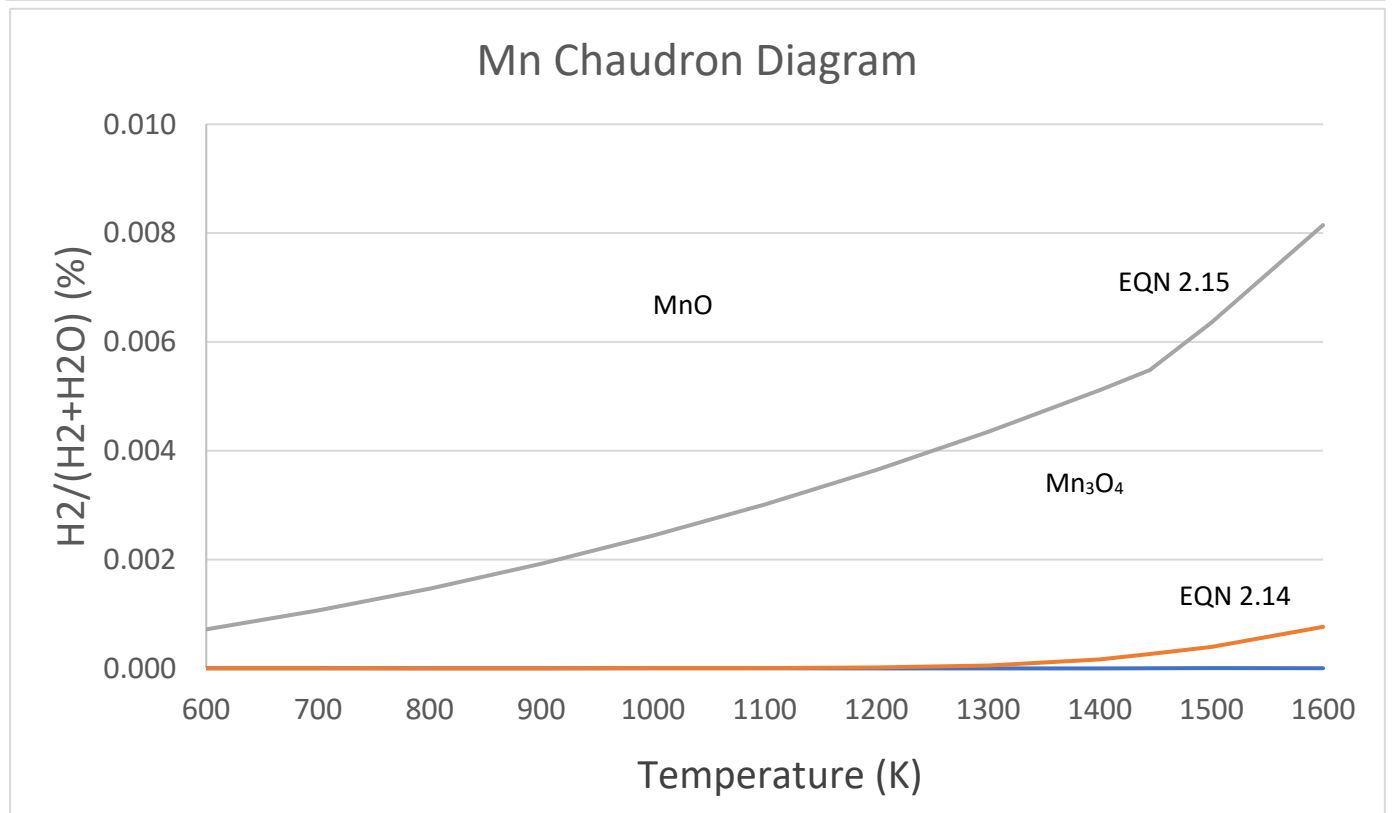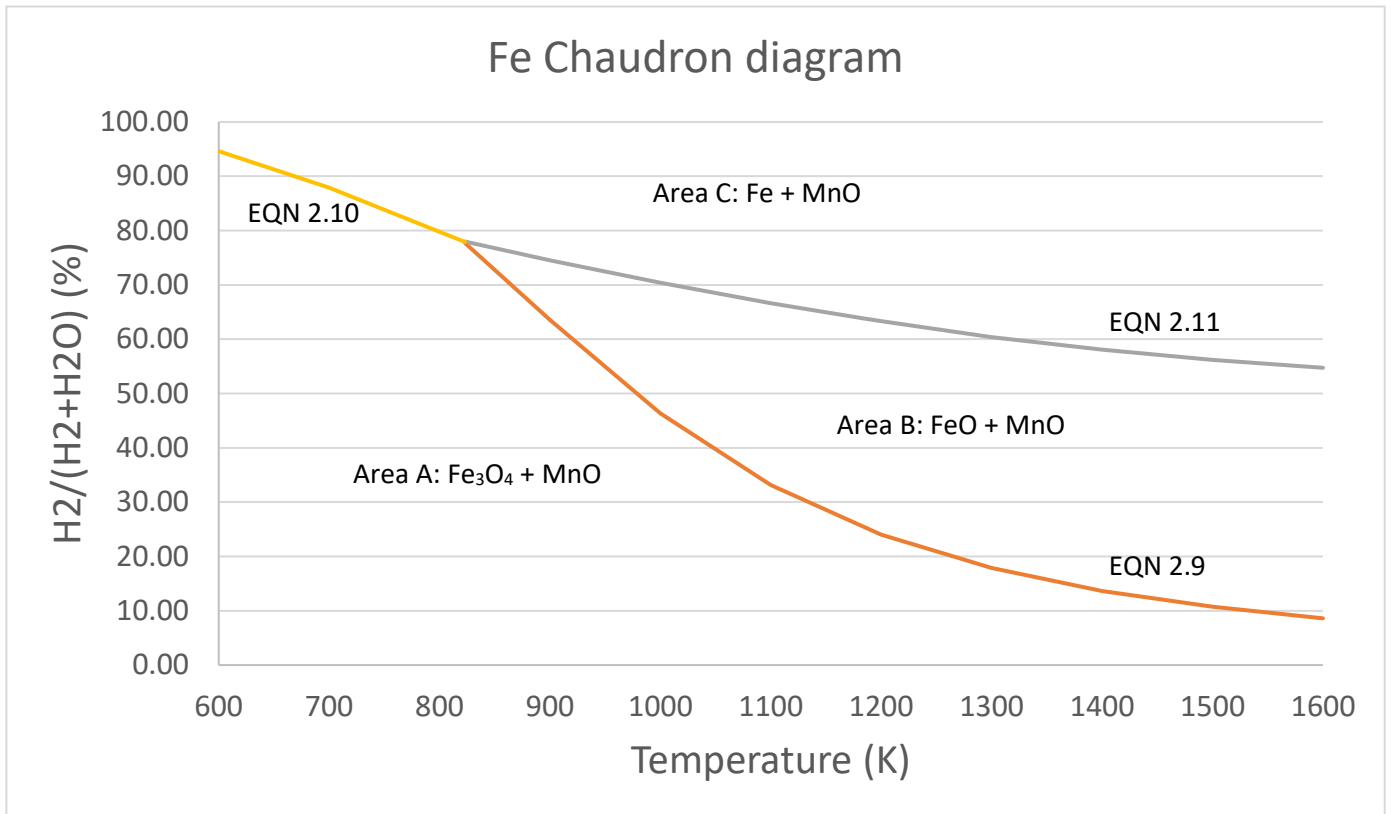
Figure 2.10 - Chaudron diagram of the MnO_2-Fe_2O_3-H_2-H_2O system. Data obtained from FactSage version 7.3 with databases FToxid and FactPS.

2.5.5 Analysis of previous work using the reduction roast-magnetic separation method

A large amount of research in this area has come in the last decade as the availability of high-grade manganese ores continues to decrease. Many attempts have been made to improve the techno-economics of the process.

A recent pilot plant study was carried out by Singh et al., (2021). The variables under investigation were the raw material feed rate (3,4,5, and 6 tph) and feed coal consumption (25%, 29%, 33%). It was found that the Mn in the ore could be increase from 30wt% to 46wt% and the Fe decreased from 27wt% to 12wt%. A Mn recovery of 70%, to the non-magnetic stream, was also achieved.

Pereira et al., (2014) carried out a calcination study on a Brazilian manganese ore. An increase in the Mn grade was found but this was attributed to the loss of CO_2 and OH during thermal decomposition of carbonated and hydrated minerals. This also caused the SiO_2 grade to increase.

Mpho et al., (2013) carried out an initial test which comprised of a two-stage magnetic separation process without any reduction roast. It was found that this process showed poor Mn separation and low Mn/Fe ratios. When a reduction roast was added prior to the magnetic separation, the ore was upgraded from 27.71% Mn and 30.90% Fe to 58.44% Mn and 2.52% Fe with a Mn recovery of 72.31%.

Y. Zhang et al., (2017) investigated the effect that the addition of Na salts ($Na_2S_2O_3$) would have on the separation efficiency of Mn and Fe. It was found that the addition of the salts increased the separation efficiency. Without the Na salt, the products from the reduction roast were metallic Fe, MnO and $(Fe,Mn)_2SiO_4$. The latter 2 reported to the non-magnetic stream. With the Na salts present, the products formed were metallic Fe, Mn_2SiO_4 and MnS. Again, the latter 2 reported to the non-magnetics, except this time, the products reporting to the non-magnetics were not associated with any Fe. This increased the separation efficiency. This result, however, may be irrelevant to the present work as in this work, the aim is to reduce to MnO and Fe_3O_4 rather than metallic iron.

L. Gao et al., (2019) carried out tests on the selective reduction of low-grade manganese ores followed by magnetic separation. The aim was to optimize operating

parameters such as temperature of the reduction roast, roasting time, manganese ore size and FC/O ratio (fixed carbon to oxygen ratio). With the optimized conditions, a manganese recovery of 71% was obtained and the resultant product had a Mn/Fe ratio of 10.85. L. Gao, Liu, Pan, et al., (2019) carried out a similar study, but went further to determine the cause of the low manganese recoveries. It was discovered that the poor separation of Fe and Mn may be related to phase transformations and intrinsic morphology evolution of composite oxides containing Mn, Fe, Al and Si. Such oxides include spinel's such as $(Fe_yMn_{1-y})Al_2O_4$, fayalite $(Fe_yMn_{2-y})SiO_4$ and a $(FeO)_x(MnO)_{1-x}$ phase. In order to overcome this poor separation, recommendations were made for reduction roast conditions. These recommendations are as follows: high temperature, short reduction times and fine Mn-Fe ores. With the optimized conditions obtained, a manganese recovery of 89.38% was obtained.

A brief overview of some of the other work done is listed in Tables 2.7 and 2.8 below:

Table 2.7 - Summary of experimental conditions and optimal conditions for previous work done employing the reduction roast-magnetic separation technique

Reference	Mn Minerals	Reductant		Time (min)		Temperature (K)		Magnetic Separator		Field Strength (T)		Separation particle size	
		Range	Optimal	Range	Optimal	Range	Optimal	Wet/Dry	Type	Range	Optimal	Range	Optimal
(Mpho et al., 2013)	Pyrolusite Todorokite	-	10%CO 90% CO2	-	480	-	1073	Wet	Davis Tube	-	1	-	0.5-1 mm
(L. Gao et al., 2018)	Bixbyite Manganite	29-67% Coal	48% Coal	120-480	360	1273-1373	1323	Wet	Davis Tube	0.025-01	0.1	-	<74 µm
(Liu et al., 2018a)	Pyrolusite Todorokite	-	10%CO 90% CO2	60-80	80	873-1273	1073	Wet	Davis Tube	-	0.1	-	d90 = 74 µm
(Huang et al., 2013)	Bixbyite	-	75% Anthracite	30-150	100	1173-1473	1373	-	Low Intensity	-	0.1881	-	<74 µm
(Kivinen et al., 2010)	Pyrolusite Manganite	-	15% Coke	-	30	1073-1273	1073	-	-	-	-	54-72% < 74 µm	d72 = 74 µm
(Y. Gao et al., 2012)	Cryptomelane Pyrolusite	0-40% CO	30% CO	0-100	60	273 - 973	873	Wet	Magnet	-	0.087	0-1000 µm	<105 µm
(Suharno et al., 2018)	Manganite	-	20% Coal	-	60	-	973	Dry	Low Intensity	-	0.5	-	-
(Singh et al., 2011)	Psilomelane Pyrolusite	10-20% Coal	15% Coal	-	30	773 - 1023	923	Wet	Davis Tube	-	0.3	-	-

Table 2.8 - Reported Mn and Fe contents of the feed and concentrate obtained under optimal conditions

Reference	Feed wt%			Concentrate wt%			
	Mn	Fe	Mn/Fe	Mn	Fe	Mn/Fe	RMn
(Mpho et al., 2013)	28	31	0.9	58	2.5	23	72
(L. Gao et al., 2018)	30	28	1.07	56	5.2	10.77	71
(Liu et al., 2018a)	23	32	0.72	48	9.3	5.16	65
(Huang et al., 2013)	39	21	1.86	61	4	15.25	74
(Kivinen et al., 2010)	35	18	1.94	54	4.7	11.49	65
(Y. Gao et al., 2012)	37	13	2.85	45	2.8	16.07	95
(Suharno et al., 2018)	21	15	1.40	28	4.6	6.09	69
(Singh et al., 2011)	32	14	2.29	42	8.4	5.00	49

2.6 Gas-solid reaction phenomena

The reduction of manganese ores can be described as a gas-solid reaction. This is because the temperatures reached in the reduction vessel (a rotary kiln for example) typically reaches a maximum of about 950 °C and thus no melting occurs. The relevant gas-solid reaction mechanisms and kinetics will therefore describe the reaction well.

Gas-solid reactions are heterogeneous in nature which means that along with chemical kinetics, the system will also be affected by geometric factors and mass transport phenomena. Gas-solid reactions also take place at a boundary and thus the mass transport (of products and reactants) to and from this boundary will be extremely important.

A typical gas-solid reaction can be expressed in the following way (Szekely et al., 1976):

$$aA(g) + bB(s) \rightleftharpoons cC(g) + dD(s) \qquad 2.16$$

There are four main steps that influence these gas-solid reactions and the magnitude of the influence of each step is dependent on the specific reaction being evaluated. The four steps are as follows:

1. Mass transfer of reactants/products from the bulk to the reaction interface.
2. Diffusion of reactants/products within the pores of the ore
3. Adsorption/desorption of reactants/products
4. Activation control

Steps 3 and 4 represent the chemical reaction rate limiting step. Therefore, the three main mechanism of gas-solid reactions are mass transfer, described by step 1, pore diffusion, described by step 2, and chemical reaction control. These steps may then be individually affected by external factors, such as nucleation of a second phase, heat transfer or structural changes of the solid (sintering for example). The analysis of gas-solid reactions is therefore complex. Often, it can be found that the rate of one of the steps is significantly lower than the other phases – this step then becomes the rate limiting step. The most common rate limiting steps in gas-solid reactions is chemical reaction control and pore diffusion control. Some scenarios of the rate limiting step

have been described by Szekely et al., (1976), for example, at low temperatures, above a certain minimum pellet size, chemical reaction control will be dominant, while at higher temperatures, diffusional resistance in the solid particle becomes the rate limiting step. Between the "low" and "high" temperature range, there is often an intermediate section in which there exists a mixed reaction control.

External mass transfer, which corresponds to step 1, can be further explained as the diffusion of gas between the reaction interface and the bulk. The rate of mass transfer from the solid to the gas per unit area of the solid and can be described by the equation below:

$$N_A = h_p(C_{As} - C_{Ao})$$
2.17

Where:

- h_p– mass transfer coefficient
- C_{As} – concentration of species A at the solid surface
- C_{Ao} – concentration of species A in the bulk

Pore diffusion, which corresponds to step 2 is described as the movement of a gas through a solid that contains pores. The modelling of the diffusion of a gas through a solid is significantly more complex than the modelling of the diffusion of a gas through a liquid. This is because the available area for diffusion in a solid varies according to the structure of the pores within the solid. This may make the diffusion path more or less tortuous. The flow of a gaseous specie in solid can be described as:

$$N_A = -D_{eff}\Delta C_A$$
2.18

Where:

- D_{eff} – effective diffusivity
- ΔC_A – concentration gradient

The effective diffusivity is a combination of the effects of two diffusion mechanisms, namely Knudsen diffusion and molecular diffusion. Molecular diffusion relates to diffusion in larger pores whereas Knudsen diffusion relates to diffusion in smaller pores. The effective diffusion can be calculated from the following equation:

$$\frac{1}{D_{eff}} = \left(\frac{1}{D_{AB,eff}} + \frac{1}{D_{A,K}}\right)$$
2.19

Where:

- $D_{AB,eff}$ – effective molecular diffusivity
- $D_{A,K}$ – Knudsen diffusivity

Chemical reaction control describes steps 3 and 4 and includes considerations regarding the kinetics of the reaction surface as well as the adsorption, desorption and reaction between species. The general rate equation with reference to the typical gas-solid reaction (equation 2.16) can be described as follows (solid activities assumed to be unity):

$$r_A = k_c \left(C_a^m - \frac{C_c^p}{K} \right) \qquad 2.20$$

Where:

- k_C – chemical rate constant
- K – equilibrium constant
- C_a and C_C – concentrations of reactant and product gasses
- m and p – reaction orders

2.7 Kinetic Model

The determination of suitable kinetic models to use for gas-solid reactions has been carried out in great detail, and as such there are several different models. The selection of a suitable model – which can accurately depict experimental conditions, therefore relies on the type of system being studied. Gas-solid reaction models typically fall withing 3 main categories (Larssen, 2020):

- A model in which the solid is non-porous,
- A model in which the solid is porous, and
- A model in which the solid is made up of many non-porous grains/particles.

The most commonly used model for a gas-solid reaction assumes that the initial solid is non-porous, and this model is the shrinking core model. As with most mathematical models, the shrinking core model makes several assumptions and has some limitations, namely:

- Solid particle with no porosity
- Isothermal conditions

- The model assumes that the reaction is first order with respect to gaseous reactants, and
- The transportation of gasses (both product gasses and reactant gasses) is assumed to occur via equimolar diffusion.

The shrinking core model takes into consideration the three steps of gas-solid reactions, namely external mass transfer, pore diffusion and chemical reaction control. The general expression for the shrinking core model, taking these 3 steps into consideration is as follows (Szekely et al., 1976):

$$t^* = g_{F_p}(X) + \sigma_s^2 \left(p_{F_p}(X) + \frac{4X}{Sh^*} \right)$$ 2.21

Where:

- t^* - dimensionless reaction time ($t^* = 1$ for full conversion)
- X – conversion
- F_p – shape factor (F_p = 1 for a slab, 2 for a long cylinder and 3 for a sphere)
- g – reaction model for chemical reaction
- σ_s^2 – shrinking core modulus (gives the ratio between the influence of the chemical reaction vs the influence of mass transfer)

In order to obtain the specific reaction time, t, from Equation 2.21, the following equation must be used. This equation assumes that the resistance offered by mass transfer through the boundary layer is negligible. The equation can be used for a spherical particle:

$$t = \frac{\rho_s r_p}{k_c} \cdot \frac{1}{C_{CO}^0} g(X) + \frac{\rho_s r_p^2}{6 D_E C_{CO}^0} p(X)$$ 2.22

Where:

- ρ – particle density
- r – particle radius
- k_c – chemical rate constant
- C^0 – bulk gas composition
- $g(X)$ – reaction model for chemical reaction with contracting volume
- D_E – diffusion constant
- $p(X)$ – reaction model for 3D diffusion

While the application of this model remains the most common, researchers have applied different models to gas-solid reactions. A minor overview of available literature is given in Table 2.9.

Table 2.9 - Brief overview of kinetic models used by previous researchers for manganese ore reduction

Material	Gas	Solid Carbon	Temperature (°C)	Size (mm)	Initial	Product	Model/Rate controlling mechanism	Reasoning	E_a (kJ/mol)	Ref
Calcined BHP, Namibian ore (NAM), and ASMAN ore	$CO:CO_2$	-	700-1100	10-20	Mn_3O_4	MnO	Shrinking core model. Combined chemical reaction and pore diffusion	SEM (observation of product layer)	41(ASM ore), 50-70 (NAM ore)	Berg, 1998
Calcined ASMAN and Gemco ore	$7CO:3CO_2$	-	700-1100	3-5 (plates)	Mn_3O_4	MnO	Shrinking core model. Combined chemical reaction and pore diffusion	SEM	30-45	Berg & Olsen, 2000
Ore details not specified	$3CO:7CO_2$	-	400-700	0.105-0.150	Mn_3O_4	MnO	Nucleation and growth	Model-fitting	66	Y. Gao et al., 2012
Baharia iron ore	$4CO:CO_2$	-	600-1000	1-4	MnO_2	MnO	Diffusion and chemical reaction control	Model-fitting and magnitude of Ea	9.61 and 36.4	El-Geassy et al., 2000
Low grade Egyptian ore which was pelletised	H_2	-	750-950	5-7	MnO_2	MnO	Chemical reaction	Model-fitting	79.8	El-Hussiny et al., 2015
MnO_2	Ar	X	1100-1400	-	MnO_2	Mn_3O_4	Multistep shrinking core	Assumption	71.3	Van Deventer, 1988

2.8 Repeatability of experiments

Several studies carried out on the reduction of manganese ores also include a study on the reproducibility of the reduction experiments.

The study by Berg & Olsen, (2000), involved the determination of the reduction kinetics of different manganese ores by carbon monoxide. The ores involved in the study were South African ores from the "ASMAN" company and Australian ores from "GEMCO" (Groote Eylandt). The reproducibility of the reduction experiments was carried out using a thermogravimetric analysis. The samples used in this study were cut from the ores received and underwent no further sample preparation. It was found that the weight loss-time relationship for two samples, cut from the same lump of ore, showed significant differences even when treated under identical conditions. This poor repeatability of experiments was attributed to the uneven distribution of minerals in the ore lump. Other explanations for this are variations in the physical properties of the ore, such as natural pores or cracks, which will affect the reduction kinetics.

In the PhD thesis by Larssen, (2020), two different types of manganese ores were also subject to a thermogravimetric analysis in order to test the repeatability of the reduction experiments. The ores used were two commercial ores, Comilog and Nchwaning ore. It was found that the reduction behaviour of the Nchwaning ore was less repeatable than that of the Comilog ore. This is due to the fact that the Nchwaning ore was more heterogenous in nature. It was also found that the larger particles of Nchwaning ore showed greater variation in reduction behaviour. This is because the larger the particle size, the fewer particles evaluated in each experimental run, which would increase the effect of natural variation.

The discussions above allow the conclusion that the repeatability of the reduction experiments is dependent on the mineral heterogeneity and the particle size of the ore being used as well as the ores natural porosity and the presence of any cracks. Due to the fact that this project deals with fine manganese ores, it is likely that the effect of mineral heterogeneity will be minimal (aided with suitable sampling methods). The presence of microcracks and porosity in fine ore is also expected to be minimal.

3 Preliminary test work

3.1 Chemical and mineralogical analysis of ore

3.1.1 Sample preparation

Samples were obtained from the Assmang Nchwaning mine in the Northern Cape, South Africa. The samples obtained were from the ultra-fines (slimes) dump. The mass of the head sample was ±300 kg. The sample obtained was wet and had to be dried in an oven at 110°C. After drying, the fine ore agglomerated significantly and had to be milled to break apart the agglomerates. The concern was how this would affect the PSD of the ore and as such golf balls were used as grinding media. The head sample was split into 10 small samples of ±30 kgs each using a large rotary splitter. Two of the 30 kg samples were recombined and re-split using the large rotary splitter. This formed 10 samples of ±6 kg each. Five of these small 6 kg samples were combined to form a representative 30 kg sample. This sample was then put through a smaller rotary splitter and split into 10 samples of ±3 kg each. These samples were then used for the experimental work.

3.1.2 Procedure and apparatus

The main aim of this section of the work was to get a good idea about the mineralogical and chemical nature of the ore. This includes the distribution of different phases, the prevalent Mn and Fe minerals and the Mn/Fe ratio. Other information such as the PSD and analyses of the different size fractions provided information on the distributions of the different minerals in the different size fractions.

Particle size distribution (PSD)

In order to determine the PSD of the sample, one of the 3 kg samples was put through a sieve shaker. The screen sizes used were 600 μm, 425 μm, 300 μm, 212 μm, 150 μm, 106 μm, 75 μm, 53 μm and a pan which represented the -53 μm fraction. Ore was fed to the 600 μm screen, after which, the lid was securely fastened, and the sieve shaker was started. The dry screening was carried out for 10 minutes. The resultant material from each screen was then weighed and the PSD was calculated.

The calculated results as well as the PSD plot are depicted below:

Table 3.1 - PSD calculations for Nchwaning slimes

Size fraction (um)	Mass on screen (g)	Mass % on screen	Cumulative mass passing screen	cumulative mass % passing
600	163.3	6.13	2501.10	93.90
425	231.3	8.68	2269.80	85.22
300	215	8.07	2054.80	77.14
212	184.4	6.92	1870.40	70.22
150	202.9	7.62	1667.50	62.60
106	193.9	7.28	1473.60	55.32
75	1066.4	40.02	407.20	15.29
53	270	10.13	137.20	5.15
37.48	137.2	5.15	0.00	0.00
	2664.4	100.00		
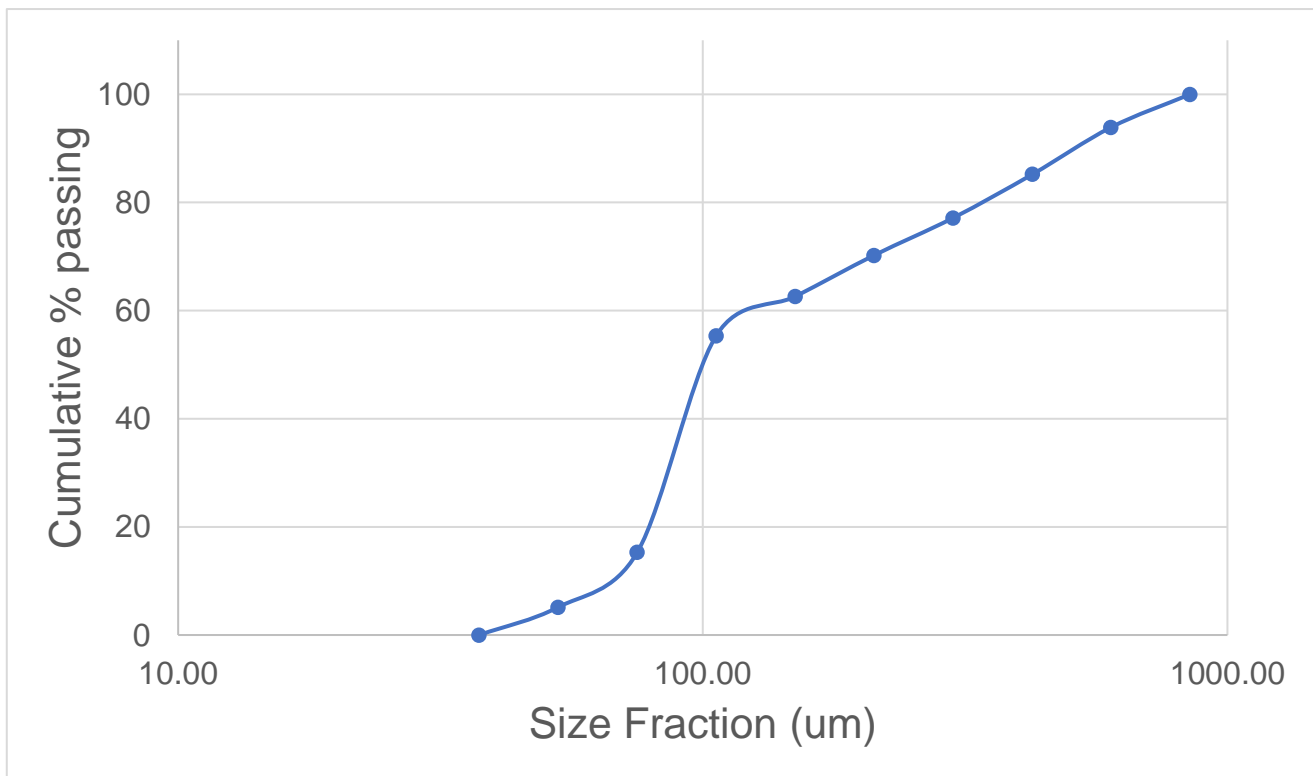
Figure 3.1 – Cumulative particle size distribution for the Nchwaning slimes sample

The obtained PSD indicated that the most prevalent size fraction in the sample is the -106+75 µm size fraction. The F80 (80% passing) for the sample lies within the - 425+300 µm size fraction.

X-Ray Diffraction (XRD)

An analysis of the different size fractions formed from the screening operation described above was carried out by XRD and XRF. The different size fractions (larger than 75 μm) were milled to -75 μm.

For the XRD analysis, the samples were prepared according to the standardized PANalytical backloading system, which provides a nearly random distribution of the particles. The samples were analysed using a PANalytical X'Pert Pro powder diffractometer in θ–θ configuration with an X'Celerator detector and variable divergence- and fixed receiving slits with Fe filtered Co-Kα radiation (λ=1.789Å). The mineralogy was determined by selecting the best–fitting pattern from the ICSD database to the measured diffraction pattern, using X'Pert Highscore plus software. The relative phase amounts (weight% of crystalline portion) were estimated using the Rietveld method (X'Pert Highscore plus software).

The XRD results, depicted in Table 3.2, indicate that the most prevalent Mn phases are braunite and braunite II, together comprising over 44% of the sample. The other major manganese phase is bixbyite, making up 12,31% of the sample. The major iron containing phase is hematite, making up 13,73% of the sample. Large amounts of carbonates were also detected, with the main one being calcite, making up 19,53% of the sample. Various other phases were detected, such as barite and magnesite, however, these phases make up very small amounts of the sample.

Table 3.2 - XRD results for different size fractions for Nchwaning slimes

Size Frac (um)	% of sample	Mn Phases						Iron Phases	Other phases			
		Bixbyite Mn_2O_3	Hausmannite Mn_3O_4	Manganite $MnO(OH)$	Braunite I $3(Mn,Fe)_2O_3.MnSiO_3$	Braunite II $7(Mn,Fe)_2O_3.CaSiO_3$	Birnessite	Hematite Fe_2O_3	Quartz SiO_2	Calcite $CaCO_3$	Magnesite $MgCO_3$	Barite $BaSO_4$
-53	5.15	24.79	3.3	6.33	25.43	0	0.77	12.24	0.03	22.17	6.33	2.29
53	10.13	10.43	0	0	16.43	24.42	0.66	12.64	1.71	21.27	11.62	0.65
75	40.02	16.37	0	3.87	0	37.15	0.72	12.28	0.84	22.71	0	2.27
106	7.28	11.43	4.04	3.69	20.41	27.7	0	15.01	1.19	16.53	0	0
150	7.62	8.28	3.8	4.22	17.42	33.13	0	14.94	1.21	17	0	0
212	6.92	8.96	3.97	3.58	18.3	32.95	0	15.41	1.48	15.36	0	0
300	8.07	7.76	3.85	3.38	18.4	34.47	0	15.74	1.36	15.04	0	0
425	8.68	8.23	4.17	3.34	19.92	31.82	0	15.96	1.25	15.3	0	0
600	6.13	0	8.8	4.03	24.33	28.96	0.32	15.52	1.11	16.94	0	0
Total	100.00	12.31	2.24	3.52	11.76	31.48	0.41	13.73	1.08	19.53	1.50	1.09

X-Ray Fluorescence (XRF)

The same samples (the different size fractions) used for XRD were used for XRF. For the XRF analysis, the samples were prepared as pressed powders (10-30g powdered sample, mixed with 20 drops Moviol (PVA) and pressed to 10 tonnes). The Thermo Fisher ARL Perform'X Sequential XRF instrument with Uniquant software was used for analysis.

XRF results, depicted in Table 3.3, indicate that the Mn content of the sample (just above 44%) was high enough to be considered a high-grade Mn ore. The major issue with the ore was thus the high iron content (14,62%) which resulted in a Mn/Fe ratio (3,01) that is too low for economic FeMn production.

Table 3.3 - XRF results on different size fractions for the Nchwaning slimes

Sample ID	Size Frac (um)	% of sample	Elements									Mn/Fe
			Mn	Fe	Ca	Mg	Si	Ba	Al	S	Na	
A	-53	5.15	44.91	14.88	7.51	2.34	2.09	2.21	0.39	0.39	0.38	3.02
B	53	10.13	44.66	15.20	7.27	2.38	2.15	2.24	0.39	0.35	0.37	2.94
C	75	40.02	44.84	14.80	7.34	2.40	2.11	2.02	0.38	0.38	0.39	3.03
D	106	7.28	43.74	14.24	7.57	2.32	2.21	1.72	0.37	0.39	0.34	3.07
E	150	7.62	43.22	14.17	7.50	2.53	2.20	1.63	0.37	0.46	0.44	3.05
F	212	6.92	43.72	14.29	7.33	2.44	2.24	1.68	0.38	0.43	0.36	3.06
G	300	8.07	43.26	14.49	7.47	2.54	2.27	1.79	0.39	0.45	0.38	2.99
H	425	8.68	42.65	14.39	7.65	2.63	2.30	1.78	0.39	0.46	0.41	2.96
I	600	6.13	41.58	14.11	8.60	2.87	2.51	2.04	0.40	0.45	0.37	2.95
Total		100.00	44.03	14.62	7.48	2.46	2.19	1.94	0.38	0.40	0.39	3.01

4 Upgrading of manganese ores by reduction roast and magnetic separation

In this section of the project, an optimization study was carried out for the reduction of manganese ores using CO as reductant. After the ore was reduced under the specified conditions for each test, it was milled and subject to a magnetic separation procedure.

4.1 Experimental design

The variables of interest in this optimization study were time, temperature, and the amount of reductant (CO: CO2 ratio). In order to simplify the experimental design, a constant time was used for each experimental run. This time is the time required for the reaction to reach completion and is described in Section 4.2.1. Being able to use a constant time means that the only two variables under consideration for the optimization studies were temperature and the amount of reductant.

4.1.1 Central composite design

A central composite type of experimental design was used for this study. The conditions (temperature and reductant addition) were obtained from the respective Chaudron diagrams.

In terms of the actual experimental design, each of the variables has 5 levels: a higher level, a lower level, a higher and lower axial point and a central point. The levels are denoted by ($-\propto$, -1, 0, 1, $\propto$). A spherical-type central composite design was considered for the optimization study and thus the star/axial points are determined by the following relationship:

$$\propto = \sqrt{k} \qquad\qquad 4.1$$

As the factorial design for the 2^K optimization study will be a 2^2 design - $\propto = 1.414$. The central composite experimental design can therefore be described in Figure 4.1 below:
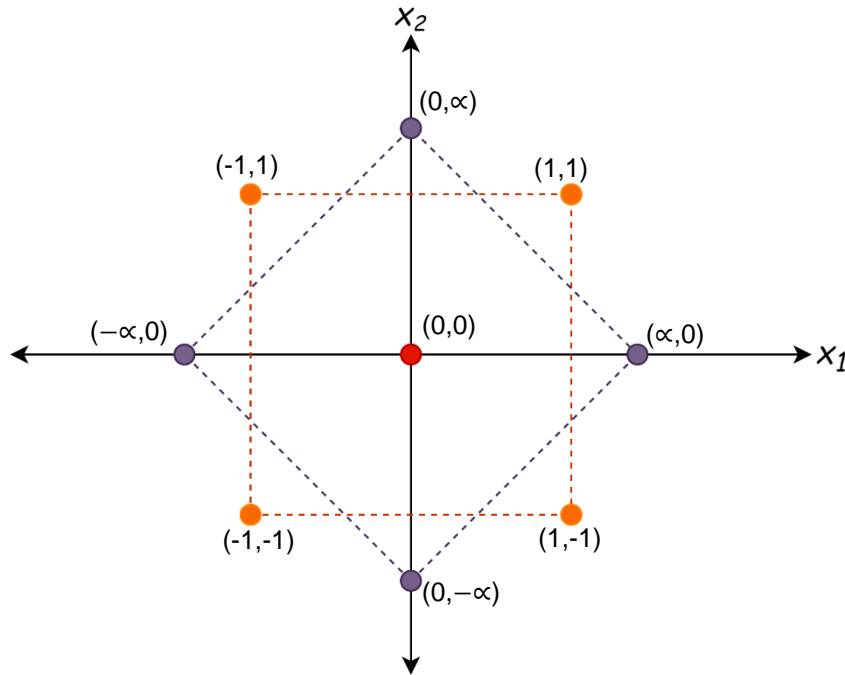
Figure 4.1 - Central composite experimental design

Central composite design using CO as reductant

The specific temperatures and CO/CO_2 ratios used for this optimization study were obtained from the Fe and Mn Chaudron diagrams. For illustrative purposes, the Chaudron diagram, with the central composite design is depicted in Figure 4.2. Experimental conditions were selected based on the placement of the central composite design within the respective chaudron diagram. The placement was dependant on two main factors – identifying an area in which the two target phases (MnO and Fe_3O_4) coexist, and to have the experimental conditions at temperatures as high as possible to ensure fast reaction kinetics.

The central composite experimental design was considered due to its ability to investigate a wide array of conditions within an experimental space. It allows for the determination of the effects of single variables on the response as well as the effects of interactions between the variables on the response. The central composite design can also be used to form numerical models and response surfaces from experimental data.

Fe Chaudron Diagram
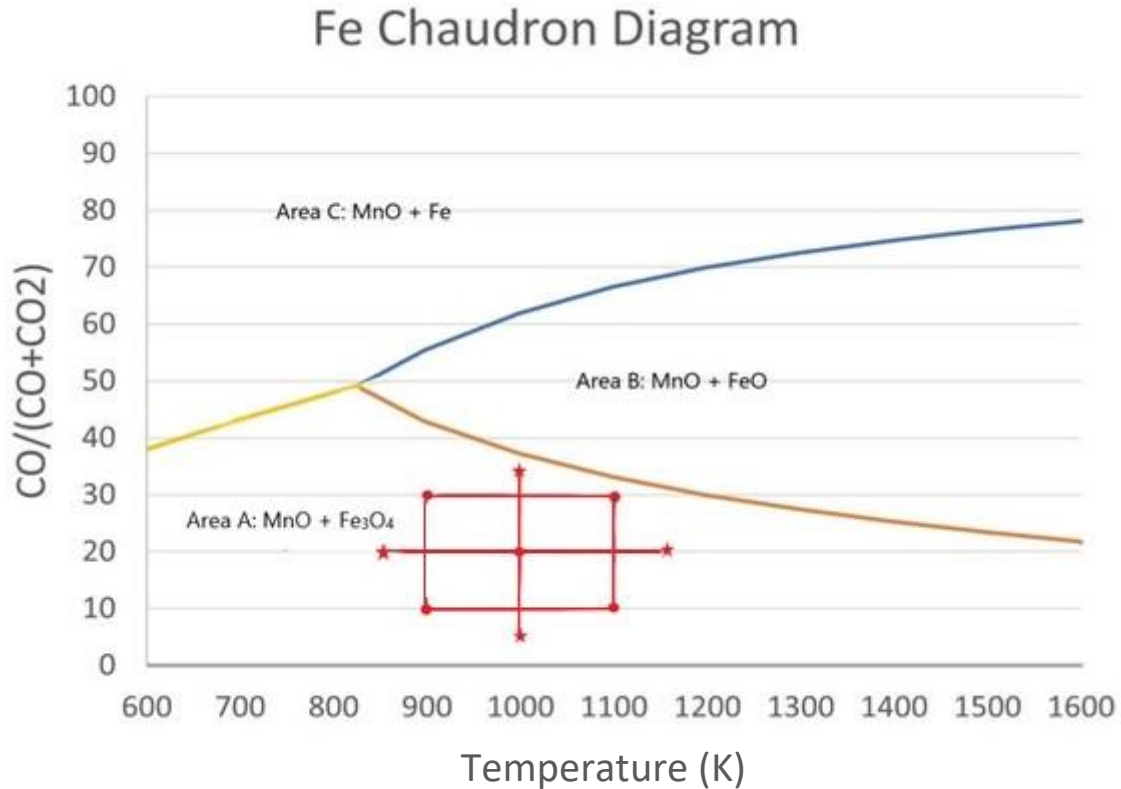
Figure 4.2 - Iron Chaudron diagram, for CO reduction, depicting the central composite experimental design

The factorial design is a 2^2 design. There are therefore 4 factorial points, 4 star/axial points (2k) and n_c centre points. The 2 factors are temperature and CO/CO$_2$ ratio. The relationship between the coded variables (x_1, x_2) and the natural variables (Temperature and CO/CO$_2$) ratio are as follows:

$$x_1\ (Temperature) = \frac{Temperature - 1000}{100} \tag{4.2}$$

$$x_2\left(\frac{CO}{CO2}\right) = \frac{\frac{CO}{CO2} - 20}{10} \tag{4.3}$$

The relationships described above can be used to formulate the different levels for each natural variable. These levels are depicted in Table 4.1.

Table 4.1 - Values of natural variables for different levels of coded variables for CO reduction tests

Parameter	Code	Higher level (+1)	Lower Level (-1)	Central point (0)	Higher axial point (+1.414)	Lower axial point (-1.414)
Temperature(K)	X_1	1100K	900K	1000K	1141,4K	858,6K
CO/CO₂ ratio	X_2	30%	10%	20%	34,14%	5,86%

The complete experimental design for the CO/CO_2 test is depicted in Figure 4.3 below:
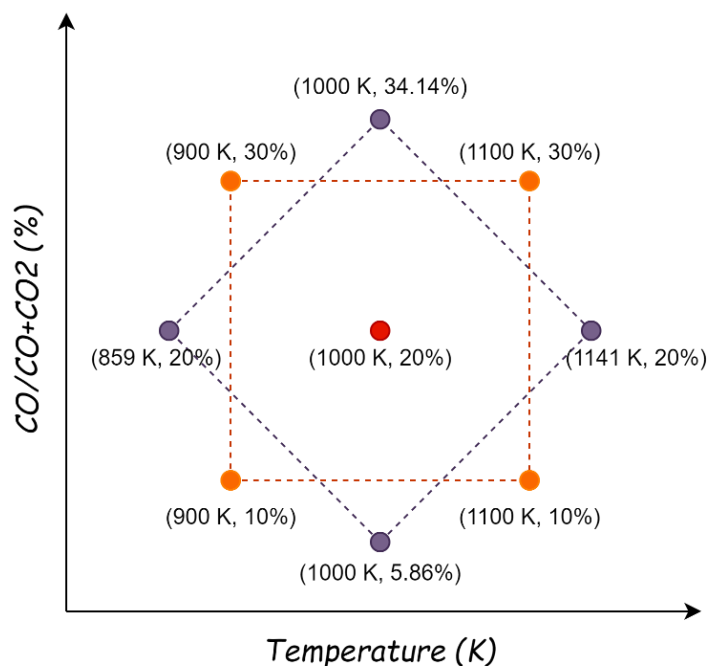
Figure 4.3 - Depiction of the experimental design for the CO/CO_2 test (including values of the natural variables)

The experimental runs are shown in Table 4.2 below. The centre point of the central composite design was run a total of 3 times, in order to establish the repeatability of the test work. This was done prior to the remainder of the tests to determine if 1 experimental run would be suitable for them.

Table 4.2 - Central composite design for CO/CO$_2$ tests

Std. order	X$_1$	X$_2$	T (K)	Reductant (CO/CO$_2$ Ratio)
1	-1	-1	900	10
2	1	-1	1100	10
3	-1	1	900	30
4	1	1	1100	30
5	-1.41	0	858,58	20
6	1.41	0	1141,42	20
7	0	-1.41	1000	5,86
8	0	1.41	1000	34,14
9	0	0	1000	20
10	0	0	1000	20
11	0	0	1000	20

4.1.2 Review metrics

The following review metrics were used in this section of the experimental work. The main aim of this investigation is to obtain a suitable feed material for FeMn production. A suitable feed material is defined as having a manganese grade > 40%, a Mn/Fe ratio of at least 7,5. A manganese recovery in the region of 80% is also advantageous in terms of the economics of the process as discussed in Section 2.1.3. Taking this into consideration, the most industrially relevant measures for this work would be the following:

- Recovery of the manganese to the non-magnetic stream (R_{Mn})
- Total manganese content of the non-magnetic stream (T_{Mn})
- The Mn/Fe ratio in the non-magnetic stream.

The R_{Mn} can be calculated in the following manner:

$$R_{Mn} = \frac{mass\ of\ non-magnetic\ product \times Mn\ Grade\ in\ non-magnetic\ product}{mass\ of\ feed\ to\ mag.sep \times Mn\ grade\ in\ mag.sep\ feed} \qquad 4.4$$

In terms of process optimization, 2 separate review metrics were considered, namely, the percentage Fe removed, and the percentage Mn lost.

The percentage Fe removed can be calculated using the following equation:

$$\%Fe\ Removed = \frac{mass\ of\ mag\ stream \times Fe\ in\ mag\ stream}{Mass\ of\ mag\ sep\ feed \times Fe\ in\ feed} \qquad 4.5$$

The percentage Mn lost can be calculated using the following equation:

$$\%Mn\ Lost = \frac{mass\ of\ mag\ stream \times Mn\ in\ mag\ stream}{Mass\ of\ mag\ sep\ feed \times Mn\ in\ feed} \qquad 4.6$$

Models of the percentage Fe removed, percentage Mn lost, and the Mn/Fe ratio were formulated using the data collected during the central composite experimental work. The models investigate first order interactions, two-way interactions, and quadratic terms in order to find the best fit within the experimental range. It should be noted that the models developed are purely empirical and are based of the best statistical fit to experimental data. The models do not attempt to explain the mechanisms involved, but rather describe what happens.

The effects of temperature and reductant addition on these review metrics are expressed by the following equation:

$$Y_i = \beta_{i0} + \beta_{i1}X_1 + \beta_{i2}X_2 + \beta_{i3}X_1X_2 + \beta_{i4}X_1^2 + \beta_{i5}X_2^2 \qquad 4.7$$

Where:

- Y_1, Y_2, Y_3 – Percentage Fe removed, percentage Mn lost and the Mn/Fe ratio in the non-magnetics respectively
- β_i – empirical model coefficients obtained from test data
- X_1, X_2 – Temperature (K) and reductant addition respectively.

4.1.3 Sample preparation

For the optimization study, the fine ore obtained from Nchwaning mine slimes dam was pressed into disc-shaped briquettes. Representative 3 kg samples were made (process described in Section 3.1.1.) from the large sample obtained. These 3 kg samples were used for the briquettes.

Each briquette had a diameter of 40 mm, a thickness of approximately 10 mm and contained 30 g of ore. The ore was mixed with approximately 3 ml of water before being pressed with a force of approximately 4,5 tonnes.

The main purpose for using briquettes is in attempt to ensure repeatability of test runs. The use of briquettes also allowed the use of a "basket" rather than a crucible. This allowed reducing gas to have a better contact area with the sample.

4.1.4 Procedure and apparatus

A vertical retort furnace setup was used for the optimization studies. A diagram of the setup is shown in Figure 4.4. The gas flow was controlled with multiple mass flow controllers.
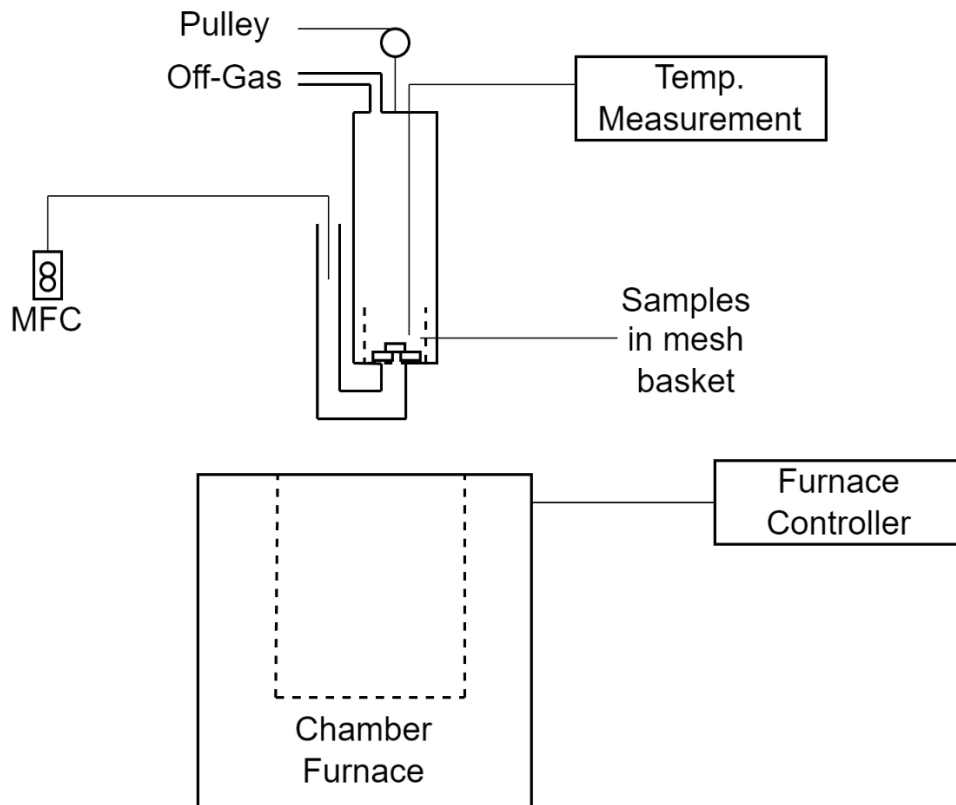
Figure 4.4 - Depiction of vertical retort furnace setup used for optimization studies

The procedure followed during each test run was as follows:

Five briquettes were selected and weighed out, after being placed into a steel basket and then placed into the retort. The briquettes were stacked in a manner that allowed for easy gas flow between them. The stacking pattern was maintained for each experimental run. The retort was then closed well to ensure an airtight seal.

Prior to the start of each test, the furnace was heated to the desired temperature. The roasting temperature was controlled by a digital temperature controller and a separate type K thermocouple was placed in a steel tube which was lowered into the retort. Once the furnace was at temperature, nitrogen (N_2) was introduced into the retort after which, it was lowered into the hot zone of the furnace – a temperature profile was carried out beforehand to ensure that the samples reached the set temperature. While

in the hot zone, the samples were allowed to heat up for 15 minutes under a N_2 atmosphere. After 15 minutes, the N_2 gas stream was closed, and the relevant reducing gas mixture was allowed to flow. The inlet gas was fixed at 1,5 l/min. The reduction then proceeded for 1 hour 45 minutes (for details on how this time was determined, refer to Section 4.2.1). Once the reduction time had elapsed, the retort was removed from the furnace and the samples were allowed to cool in a nitrogen atmosphere. The samples were then removed and weighed. The reduced briquettes were then pulverised, split using a rotary splitter and magnetically separated using a Davis Tube (wet magnetic separation device in which the sample is placed within a glass tube that is moved repeatedly into and out of a magnetic field, causing magnetic particles to be held in suspension, while non-magnetic particles pass through the magnetic field), with a magnetic intensity of 1550 Gauss. The resulting magnetic stream and non-magnetic stream were then sent for XRF and XRD analysis and were mounted for SEM analysis.

4.2 Preliminary Tests

4.2.1 Test to determine suitable experimental time

In the central composite design, there are two main variables – temperature and reductant ratio. In order to determine a suitable time period that each test in the optimization study can be run for, a test was carried out on the thermobalance setup (same setup used for the kinetic study – more information in Section 5.1).

This test was carried out with the same experimental conditions as the centre point of the central composite design, i.e., a 20% CO, 80% CO_2 gas mixture at a temperature of 1000 K.

The results of the thermobalance test are shown in Figure 4.5 below:
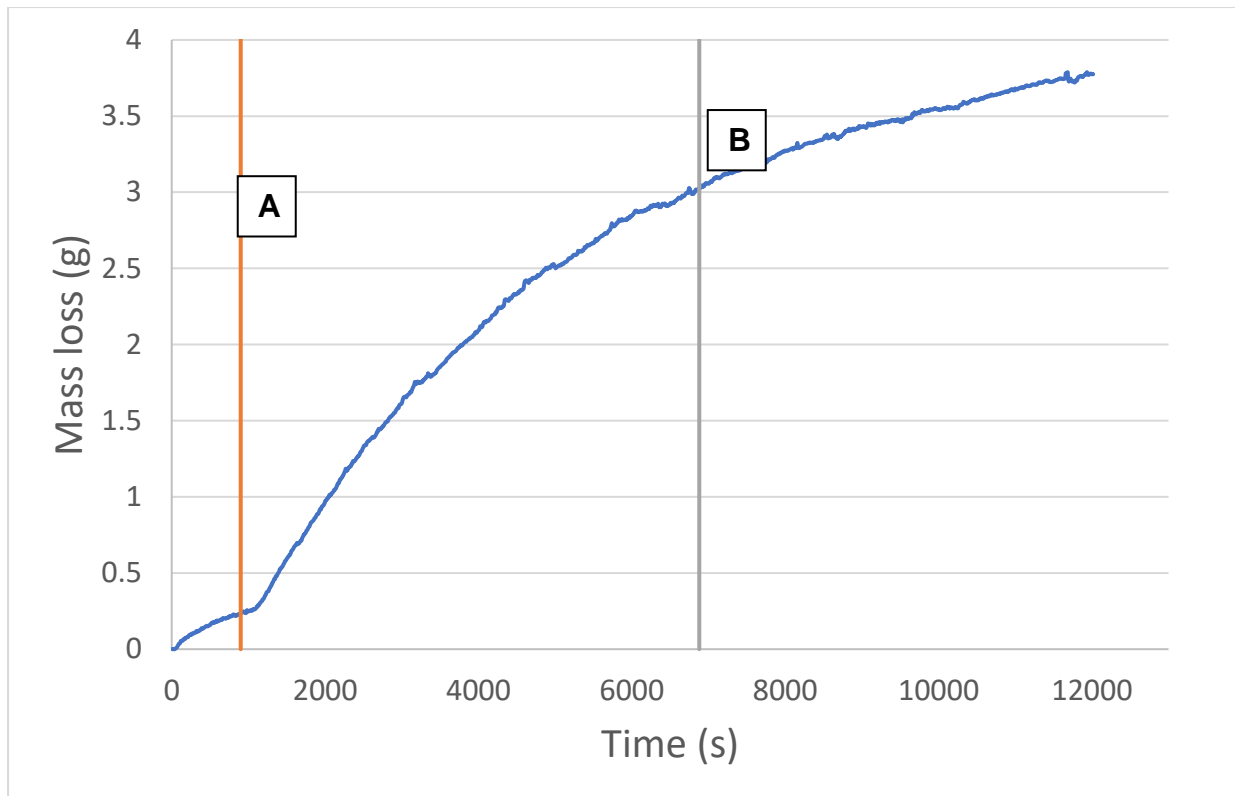
Figure 4.5 - Mass loss vs time plot for time determination study in CO/CO₂ atmosphere (N₂ inert atmosphere on left of line A, CO/CO₂ atmosphere on right of line A. Line B represents time at 80% reduction). Test carried out at 1000 K and 20 vol% CO

Figure 4.5 represents the mass loss over time for the test carried out in the thermobalance. Line A represents the time at which the atmosphere was changed from an N_2 purging atmosphere to a reducing CO/CO_2 atmosphere. Line B represents the time at which 80% of the reduction has taken place. This time is 6880 seconds or 1,91 hours. It was therefore decided that a total time of 2 hours would be suitable for each test run. This includes 15 minutes under an inert atmosphere (either N_2 or Ar) while the samples heat up to the relevant temperature and 1 hour 45 minutes under the relevant CO/CO_2 atmosphere.

4.2.2 Test to determine suitable magnetic field intensity

A series of tests were carried out to determine the effect of magnetic intensity. In order to carry out these tests, samples were reduced at the following conditions: 1000K and 20 vol% CO. These conditions coincide with the centre point of the central composite design. The variable under investigation was the magnetic field intensity of the Davis Tube. All other variables – time, water flowrate, motor speed and mass of sample used remained constant. The range of magnetic field intensities were obtained from the

typical values found in literature (summary in Table 2.7). According to L. Gao et al., (2018) and Liu et al., (2018b), an optimum magnetic field intensity of 1000 Gauss was determined, while Huang et al., (2013) found an optimum magnetic field intensity of 1881 Gauss. A summary of the investigated magnetic field intensities, along with the calculated review metrics are shown in Table 4.3 below.

Table 4.3 - Results of magnetic field intensity tests (original ore Mn/Fe ratio of 3,01)

Sample Number	Davis Tube Controller setting (A)	Magnetic Intensity (G)	%Fe Removed	%Mn Lost	Mn/Fe Ratio in Non-mags
1	0,4	1000	14,44	4,54	3,18
2	0,5	1300	13,89	5,56	3,26
3	0,6	1550	22,5	8,94	3,58

Two main observations could be taken from the results of this test. The first is that the most suitable magnetic field intensity for this test work is 1550 Gauss. The second observation is that the increase in the Mn/Fe ratio was not as large as that achieved in other work with this process.

4.3 Results of optimization study

The quantification of the reduction roast and magnetic separation process was carried out by determining the elemental composition of each stream using XRF and the phase composition using XRD. The relevant review metrics were then calculated using this data.

4.3.1 Reproducibility of experiments

In order to test the reproducibility of the experiments in the optimization study, 3 tests were carried out at the conditions representing the centre point of the central composite design. These conditions are a temperature of 1000K and a CO content of 20 vol% CO. The XRF results and calculated review metrics for these 3 tests are summarised in Table 4.4 and Figure 4.6. The results of the tests show insignificant differences between the 3 sets of tests. It can therefore be concluded that the tests show good repeatability.

Table 4.4 - XRF results and calculated review metrics for reproducibility tests

Test number	XRF of non-mags		Review Metrics			
	wt% Mn	wt% Fe	Mn recovery to non mags	Mn/Fe ratio in non-mags	%Fe removed	%Mn lost
Centre point 1	47.2	13.2	82.01	3.58	22.5	8.94
Centre point 2	47.4	13.5	85.22	3.51	22.98	8.94
Centre point 3	47.6	13.2	80.22	3.61	22.43	8.71

A plot of the results for each different test is depicted in Figure 4.6.
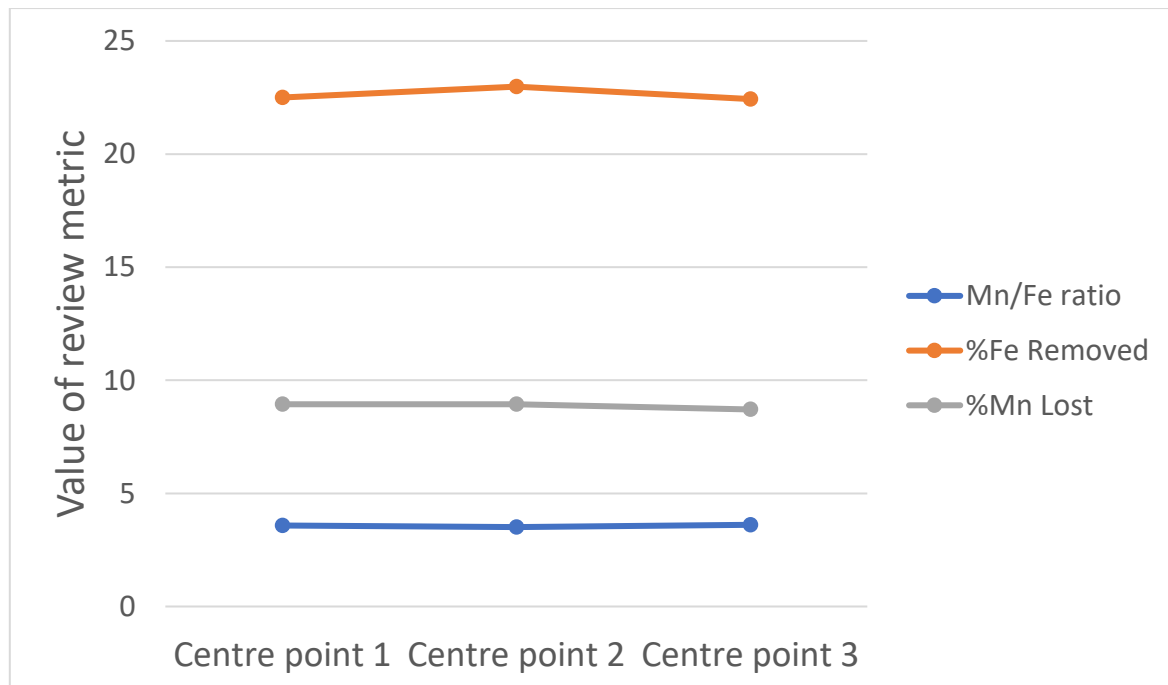
Figure 4.6 - Values of different review metrics used to indicate the reproducibility of tests

4.3.2 XRD results

The XRD results obtained from each test run is depicted in Table 4.5 below. The XRD results indicate that the target phases were achieved. In the majority of the tests, all hematite was reduced either to magnetite or jacobsite (both these phases have a spinel structure) and the majority of manganese phases were reduced to MnO. This indicates that the reduction step for the optimization study was successful in producing phases with different magnetic susceptibilities. Run 4 and 8 indicate that there is neither hematite no magnetite present. This meant that the iron in the sample,

observed from XRF and SEM EDS analysis was not accounted for. Upon further investigation of the XRD spectra obtained, it was observed that under these conditions, iron oxides were reduced to wustite. The wustite then reacted with manganosite to form a composite monoxide phase (FeO – MnO solid solution) – this phenomena was reported previously by L. Gao, Liu, Pan, et al., (2019). Considering both, the sample chemistry from XRF and SEM EDS, as well as the best fit to the observed XRD spectra, the phase identified was $(FeO)_{0.331}(MnO)_{0.669}$. "Run 8 mags," for example, was found to be comprised of 70,8% of this composite monoxide phase, which accounts for the iron found in the XRF results.

Considering the FeO-MnO phase diagram in Figure 4.7 below, it can be seen that there exists a wide range of solid solubility between MnO and FeO.
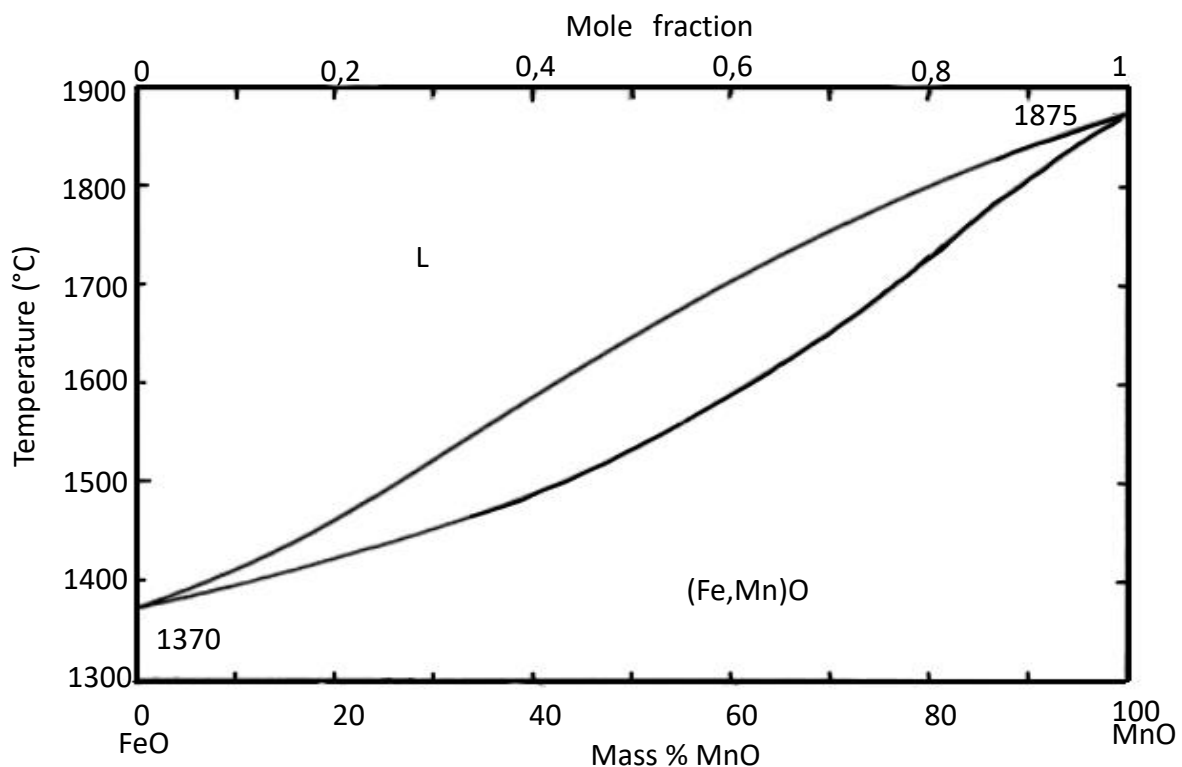
Figure 4.7 - FeO - MnO system (Allibert et al., 1995)

Considering the thermodynamic likelihood of forming wustite under the conditions used for Run 4 (1100K – 30 vol% CO) and Run 8 (1000K – 34,14 vol% CO), from Figure 4.2, these two points are the closest sets of conditions to the border between the magnetite and wustite stability fields. It should also be noted that Figure 4.2 is drawn assuming unit activities for each solid phase. If FeO were to form, the activity would be lower than 1. This would cause the FeO-Fe$_3$O$_4$ boundary to shift downwards

as depicted in Figure 4.8. This shift of the FeO + MnO phase field indicates that it is thermodynamically possible that FeO could form under these conditions. FeO – Fe_3O_4 boundaries for different FeO activities are depicted in Figure 4.8 (assuming ideal solution and that the activity follows Raoult's law).
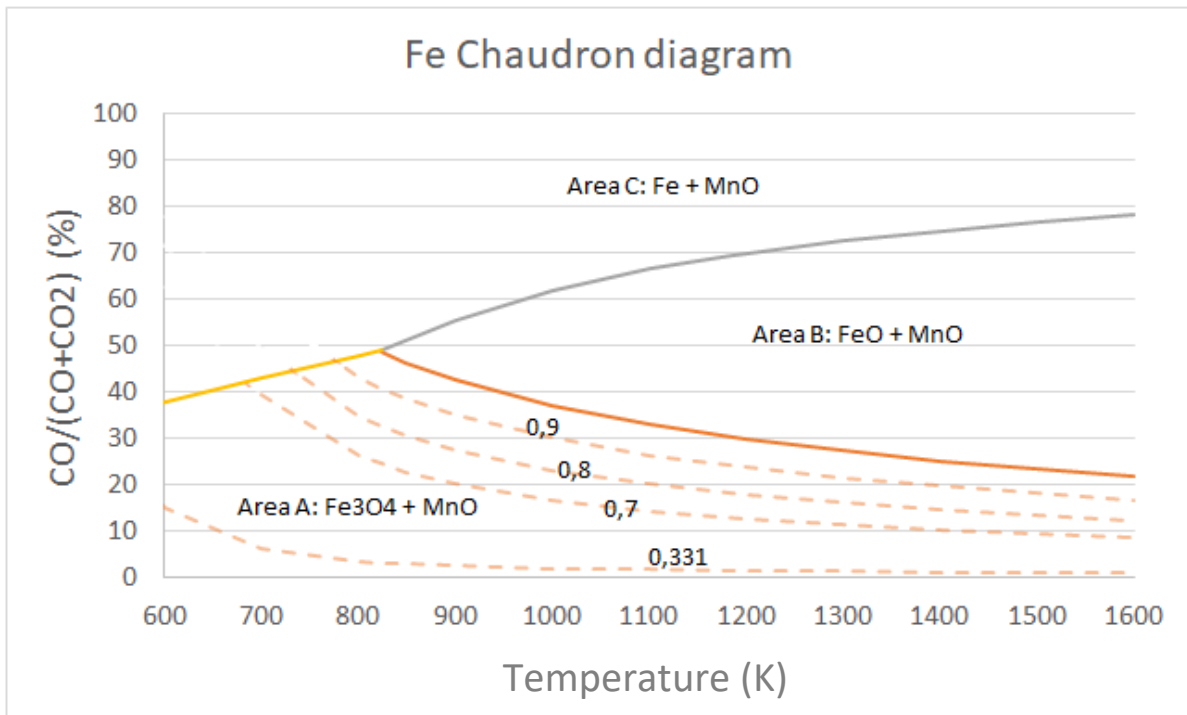
Figure 4.8 - Iron chaudron diagram with the FeO-Fe_3O_4 boundary drawn for different FeO activities (FeO activity indicated on each respective line)

Table 4.5 - XRD results of the different test runs for the optimization study

Test Number	Temperature (K)	%CO	Mn Phases					Fe Phases		Other Phases		
			Bixbyite	Hausmannite	MnO	Braunite I	Braunite II	Hematite	Magnetite	Jacobsite	Calcite	Quartz
Unreacted Ore	-	-	12.31	2.24	0	11.76	31.48	13.73	0	0	19.53	1.08
*CP2 Mags	1000	20	-	-	33	-	6.66	-	30.42	2.3	7.61	-
*CP2 Non-mags	1000	20	8.83	-	55.2	-	-	-	-	13.06	19.12	0.7
*CP3 Mags	1000	20	-	-	32.15	-	3.82	-	24.74	24.69	14.61	-
*CP3 Non-mags	1000	20	9.52	-	54.7	-	-	-	-	12.85	19.47	0.36
Run 1 Mags	900	10	9.53	-	19.45	-	9.71	5.39	-	42.61	13.3	-
Run 1 Non-mags	900	10	-	-	17.96	-	37.85	-	14.14	1.8	25.3	0.75
Run 2 Mags	1100	10	8.89	-	32.83	-	3.4	-	-	45.53	9.35	-
Run 2 Non-mags	1100	10	-	-	40.29	-	16.77	11.3	-	16.98	12.74	-
Run 3 Mags	900	30	-	-	25.19	-	11.18	-	15.61	37.72	10.3	-
Run 3 Non-mags	900	30	-	-	43.81	-	17.72	-	-	12.54	22.96	0.89
Run 4 Mags	1100	30	-	-	93.2	1.35	-	-	-	2.15	3.29	-
Run 4 Non-mags	1100	30	-	-	88.18	-	1.5	-	-	3.92	5.77	-
Run 5 Mags	858	20	-	-	20.42	-	16.28	-	11.63	42.13	9.54	-
Run 5 Non-mags	858	20	-	-	24.99	-	33.01	-	-	14.07	24.69	-
Run 6 Mags	1141	20	-	-	48.12	-	6.72	-	-	45.16	-	-
Run 6 Non-mags	1141	20	-	-	80.5	-	7.68	-	-	8.8	-	-
Run 7 Mags	1000	5.86	-	-	18.22	-	18.5	10.37	23.26	17.04	12.6	-
Run 7 Non-mags	1000	5.86	-	10.84	20.14	11.45	20.64	9.27	-	-	23.41	-
Run 8 Mags	1000	34.14	-	-	74.45	-	1.87	-	-	5.03	18.65	-
Run 8 Non-mags	1000	34.14	-	-	73.63	-	1.93	-	-	3.94	18.15	-

*CP – Centre point

4.3.3 XRF data

The XRF data for the different test runs in the optimization study is depicted in Table 4.6. The XRF data indicates that the separation between magnetic phases and non-magnetic phases was poor. While this resulted in a Mn/Fe ratio below the target value of 7.5, the Mn grade in the ore does remain at acceptable levels.

Table 4.6 - XRF results of the different test runs for the optimization study

Test Number	Temperature (K)	%CO	Element						
			Mn	Fe	Ca	Si	Mg	Ba	Mn/Fe
*CP2 Mags	1000	20	33.78	29.61	4.15	1.35	1.57	0.74	1.14
*CP2 Non-mags	1000	20	47.43	13.5	7.36	2.17	2.26	1.94	3.51
*CP3 Mags	1000	20	34.08	29.93	4.33	1.33	1.63	1.05	1.14
*CP3 Non-mags	1000	20	47.64	13.2	7.42	2.17	2.23	1.96	3.61
Run 1 Mags	900	10	34.33	30.04	3.85	1.2	1.42	0.795	1.14
Run 1 Non-mags	900	10	45.86	13.9	7.48	2.16	2.28	1.89	3.30
Run 2 Mags	1100	10	38.41	25.33	4.63	1.24	1.76	0.936	1.52
Run 2 Non-mags	1100	10	46.64	14.35	7.13	2.02	2.24	1.96	3.25
Run 3 Mags	900	30	30.12	32.81	4.39	1.25	1.43	0.916	0.92
Run 3 Non-mags	900	30	47.15	12.69	7.62	2.25	2.28	2.01	3.72
Run 4 Mags	1100	30	34.81	25.37	4.82	1.97	1.62	0.912	1.37
Run 4 Non-mags	1100	30	46.43	15.19	7.06	2.35	2.04	1.64	3.06
Run 5 Mags	858	20	32.49	31.69	3.99	1.23	1.42	0.859	1.03
Run 5 Non-mags	858	20	46.22	13.1	7.68	2.22	2.26	1.95	3.53
Run 6 Mags	1141	20	39.16	25.61	4.16	1.32	1.56	1.03	1.53
Run 6 Non-mags	1141	20	47.37	14.63	6.69	2.25	2.02	1.59	3.24
Run 7 Mags	1000	5.86	38.62	24.64	4.38	1.21	1.56	0.834	1.57
Run 7 Non-mags	1000	5.86	45.56	14.47	7.27	2.06	2.3	1.9	3.15
Run 8 Mags	1000	34.14	26.59	36.09	4.52	1.61	1.67	1.05	0.74
Run 8 Non-mags	1000	34.14	46.56	14.77	7.22	2.24	2.22	1.9	3.15

*CP – Centre point

4.3.4 Calculated review metrics

The data obtained from the XRF analysis was used to determine the values of the review metrics – Mn/Fe ratio of the non-magnetic stream, the percentage Mn lost, and the percentage Fe removed. The results are shown in Table 4.7.

Table 4.7 - Calculated review metrics at different combinations of temperature and vol% CO. Results are highlighted with conditional formatting - green indicates the best result for a specific metric and red the worst.

T (K)	Reductant	Mass% to non-mags	Mn Recovery to non-mag	Mn/Fe in non-mag	% Fe removed	% Mn lost
900	10	84.53	88.04	3.30	19.84	7.73
1100	10	85.40	90.46	3.25	18.12	9.37
900	30	79.38	85.00	3.72	34.50	10.80
1100	30	92.81	97.87	3.06	1.67	0.78
859	20	83.18	87.32	3.53	27.66	9.67
1141	20	83.74	90.09	3.24	18.03	9.40
1000	5.86	85.89	88.87	3.15	14.16	7.56
1000	34.14	94.14	99.55	3.15	2.35	0.59
1000	20	79.11	85.22	3.51	22.98	8.94
1000	20	74.16	80.24	3.61	22.43	8.71
1000	20	73.92	82.01	3.58	22.50	8.94

From Table 4.7, it is evident that the increase in Mn/Fe ratio is significantly smaller than the goal of this work. The Mn/Fe ratio increased from 3,00 to 3,72 in the best result (900 K, 30 vol% CO). The Mn content of the non-magnetic stream from this test contains 47,15% Mn (upgraded from 44% Mn). The Mn content, therefore, is within an acceptable region. In this specific test, the percentage Fe removed also peaks at 34,50%. Unsurprisingly, this specific test also has the highest percentage Mn lost at 10,80%. The Mn recoveries to the non-magnetic stream does seem to be high in most tests, however, this is not a critical metric, as a high Mn recovery may just mean that there was very little magnetics recovered for a specific test. Tests at 1100 K - 30 vol% CO and 1000 K - 34,14 vol% CO are two examples of tests with high recoveries but with most of the reduced sample reporting to the non-magnetic stream.
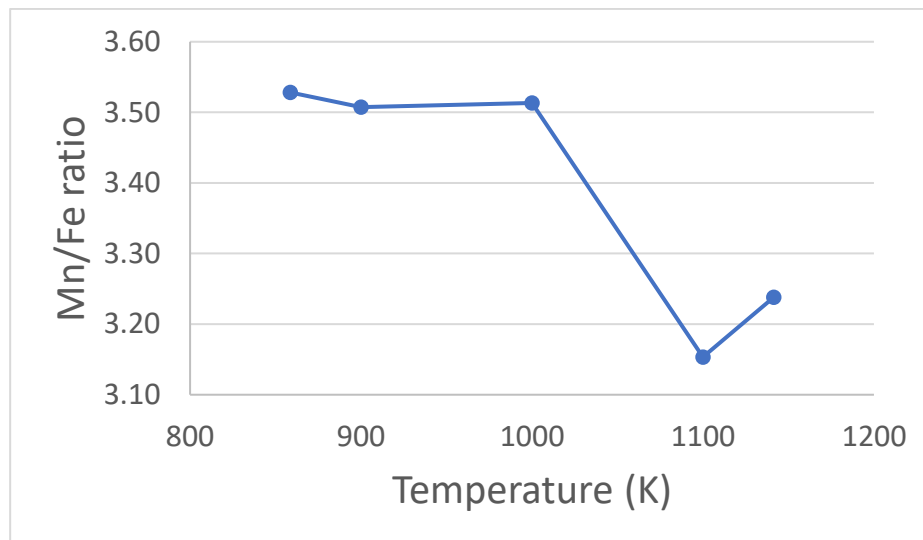
Effect of temperature

The effect of temperature was studied by considering Tests 1, 2, 3, 4, 5, 6 and a CP (centre point). The test numbers can be found in Table 4.2. The temperatures

in these tests are 859 K, 900 K, 1000 K, 1100 K and 1141 K respectively. Table 4.8 summarises the results for the tests at different temperatures in which a constant fraction of CO was used (20 vol%). Averages of review metrics from Tests 1 and 3 (900 K) and Tests 2 and 4 (1100 K) were considered, even though different fractions of CO were used at these temperatures. This averaging is a valid property of the factorial design.

Table 4.8 - Results from tests at different temperatures with a constant fraction CO (20 vol%)

Temperature(K)	Magnetic Stream			Non-magnetic stream		
	Wt% of sample	XRF		Wt% of sample	XRF	
		Wt% Fe	Wt% Mn		Wt% Fe	Wt% Mn
859	16.82	31.69	32.49	83.18	13.1	46.22
1000	20.89	29.61	33.78	79.11	13.5	47.43
1141	16.26	25.61	39.16	83.74	14.63	47.37

Plots of the 3 review metrics (Mn/Fe ratio, percentage Mn lost and percentage Fe removed) can be found in Figures 4.9, 4.10 and 4.11 below.

Figure 4.9 - Effect of temperature on Mn/Fe ratio in the non-magnetic stream
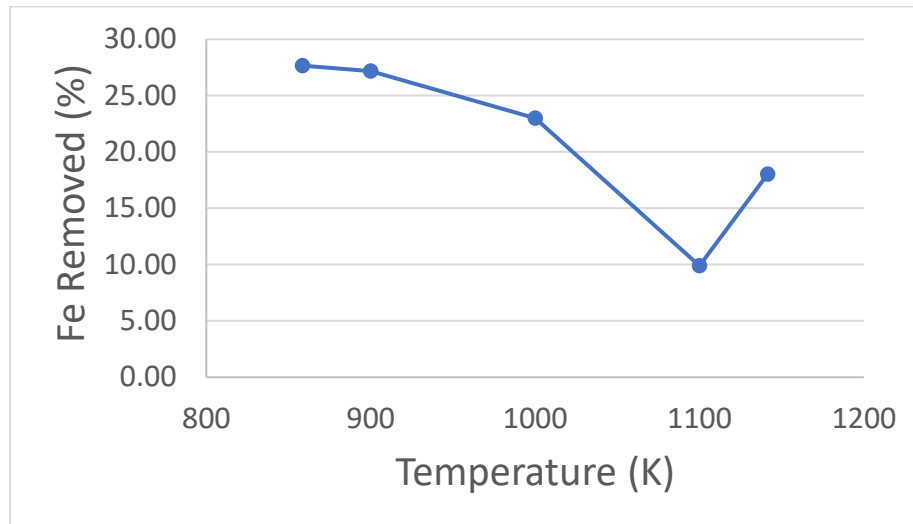
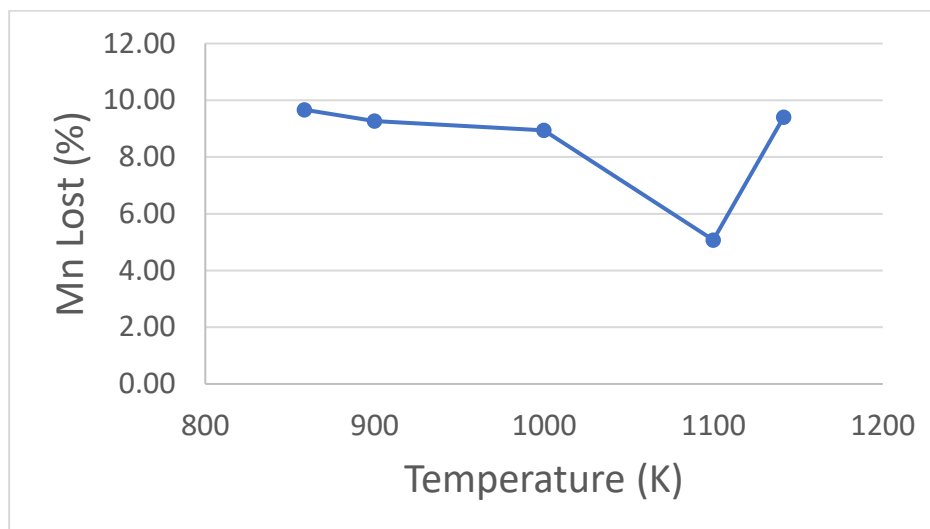*Figure 4.10 - Effect of temperature on the percentage Fe removed*

Figure 4.11 - Effect of temperature on the percentage Mn lost

From the Figures 4.9 – 4.11, it can be seen that as the temperature increases, the Mn/Fe ratio and the percentage Fe removed was found to decrease. This could be due to the presence of solid solutions of Fe and Mn which hinder the separation of Mn and Fe oxides. The specific solid solution phase found was $(FeO)_{0.099}(MnO)_{0.901}$. The percentage Mn lost remains fairly constant over the temperature range. The results at 1100 K were considerably lower than other results. The tests at 1100 K were carried out at 10 vol% CO and 30 vol% CO and the average value was considered. At 1100 K and 30 vol% CO, the reduction of

iron oxides proceeded to wüstite rather than magnetite. This then resulted in the formation of a solid solution phase $(FeO)_{0.331}(MnO)_{0.661}$ and significantly affected the review metrics.

Effect of CO content

The effect of CO content of the reducing gas mixture was studied by considering Tests 1, 2, 3, 4, 7, 8 and a CP (centre point). The test numbers can be found in Table 4.2. The CO content considered in these tests are 5,86 vol%, 10 vol%, 20 vol%, 30 vol% and 34,14 vol% respectively. Table 4.9 summarises the results for the tests at different fractions of CO that were run at a constant temperature (1000 K). Averages of review metrics from Tests 1 and 2 (10 vol% CO) and Tests 3 and 4 (30 vol% CO) were considered, even though these tests were run at different temperatures. As previously mentioned, this averaging is a valid property of a factorial design.

Table 4.9 - Results from tests at different CO contents

CO Content	Magnetic Stream			Non-magnetic stream		
	Wt% of sample	XRF		Wt% of sample	XRF	
		Wt% Fe	Wt% Mn		Wt% Fe	Wt% Mn
5,86	14.12	24.64	38.62	85.88	14.47	45.56
20	20.89	29.61	33.78	79.11	13.5	47.43
34,14	5.86	36.09	26.59	94.14	14.77	46.56

Plots of the 3 review metrics (Mn/Fe ratio, percentage Mn lost and percentage Fe removed) can be found in Figures 4.12, 4.13 and 4.14 below.
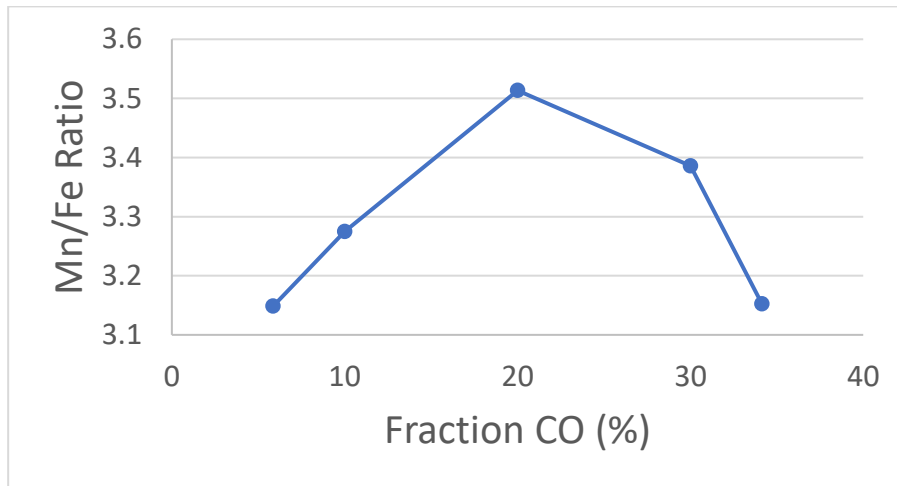
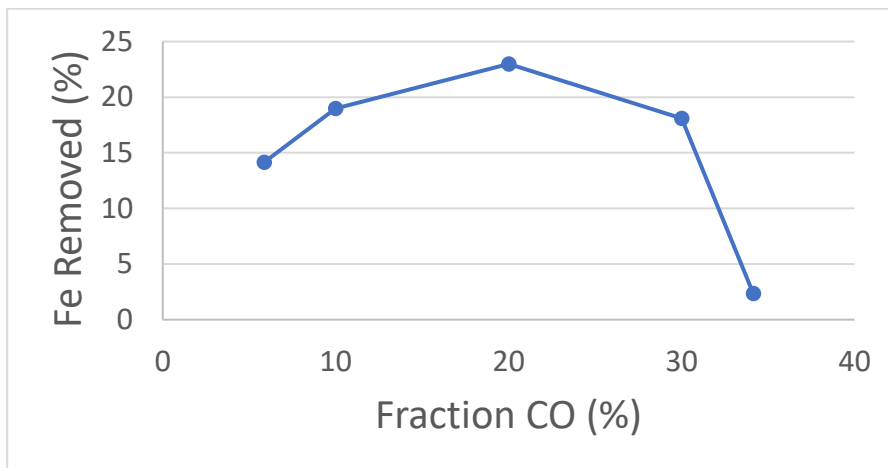*Figure 4.12 - Effect of CO content on Mn/Fe ratio in the non-magnetic stream*

Figure 4.13 - Effect of CO content on the percentage Fe removed
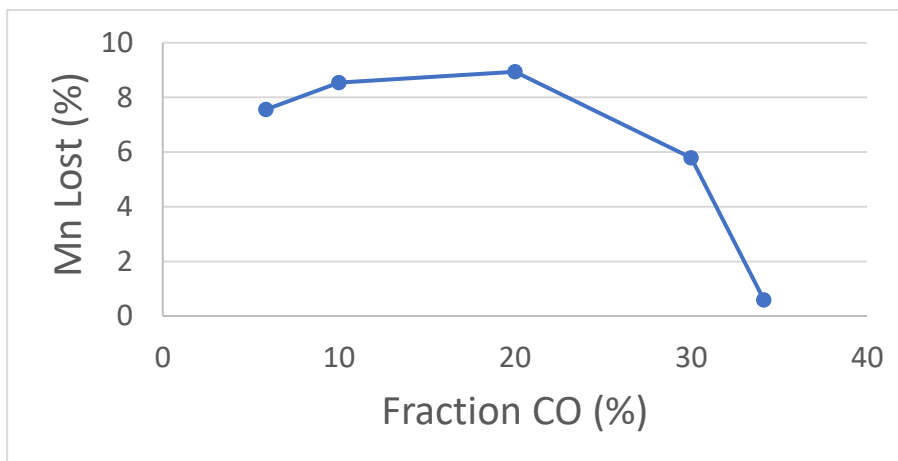

Figure 4.14 - Effect of CO content on the percentage Mn lost

The results are depicted in Figures 4.12 – 4.14. Each of the 3 figures indicate a similar trend as the CO content of the reducing gas mixture increases. As the CO content increases from 5.86 vol% to 20 vol%, an increase in each of the review metrics is noted, including the percentage Mn lost, in which an increase is undesirable. However, as the CO content further increases from 20 vol% to 34.14 vol%, large decreases in each of the review metrics are observed. From an experimental viewpoint, when magnetic separation was carried out for this specific sample, very little magnetics were recovered. In order to explain this, the XRD spectra was investigated. It was determined, based on the chemistry observed from XRF and SEM EDS analysis, that the presence of a solid solution phase is the reason for the small amount of magnetics recovered. The phase observed is $(FeO)_{0.331}(MnO)_{0.669}$. After Rietveld refinement, it was found that this phase makes up 70.8% of the small amount of magnetics recovered. This indicates that at this high-volume fraction CO in the reducing gas, the reduction proceeded further than required – reducing to wüstite, rather than magnetite. The formation of composite monoxide phases has been previously observed (L. Gao, Liu, Pan, et al., 2019). The data from the test at 30 vol% CO fits well within the observed trend in the gas composition analysis, as both, the test at 30 vol% CO and the test at 34.14 vol% CO resulted in the formation of wüstite rather than magnetite and subsequently, the formation of a solid solution phase. In the temperature analysis, the test at 1100K and 30 vol% CO was the only point in which reduction to wustite was observed. This resulted in the point at 1100 K not fitting well within the observed trend.

4.4 Models

Despite the results of the optimization study not resulting in a high Mn/Fe ratio, the review metrics were still modelled using response surface methodology and a least squares method to fit a numerical model to the data. A statistical analysis was also carried out on the models to determine if they were statistically significant.

4.4.1 Mn/Fe ratio model

The model for the Mn/Fe ratio is as follows:

$$Mn/Fe\ ratio\ =\ 3{,}56 - 0{,}14x_1\ +\ 0{,}028x_2 - 0{,}15x_1x_2 - 0{,}073x_1^2\ -\ 0{,}19x_2^2 \qquad 4.8$$

Where:

$$x1\ =\ \frac{T - 1000}{100} \qquad\qquad 4.2$$

$$x2\ =\ \frac{\frac{CO}{CO+CO2} - 20}{10} \qquad\qquad 4.3$$

The statistical analysis of the developed model yielded an R^2 = 0,934, an adjusted R^2 = 0,852 and a lack of fit (Pr >F) = 0,488. The model therefore has a high adjusted R^2 value and a lack of fit that is not significant.

The contour plot and response surface developed for the Mn/Fe ratio is shown in Figures 4.15 and 4.16.
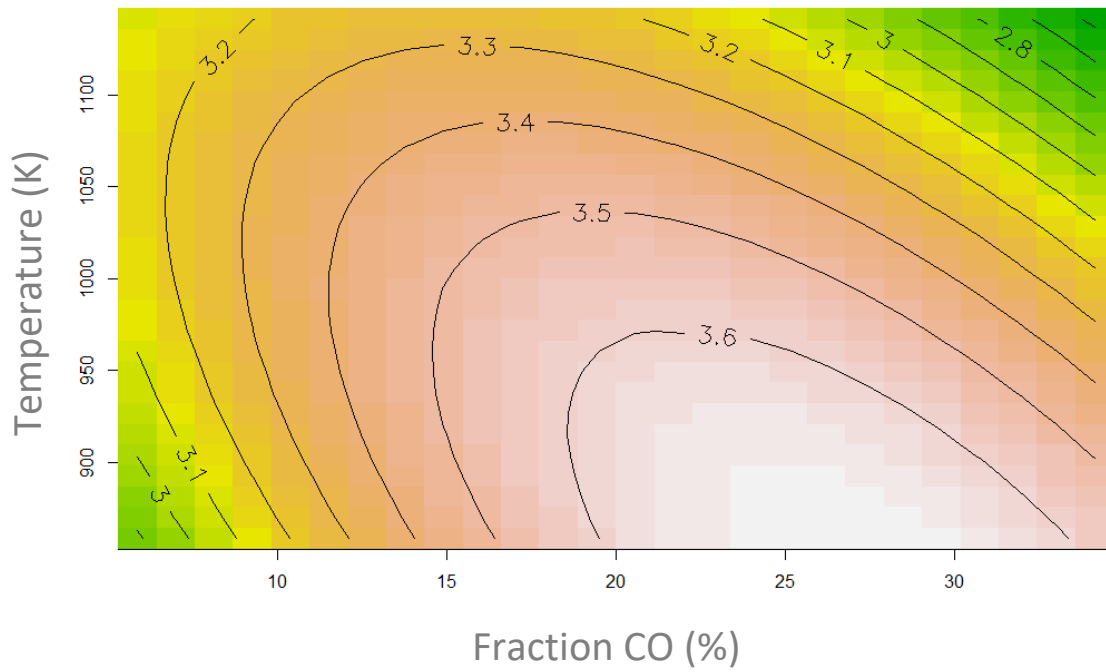
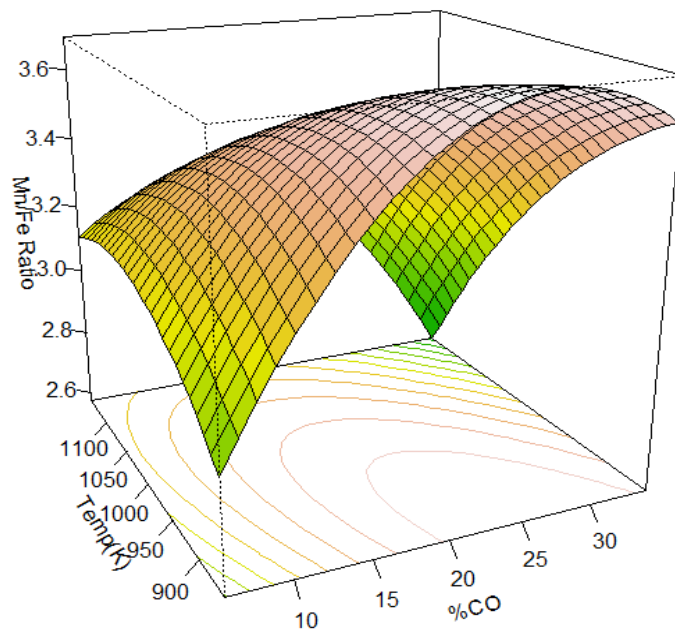*Figure 4.16 - Contour plot for the Mn/Fe ratio*

Figure 4.15 - Response surface for the Mn/Fe ratio

From Figure 4.15 and Figure 4.16, it can be seen that the Mn/Fe ratio approaches a maximum at lower temperatures and at higher CO contents of the reducing gas mixture. The stationary point in this response surface is at a temperature of 822 K and a CO content of 27,9 vol%. A comparison between experimental Mn/Fe ratios and those calculated using the model is shown in Table 4.10 below.

Table 4.10 - Comparison between experimental Mn/Fe ratio and calculated Mn/Fe ratio

std.order	x1	x2	T (K)	Reductant	Experimental Mn/Fe ratio	Calculated Mn/Fe ratio	% Difference
1	-1	-1	900	10	3,30	3,26	-1,27
2	1	-1	1100	10	3,25	3,28	1,00
3	-1	1	900	30	3,72	3,62	-2,59
4	1	1	1100	30	3,06	3,03	-0,71
5	-1.41	0	859	20	3,53	3,61	2,39
6	1.41	0	1141	20	3,24	3,22	-0,64
7	0	-1.41	1000	5,86	3,15	3,14	-0,21
8	0	1.41	1000	34,14	3,15	3,22	2,23
9	0	0	1000	20	3,51	3,56	1,36
10	0	0	1000	20	3,61	3,56	-1,33

4.4.2 Percentage Fe removed model

The model for the percentage Fe removed is as follows.

$$\% \, Fe \, Removed \; = \; 22{,}71 - 6{,}02x_1 - 2{,}31x_2 - 7{,}78x_1x_2 + 0{,}81x_1^2 \; - \; 6{,}48x_2^2 \quad 4.9$$

Where:

$$x1 \; = \; \frac{T - 1000}{100} \qquad\qquad 4.2$$

$$x2 \; = \; \frac{\frac{CO}{CO+CO2} - 20}{10} \qquad\qquad 4.3$$

The statistical analysis of the developed model yielded an $R^2 = 0{,}893$, an adjusted $R^2 = 0{,}759$ and a lack of fit (Pr >F) = 0,0498. The model therefore has a reasonably high adjusted R^2 value and a lack of fit that is on the verge of being significant.

The contour plot and response surface developed for the percentage Fe removed is shown in Figures 4.17 and 4.18.
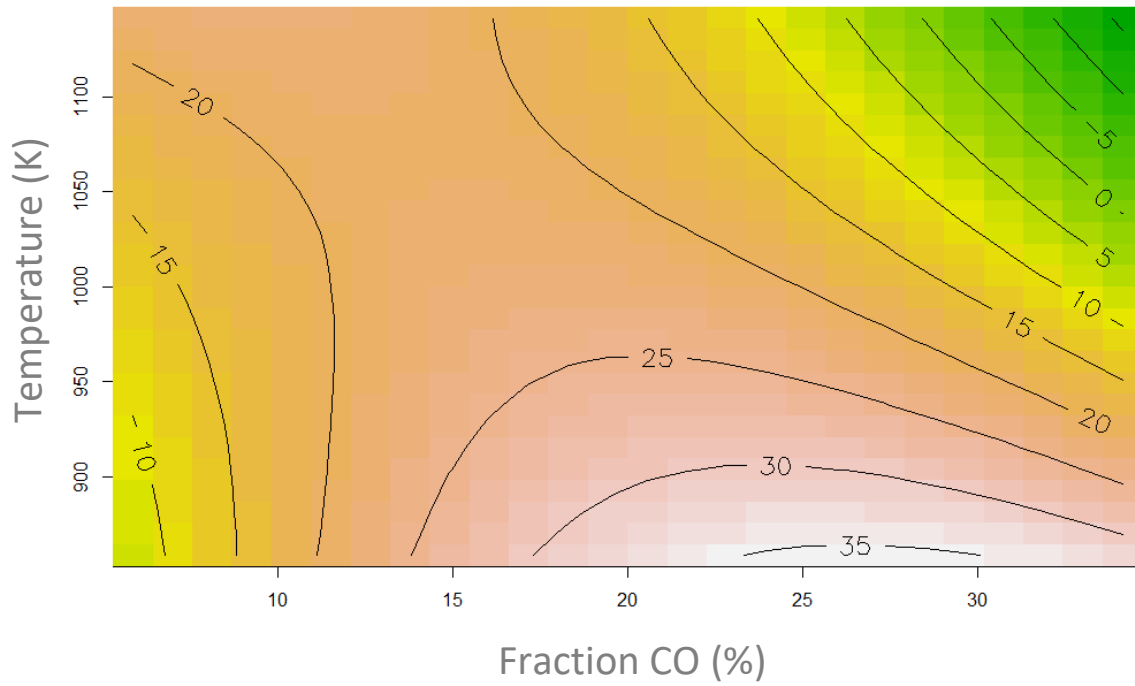
Figure 4.17 – Contour plot for the percentage Fe removed
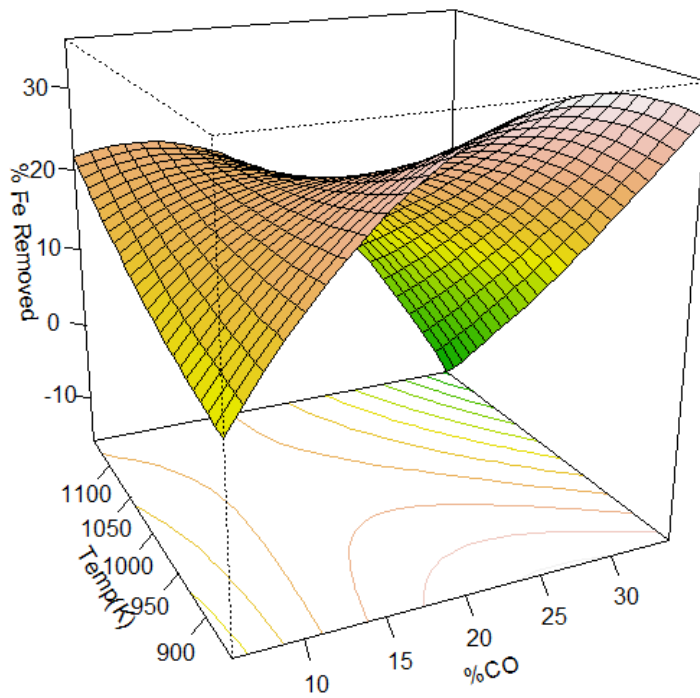

Figure 4.18 – Response surface for percentage Fe removed

From Figure 4.17 and Figure 4.18, it is evident that the response surface for percentage Fe removed shows a "saddle point" shape. While the response may not be at an optimum at this point, in terms of process control, operating in these conditions is preferred as a change in input does not lead to a significant change in outputs. The stationery point is found at a temperature of 1073K and a CO content of 13,8 vol%. It does also appear like the response approaches a maximum value at lower temperatures and high CO contents. A comparison between experimental percentage Fe removed values and calculated values in shown in Table 4.11 below. It can be seen that the percentage difference between calculated and experimental values is high for tests 4 and 8. These two tests had very high Mn recoveries and a very low mass split to the magnetic stream.

Table 4.11 - Comparison between experimental percentage Fe removed values and calculated percentage Fe removed values

std.order	x1	x2	T (K)	Reductant	Experimental %Fe removed	Calculated %Fe removed	% Difference
1	-1	-1	900	10	19.84	17.59	-11.31
2	1	-1	1100	10	18.12	21.11	16.50
3	-1	1	900	30	34.50	28.52	-17.31
4	1	1	1100	30	1.67	0.93	-44.09
5	-1.41	0	858.58	20	27.66	32.85	18.77
6	1.41	0	1141.42	20	18.03	15.82	-12.26
7	0	-1.41	1000	5.86	14.16	13.01	-8.08
8	0	1.41	1000	34.14	2.35	6.48	175.46
9	0	0	1000	20	22.98	22.71	-1.21
10	0	0	1000	20	22.43	22.71	1.24

4.4.3 Mn loss model

The model for the percentage Mn lost is as follows.

$$Percentage\ Mn\ lost = 8,82 - 1,09x_1 - 1,92x_2 - 2,91x_1x_2 + 0,45x_1^2 - 2,28x_2^2 \quad 4.10$$

Where:

$$x1 = \frac{T - 1000}{100} \quad\quad 4.2$$

$$x2 = \frac{\frac{CO}{CO+CO2} - 20}{10} \quad\quad 4.3$$

The statistical analysis of the developed model yielded an R^2 = 0,910, an adjusted R^2 = 0,799 and a lack of fit (Pr >F) = 0,064. Again, the adjusted R^2 remains reasonably high and for this model the lack of fit is not significant.

The contour plot and response surface developed for the percentage Mn lost is shown in Figures 4.19 and 4.20. A similar response is observed for the percentage Mn lost as was observed for the percentage Fe removed. Both responses depict a typical "saddle point", however, in the case of the percentage Mn lost; the value should ideally be as low as possible. The response surface for percentage Mn lost has a stationery point at a temperature of 995K and a CO content of 16,1 vol%. As with the other review metrics, a comparison between experimental percentage Mn lost and calculated percentage Mn lost values is depicted in Table 4.12. Again, the significant difference between calculated and experimental values from tests 4 and 8 is noted.

Table 4.12 - Comparison between experimental % Mn lost values and calculated % Mn lost values

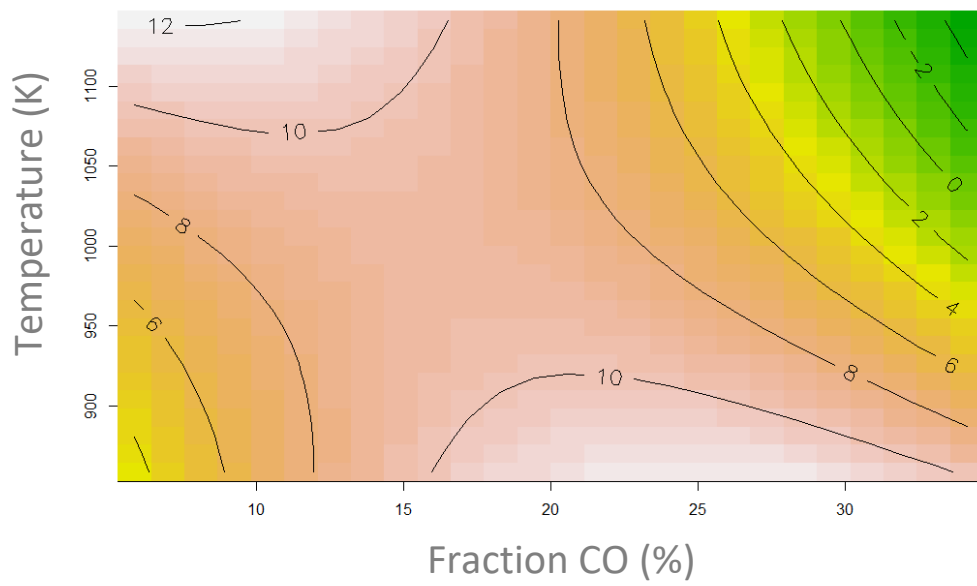| std.order	x1	x2	T (K)	Reductant	Experimental %Mn lost	Calculated %Mn Lost	% Difference
1	-1	-1	900	10	7.73	7.09	-8.26
2	1	-1	1100	10	9.37	10.73	14.54
3	-1	1	900	30	10.80	9.07	-15.97
4	1	1	1100	30	0.78	1.06	35.28
5	-1.41	0	858.58	20	9.67	11.26	16.51
6	1.41	0	1141.42	20	9.40	8.17	-13.12
7	0	-1.41	1000	5.86	7.56	6.98	-7.75
8	0	1.41	1000	34.14	0.59	1.54	160.75
9	0	0	1000	20	8.94	8.82	-1.30
10	0	0	1000	20	8.71	8.82	1.33

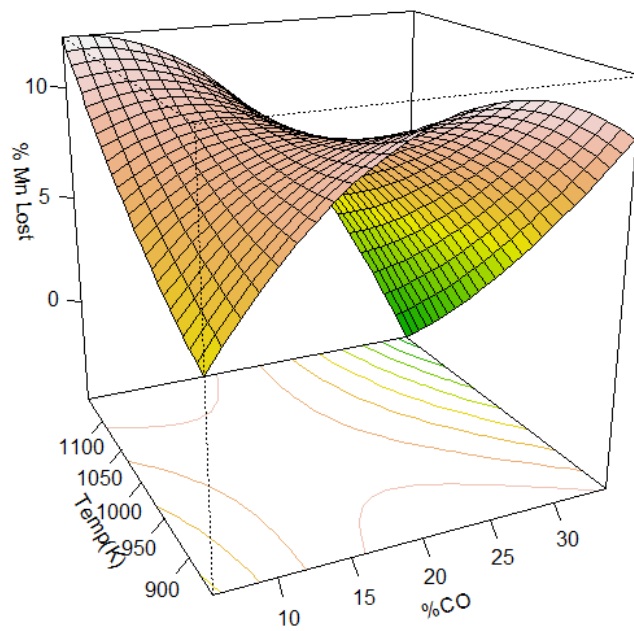*Figure 4.19 – Contour plot for the percentage Mn lost*

Figure 4.20 – Response surface for percentage Mn lost

4.5 Optimization with desirability functions

Desirability functions are a method of simultaneously optimizing for several response variables. This technique was popularized by Derringer & Suich, (1980). The general approach to apply this method is to convert each response variable, y_i, into a desirability function, d_i, with a value between 0 and 1.

$$y_i \rightarrow 0 < d_i < 1$$

The output of the desirability function, d_i, is 1 if the response variable is at its goal or target, or 0 if the response is outside an acceptable region. The individual desirability functions can be set to maximise, minimise, or achieve a specific value of the response variable. The objective is to maximise the overall desirability, D.

$$D = (d_1 \cdot d_2 \cdot d_3 \dots d_m)^{\frac{1}{m}} \qquad\qquad 4.11$$

Where:

- m – number of responses

As the overall desirability function, D, is a product of the individual desirability functions, d_i, it will be 0 if any of the individual responses is undesirable.

Forms of desirability functions

If the aim is to maximise a response variable, the individual desirability can be calculated with the following expression.

$$d = \begin{cases} 0 \ if \ y < L \\ \left(\frac{y-L}{T-L}\right)^r \ if \ L < y < T \\ 1 \ if \ y > T \end{cases} \qquad\qquad 4.12$$

Where:

- y – response variable
- T – Target
- L – Lower limit
- r – weight/scale of each response

In a similar manner, to minimise a response, the individual desirability can be calculated with the following expression:

$$d = \begin{cases} 0 \; if \; y > U \\ \left(\dfrac{U-y}{U-T}\right)^r \; if \; T < y < U \\ 1 \; if \; y < T \end{cases} \qquad 4.13$$

Where:

- y – response variable
- T – Target
- U – Upper limit
- r – weight/scale of response

There does exist an expression to calculate the value of d if the aim is to optimize to a particular value of a response, however, it is not included in this work, as only the maximise and minimise expressions are used.

4.5.1 Results and discussion

For the application of the desirability function, the responses considered, and relevant values are listed below. The models developed in Section 4.4 were used to obtain values for the different responses. Individual desirability's were then calculated using these values.

- Percentage Fe Removed – Maximise
  - L = 25%
  - T = 35%
  - r = 1

- Mn/Fe ratio – Maximise
  - L = 3.3
  - T = 3.8
  - r = 1

- Percentage Mn Lost – Minimise
  - U = 10%
  - T = 0.5%
  - r = 1

The analysis was then coded using R Studio to yield the following desirability plot.

Desirability Function
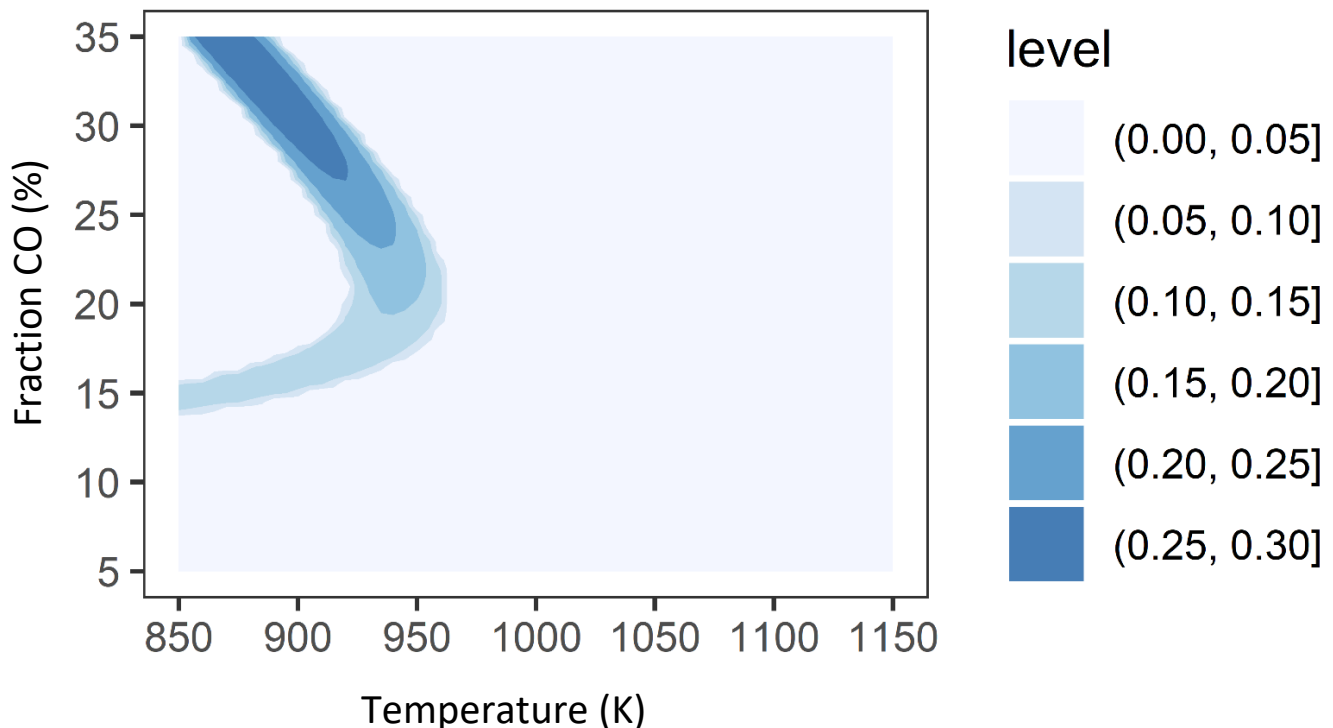
Figure 4.21 - Calculated overall desirability value for the 3 considered responses at different temperatures and reductant ratios

From Figure 4.21, much of the area contains a desirability value of 0 – this indicates that at these conditions, one or more of the responses is at an undesirable value. The highest desirability can be found at low temperatures (850K - 900K) and at high reductant ratios (30-35 vol% CO).

4.6 Reasons for poor observed upgrading of ore

4.6.1 SEM analysis

SEM was carried out to understand the mineralogy of the reduced and magnetically separated samples and to gain insight on the reasons for the poor separation observed between Fe and Mn phases.
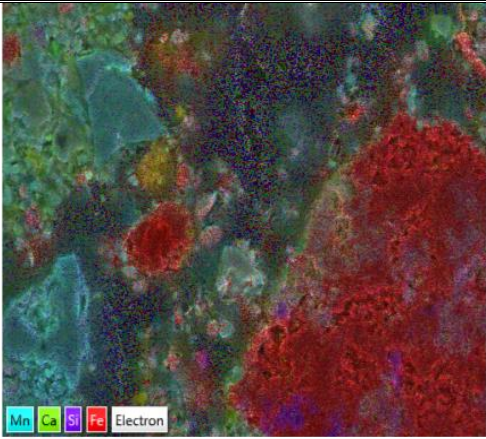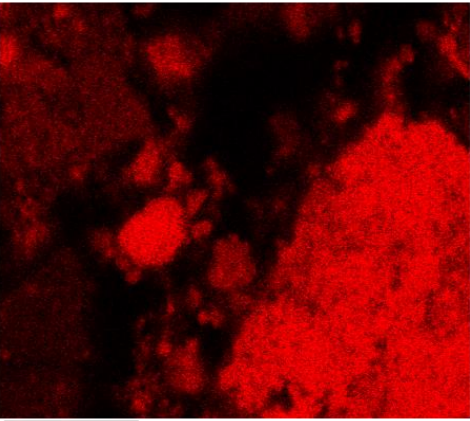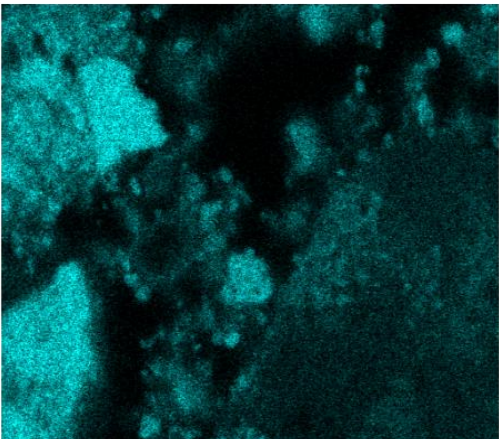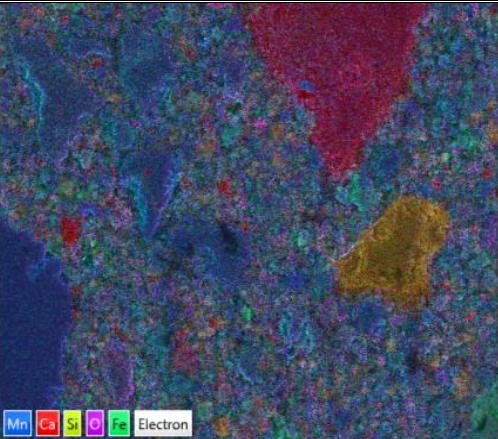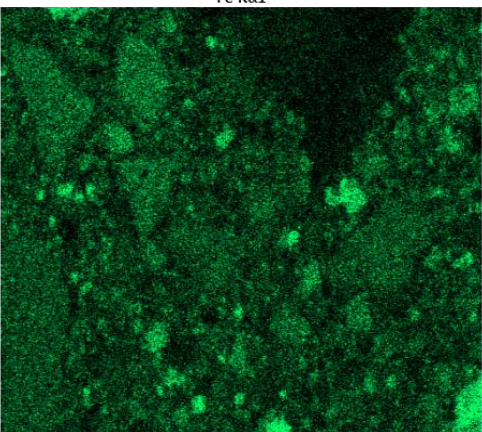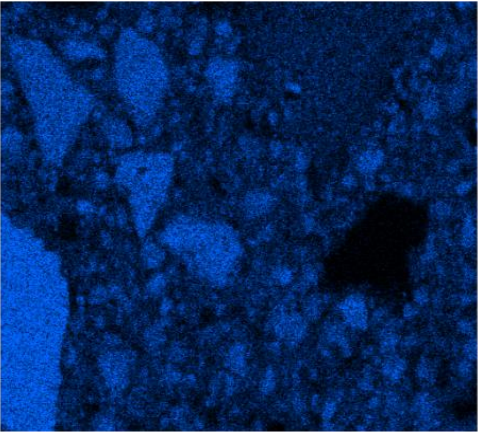
Results and discussion

SEM EDS was used to generate elemental maps of samples to get an overview of the distribution of the different elements within each sample stream. The results are shown in Table 4.13 below. Elemental maps are shown rather than point analyses as the elemental maps highlight the problem faced by the process – solid solution formation.

Considering the non-magnetic stream for the centre point test, a large Mn rich particle is observed (labelled A), however this particle also has considerab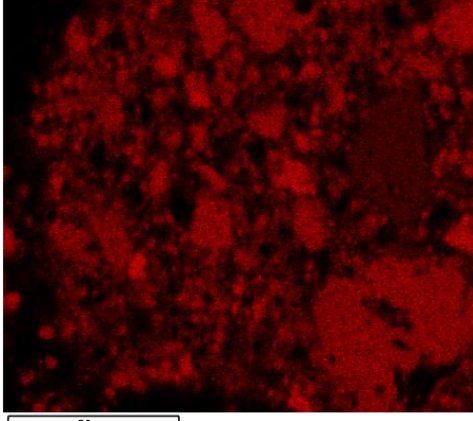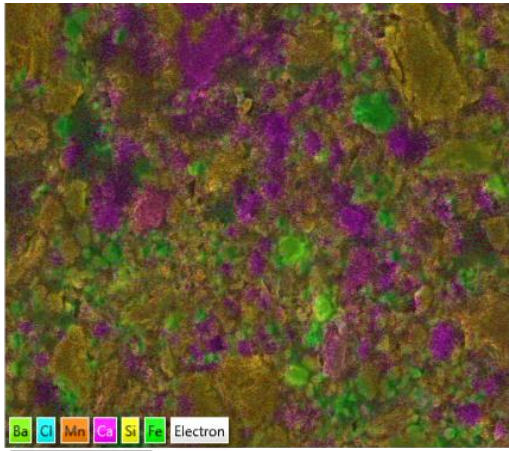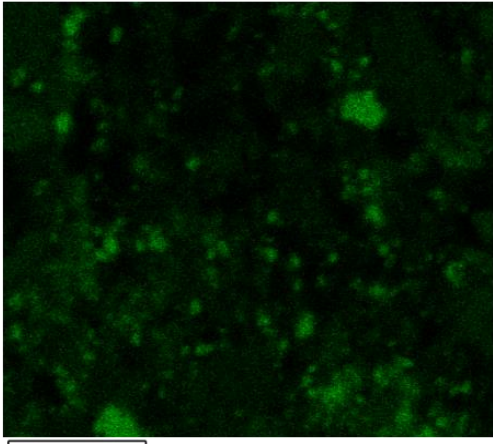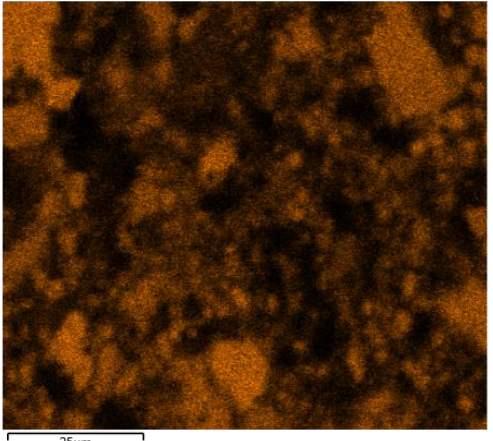le amounts of Fe as evident by the relevant Fe elemental map (a point analysis on this particle indicates that it contains ±35 wt% Mn and ±12 wt% Fe). This issue is observed in all SEM EDS maps that were obtained and is the main reason behind the poor observed separation between Mn and Fe in the magnetic separation process. An investigation was carried out to determine whether the cause of this solid solution formation was due to excessive reduction times, high temperatures or is simply due to the mineralogy of the ore. Details of this investigation are given in Section 4.6.2.

Table 4.13 - SEM EDS maps at different temperatures and CO contents. For each stream (magnetic and non-magnetic streams) the complete elemental map is shown, together with the Fe and Mn elemental maps

Test Number	Test Conditions	Magnetic stream	Non-Magnetic stream
Centre point	1000K, 20 vol% CO		

Test Number	Test Conditions	Magnetic stream	Non-Magnetic stream
Test 6	1141K, 20 vol% CO		

Test Number	Test Conditions	Magnetic stream	Non-Magnetic stream
Test 7	1000K, 5,86 vol% CO	 Fe Kα1 Mn Kα1 	 Fe Kα1 Mn Kα1

4.6.2 Reduction progress tests

In order to confirm the reason for the presence of the solid solution phases observed in Section 4.6.1, reduction progress tests were carried out. These tests helped determine whether the reason for the presence of the solid solution phases can be attributed to excessively long reaction times, high temperatures or whether it is simply due to the mineralogy of the ore. The same sample preparation method, procedure and apparatus used for the optimization study was also used for these tests. Details can be found in Section 4.1.3 and 4.1.4.

The tests were carried out at a fixed CO content of the reducing gas – 30 vol%. This was selected based on the optimized conditions found. The tests were run at different temperatures and for different times at each temperature. Table 4.14 below summarises the different experimental runs that were carried out. After the reduction stage, the reduced samples were then sent for XRD analysis. If the solid solutions phases formed during the reduction process, this would be observed as a shift in the peaks observed on XRD results. This peak shift would indicate a change in lattice parameters caused by the formation of solid solution phases.

Table 4.14 - List of conditions (time and temperature) considered for each test

Test Number	Temperature (°C)	Time (minutes)
1	600	20
2	600	40
3	600	80
4	600	160
5	700	20
6	700	40
7	700	80
8	700	160
9	800	20
10	800	40
11	800	80
12	800	160
13	900	20
14	900	40

15	900	80
16	900	160

Results and discussion

The data obtained from XRD was plotted in Excel to be able to compare the peaks for different tests with each other. The results of the XRD for each temperature is depicted in the figures below.

Figure 4.22 - XRD results of tests at 600°C. Peak identification: 1 - Calcite, 2 - Braunite I/Braunite II, 3 - Jacobsite, 4 - (Fe,Mn)O, 5 - (Fe,Mn)O

Figure 4.23 - XRD results of tests at 700°C. Peak identification: 1 - Calcite, 2 - Braunite I/Braunite II, 3 - Jacobsite, 4 - (Fe,Mn)O, 5 - (Fe,Mn)O

Figure 4.24 - XRD results of tests at 800°C. Peak identification: 1 - Calcite, 2 - Braunite I/Braunite II, 3 - Jacobsite, 4 - (Fe,Mn)O, 5 - (Fe,Mn)O

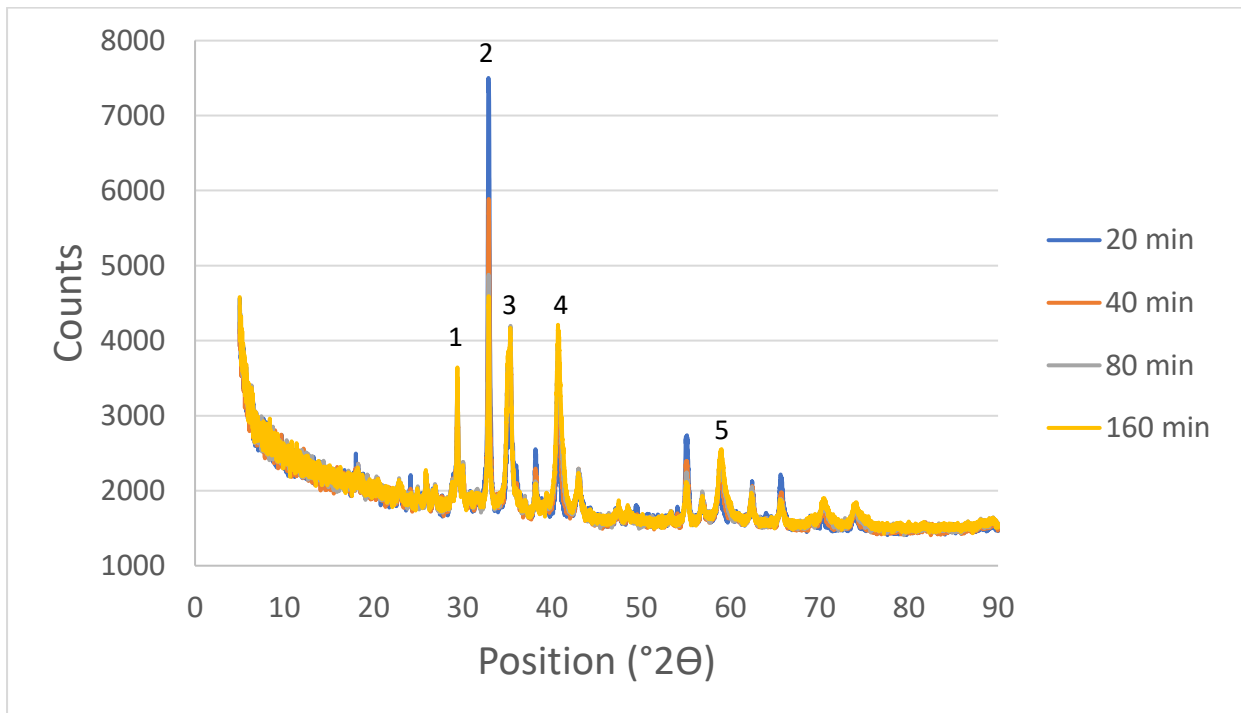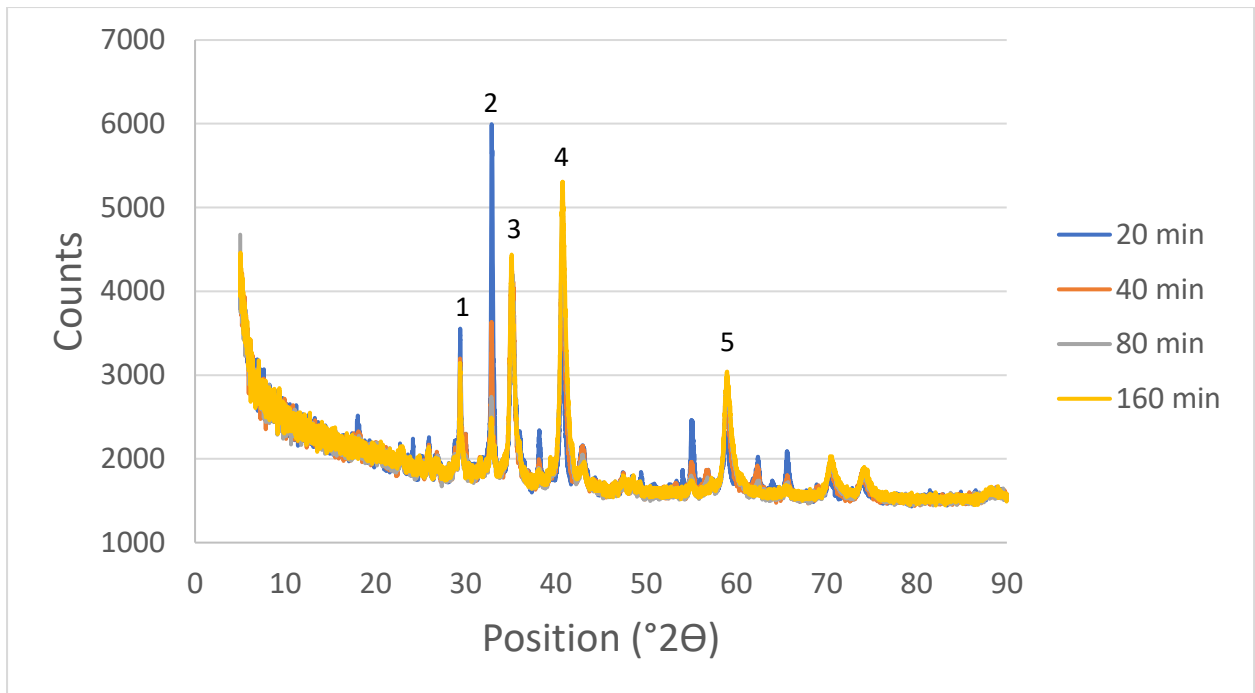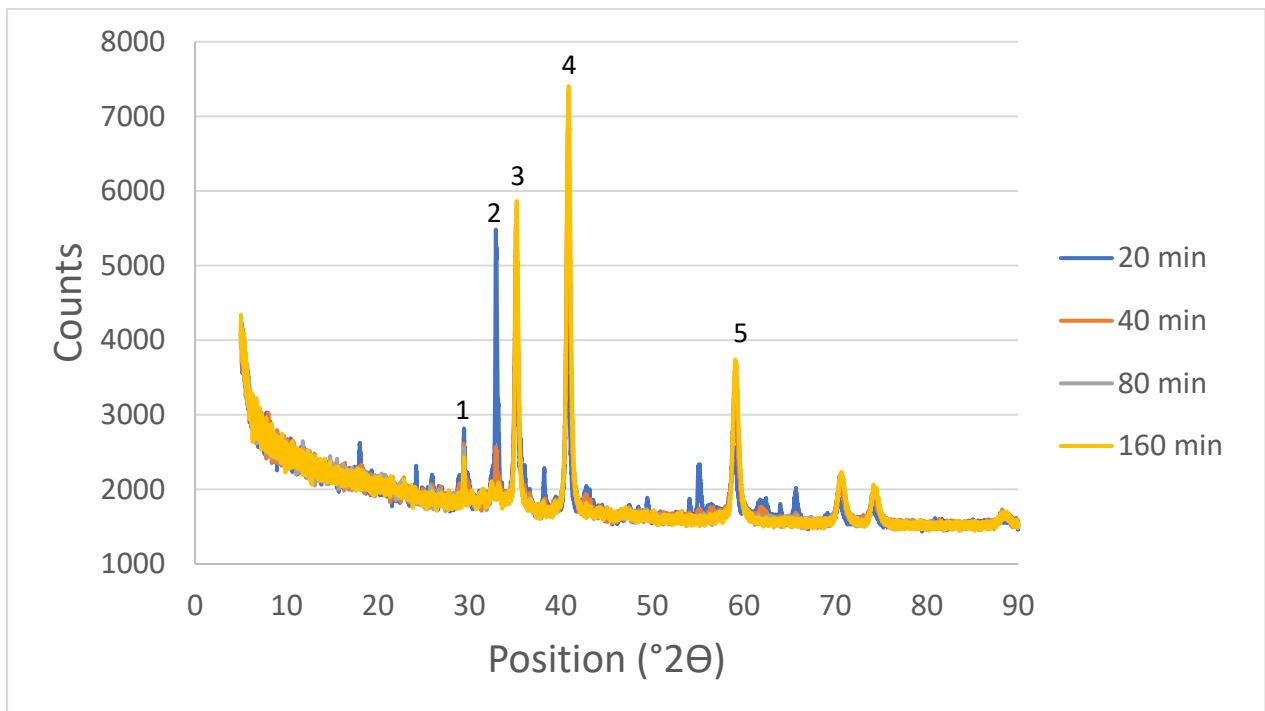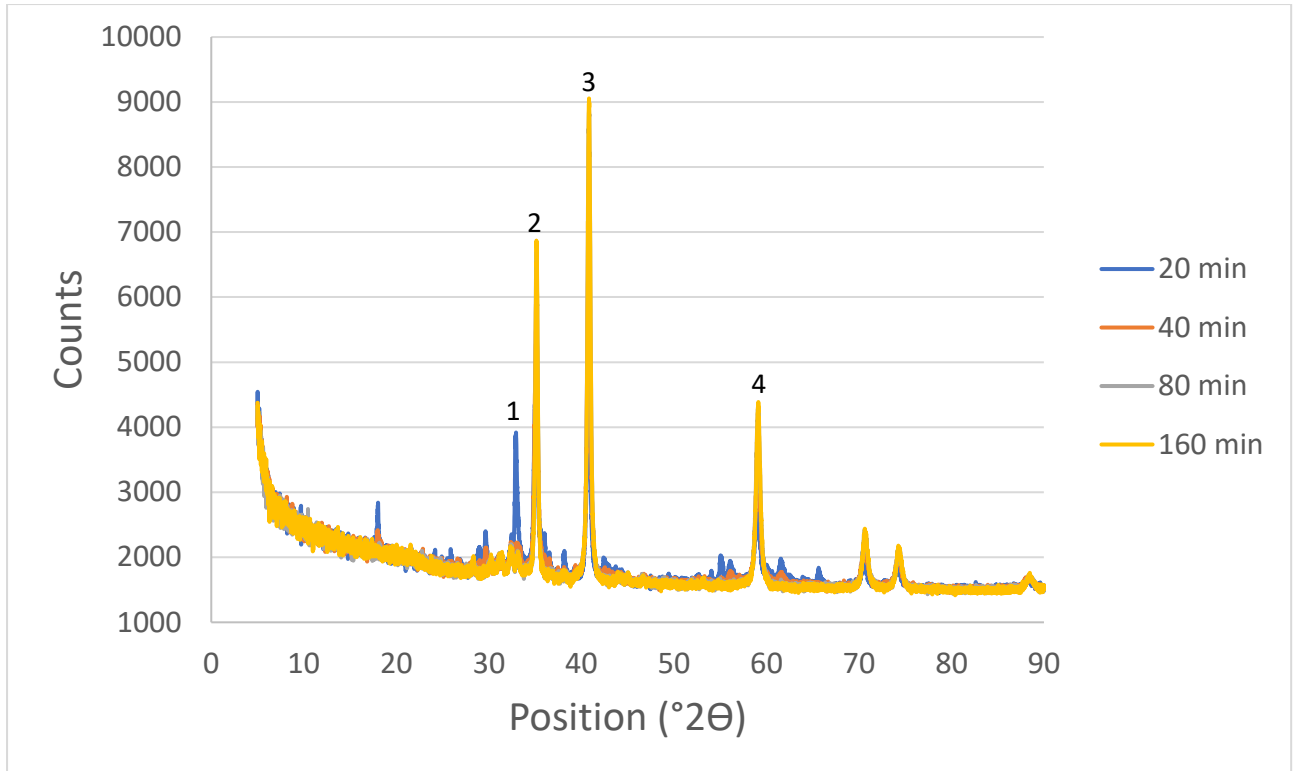*Figure 4.25 - XRD results of tests at 900°C. Peak identification: 1 - Braunite I/Braunite II, 2 - Jacobsite, 3 - (Fe,Mn)O, 4 - (Fe,Mn)O*
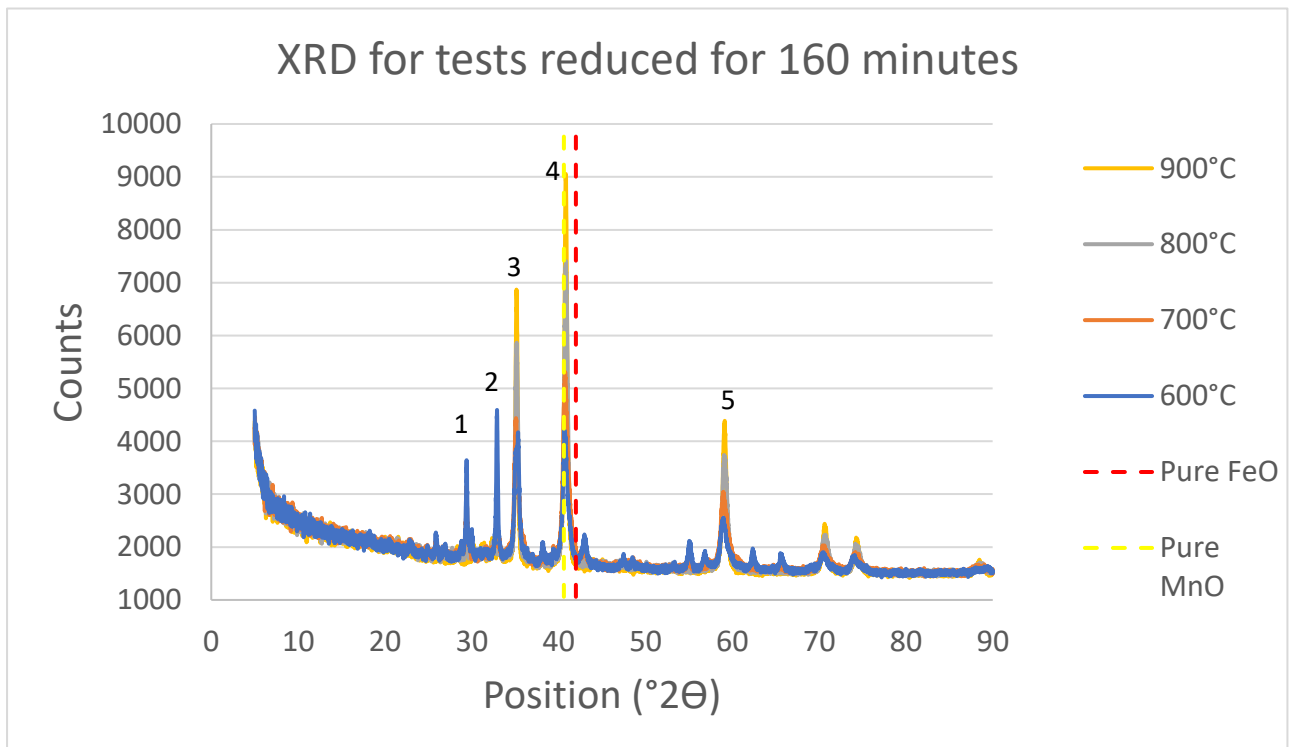

Figure 4.26 - XRD results of tests carried out for 160 minutes. Peak identification: 1 - Calcite, 2 - Braunite I/Braunite II, 3 - Jacobsite, 4 - (Fe,Mn)O, 5 - (Fe,Mn)O

From the figures above, there is no evidence of any significant peak shifts. However, when identifying the best fitting pattern to the measured diffraction pattern, 2 interesting observations were made. The first was that jacobsite ($MnFe_2O_4$) was found to be a better fit to the measured peak than magnetite. Both structures are spinel's, however, the fact that jacobsite fits better than magnetite, indicates that there is significant amounts of Mn in the spinel phase. The second observation was that $Fe_{0.099}Mn_{0.901}O$ was found to be a better fit to the measured diffraction pattern than pure MnO. This is also very significant as it indicates the formation of composite monoxides which would decrease the separation efficiency between Fe and Mn. The positions of the XRD spectra for pure MnO and pure FeO is depicted in Figure 4.26. The position of the identified peaks relative to these theoretical peaks shows that the solid solution phase would likely be richer in Mn than in Fe – which is what was identified. The interesting part of these two observations is that the 2 different phases fit better than the expected phases under all experimental conditions – i.e., at all temperatures and for all times. This indicates that it is the mineralogy of the ore itself that prevents the magnetic separation process from producing a suitable product.

5 Kinetic study on reduction of manganese ore

The determination of the rate controlling mechanism and the development of a kinetic model for the reduction of low-grade ferruginous manganese ores gives insight into the reduction process and allows the prediction of reduction behaviours for combinations of conditions not explicitly investigated by means of an actual experiment.

5.1 Experimental design

5.1.1 Sample preparation

The same cylindrical briquettes used for the optimization study were used for the kinetic study. Details on the briquetting process can be found in Section 4.1.3. An important aspect that had to be considered when preparing samples for the kinetic study, was that there exists relatively large amounts of carbonates and other hydrated phases in the ore. If the briquettes were used directly in the kinetic study, the recorded mass loss would be due to both reduction and calcination. The development of the rate model would then not accurately depict the reduction process. In order to circumvent this issue, the samples were calcined at 900°C for a time period of 1,5 hours in an argon atmosphere. These calcined briquettes were then used for the kinetic study.

5.1.2 Procedure and apparatus

The calcined samples were placed in a mesh basket, separated by pieces of wire that were fashioned into separate bases for each briquette. This was to ensure that all surfaces of each briquette were exposed to the reducing environment. A depiction of the thermobalance used is shown in Figure 5.1. The setup consists of a vertical tube furnace. The sample is attached via a lever to a balance which sends a signal every 5 seconds to a data collector. A gas flow rate of 2.5 Nl/min was maintained to ensure that the supply of reactant didn't become a rate limiting step. The resulting mass loss vs. time curve was used for the kinetic calculations. The furnace was heated up to the relevant temperature and the sample was then loaded into the thermobalance under

an N_2 atmosphere, where it remained for 20 minutes. This gave sufficient time for the sample to heat up to temperature, but more importantly, it gave sufficient time to properly centre the sample in the alumina tube such that the readings on the scale would become stable. After the 20-minute period, the N_2 gas stream was closed, and the reducing gas mixture was introduced. The reduction was then allowed to proceed for 3 hours.

The reduction extent was calculated from the measured mass loss by using Equation 5.1:

$$X = \frac{W_i - W_t}{Theoretical\ mass\ loss}$$ 5.1

Where:

- X – reduction extent
- W_i – initial mass of calcined samples
- W_t – mass of the sample at a specific time

The theoretical mass loss was calculated by assuming complete reduction of all manganese oxides to MnO and all iron oxides to Fe_3O_4. The calculated mass losses from the reduction of the different phases is shown in Table 5.1. For phases such as Braunite I and Braunite II, the amount of Mn_2O_3 in each of the phases was first calculated. The reduction of this Mn_2O_3 to MnO was then used to calculate the mass loss from these phases. The calculation yielded the result of total mass loss due to reduction (described as the removal of all removable oxygen) as 5,76 g/100g sample.

Table 5.1 - Mass loss due to reduction for different phases

Phase	Mass loss(g) (Basis – 98.81 g)	% Mass loss
Hematite – Fe_2O_3	0.458	8,05
Bixbyite – Mn_2O_3	1.25	21,97
Hausmannite – Mn_3O_4	0.157	2.76
Braunite I - $3(Mn,Fe)_2O_3.MnSiO_3$	0.935	16,43
Braunite II - $7(Mn,Fe)_2O_3.CaSiO_3$	2.89	50,79
Total	**5.69**	**100**
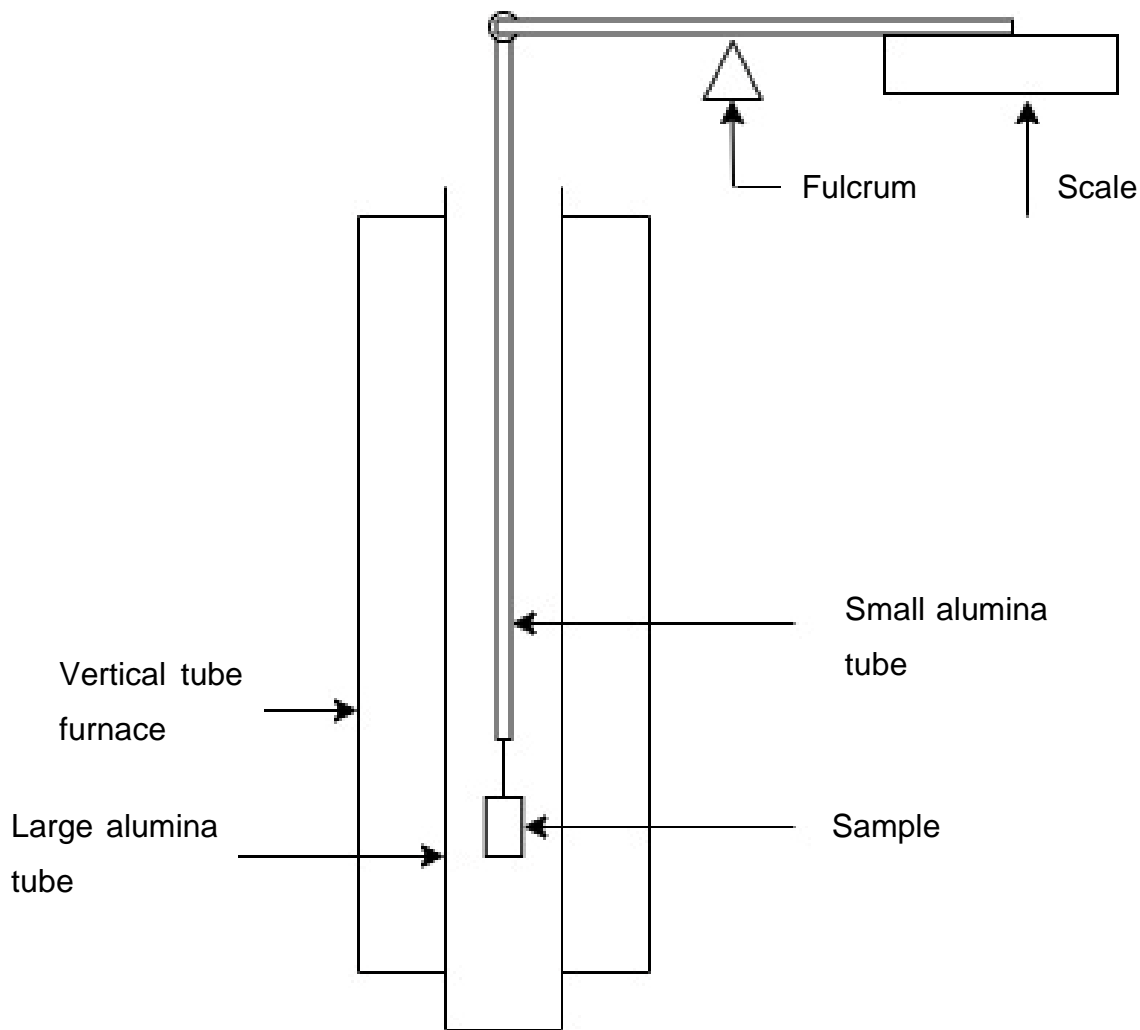
Figure 5.1 - Depiction of the thermobalance setup used

5.2 CO/CO$_2$ kinetic study

The conditions used for the CO kinetic study were the same as those used for the CO optimization study, i.e., the same central composite experimental design was considered. The diagram depicting the central composite design is repeated below for convenience.
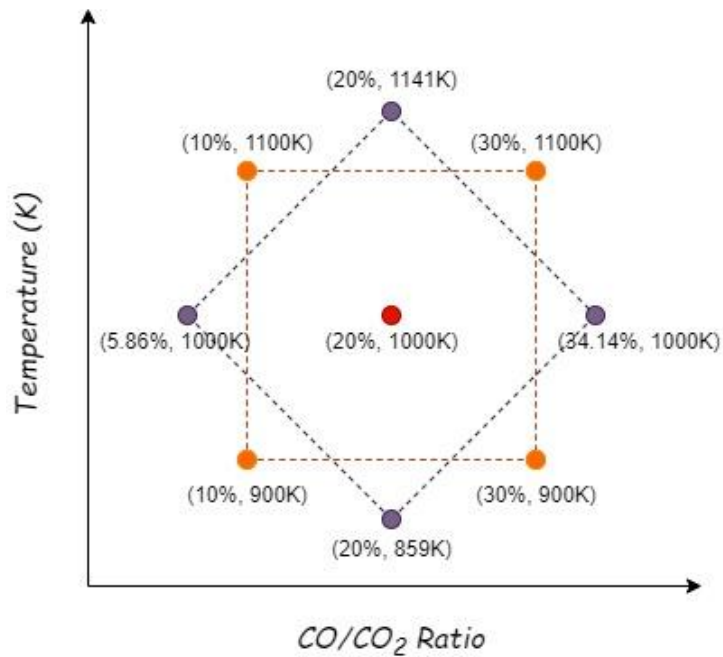
Figure 5.2 - Depiction of the experimental design for the CO/CO$_2$ test

Table 5.2 - List of test runs for CO kinetic study

Std. order	X$_1$	X$_2$	T (K)	T (°C)	Reductant Ratio (CO/CO$_2$)
1	-1	-1	900	627	10
2	1	-1	1100	827	10
3	-1	1	900	627	30
4	1	1	1100	827	30
5	-1.41	0	858.58	586	20
6	1.41	0	1141.42	868	20
7	0	-1.41	1000	727	5.86
8	0	1.41	1000	727	34.14
9	0	0	1000	727	20

5.2.1 Results and discussion

The raw data of each test run, specified by the central composite design, is shown in Figure 5.3. The key for Figure 5.3 is given in the format: Temp (°C), %CO in gas stream.
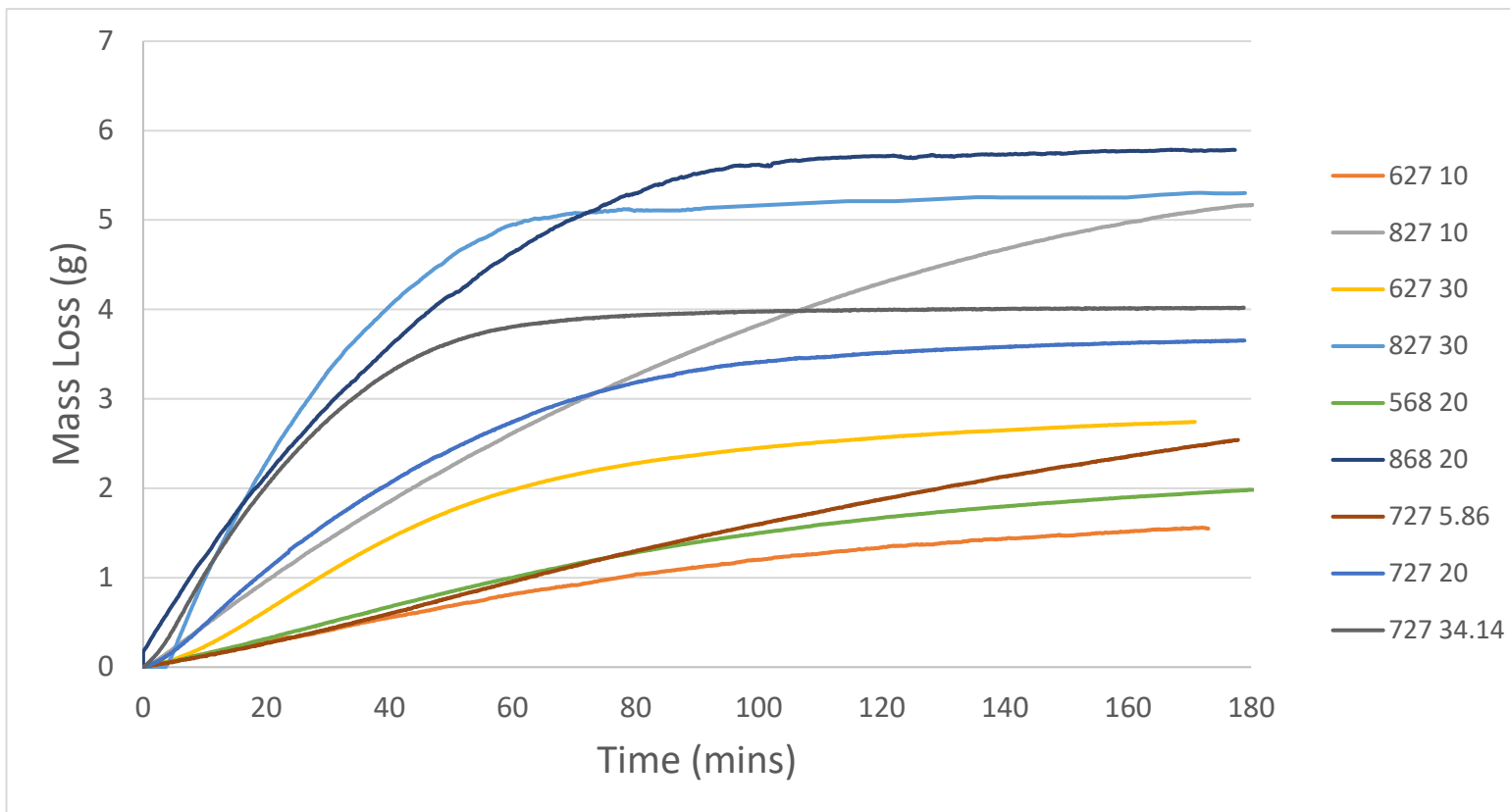
Figure 5.3 - Raw data for CO kinetic study in the form of mass loss vs time curves (Key: Temp (°C), vol% CO)

Reproducibility of experiments

The reproducibility of the kinetic experiments was tested by employing the conditions represented by the centre point of the central composite design, i.e., a temperature of 1000 K and a CO content of 20%. Figure 5.4 indicates that there is little significant difference between original and repeat test in terms of reduction extent.
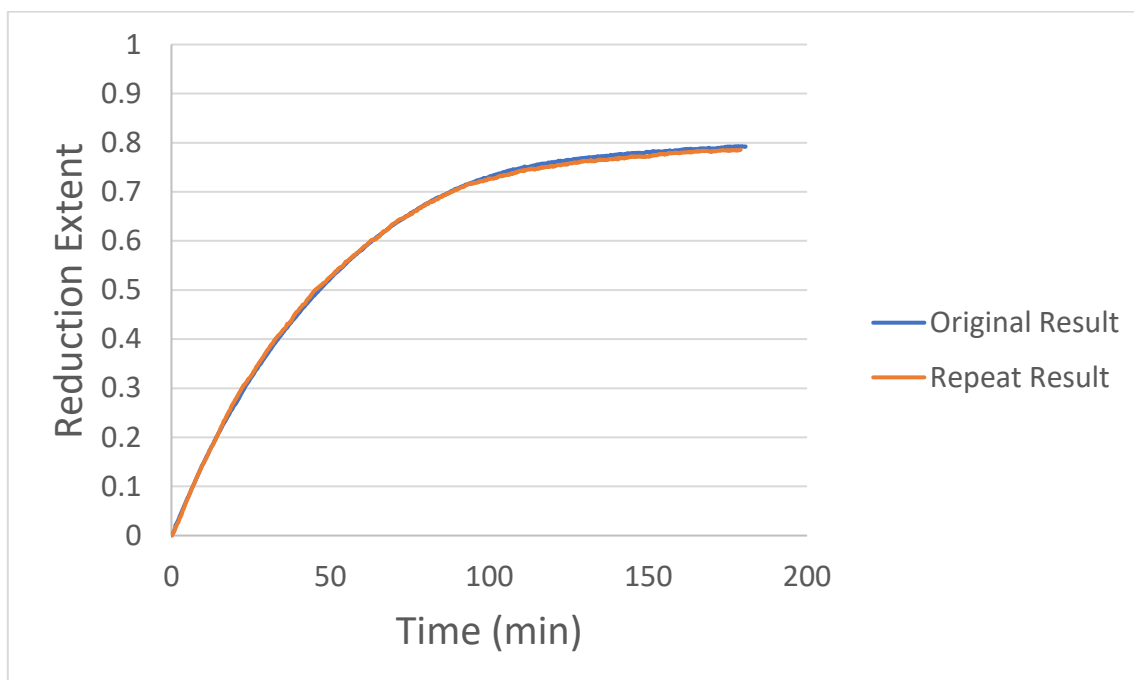
Figure 5.4 - Reduction extent of original and repeat tests

Effect of temperature

The effect of temperature on the reduction process was studied by considering tests 5, 6 and 9 (listed in Table 5.2). These tests were carried out at the following temperatures: 858 K, 1141 K and 1000 K (586 °C, 868 °C and 1000 °C) respectively. The reducing gas for each of these 3 tests was a mixture of CO and CO_2 with a volume ratio of CO/CO_2 = 20/80.

The reduction extent vs. time curves are depicted in Figure 5.5. From these curves it is evident that an increase in temperature leads to an increase in the reduction rate.
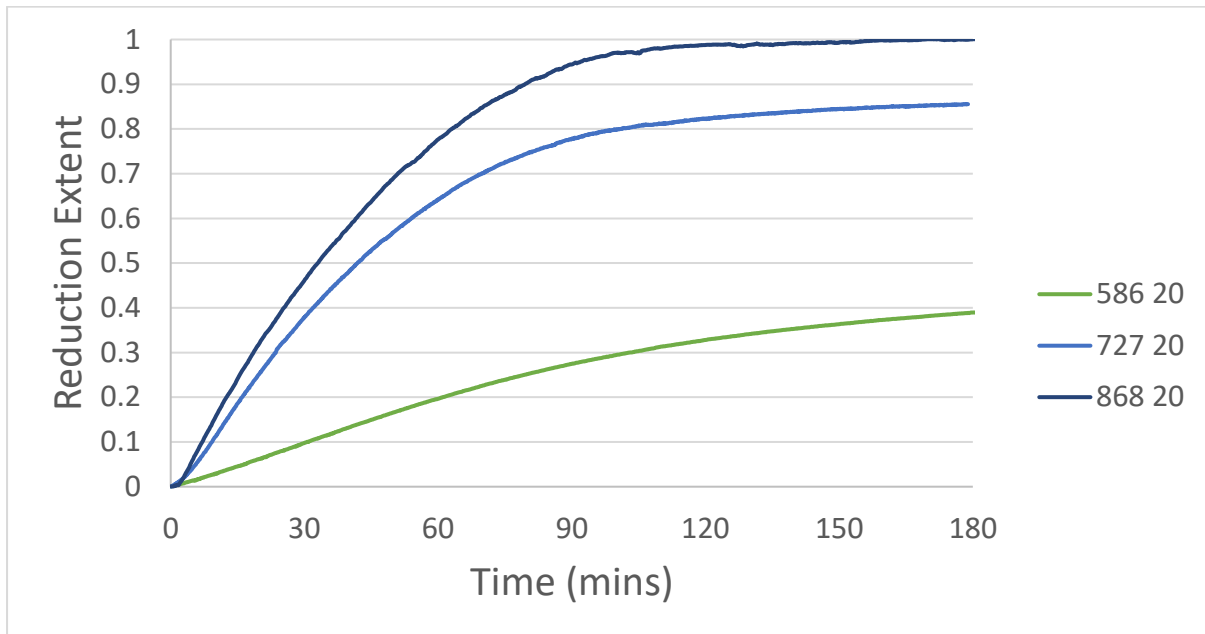
Figure 5.5 - Reduction extent vs time for isothermal tests at different temperatures. CO content = 20 vol% (key – Temp(°C), vol% CO)

Figure 5.5 indicates that the rate of reaction increases to a larger extent when the temperature is increased from 586°C to 727°C than it does when the temperature is increased from 727°C to 868°C. This indicates that the effect of temperature on the rate of reduction decreases at higher temperatures.

Effect of CO content

The effect of CO content on the reduction process was observed by considering tests 7, 8 and 9; listed in Table 5.2. These isothermal tests were carried out at 1000K (727°C), under different CO/CO_2 volume ratios – 5,86 vol% CO, 20 vol% CO and 34,14 vol% CO.

The reduction extent vs time curves are depicted in Figure 5.6.
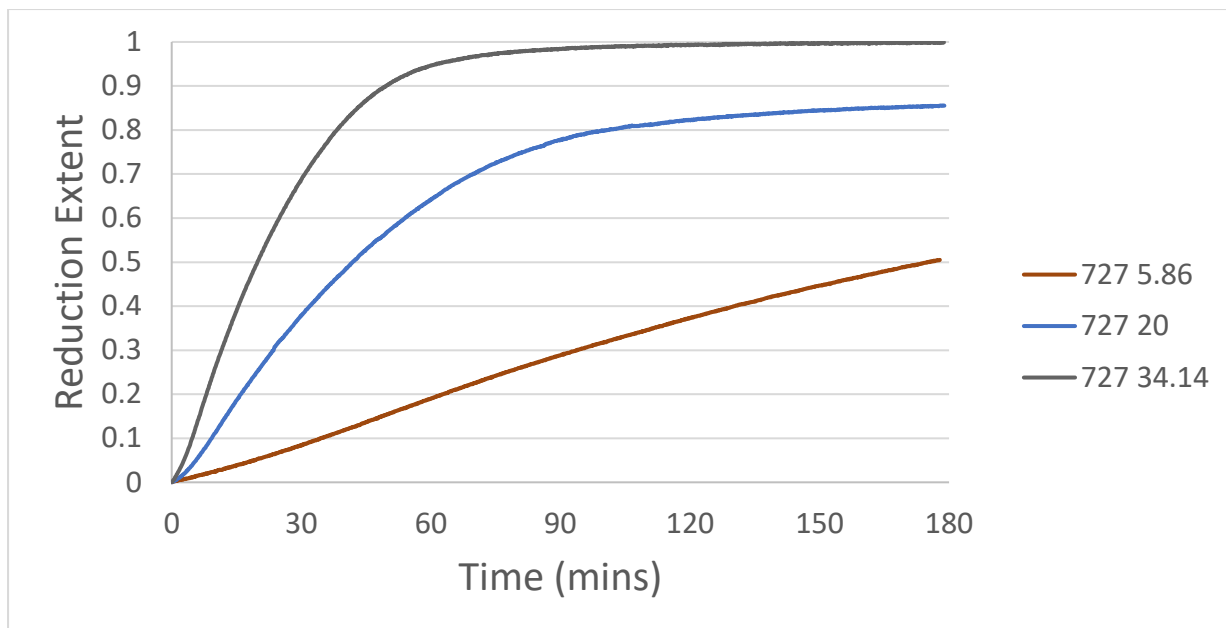
Figure 5.6 - Reduction extent vs. time curve for isothermal tests at different CO contents. Temperature = 727°C (key - Temp (°C), vol% CO)

From Figures 5.6, it is evident that as the CO content increases, the rate of reduction also increases. The reduction also reaches completion a lot faster with a higher CO content. This is likely due to a higher driving force for the reaction (a more negative ΔG caused by a higher CO concentration) or a higher concentration gradient (dC/dx). This data indicates that the reaction is not activation controlled.

5.2.2 Kinetic analysis

The reduction reaction can be controlled by various mechanisms, most importantly, by chemical reaction control, diffusion control, or by nucleation and growth. For the purposes of this analysis, it was assumed that the reaction would represent a shrinking core model and that each individual particle could be considered a sphere, i.e., having the same dimensions in all directions and therefore, having the same reactivity in all directions. By making these assumptions, the following rate equations could be considered.

Table 5.3 - Rate equations for different rate controlling mechanisms

Rate controlling mechanism	Integral form $g(X) = kt$
Chemical reaction control	$1 - (1 - X)^{1/3}$
Diffusion control – Jander model	$(1 - (1 - X)^{1/3})^2$
Nucleation and growth – Avrami model	$(-\ln(1 - X))^{1/n}$

In order to determine which of the rate equations best fit the experimental data, 2 methods were applied:

Firstly, the rate models were linearized and plotted against time or ln(t) depending on the model. If the model fit the data, this linearization would result in a linear plot. If the reduction was controlled by chemical reaction, a plot of $[1 - (1 -X)^{1/3}]$ vs time would result in straight lines, if the reaction was controlled by diffusion, a plot of $[(1 - (1 - X)^{1/3})^2]$ vs time would be linear and if the reaction was controlled by nucleation and growth, a plot of $[\ln(-\ln(1-X))]$ vs ln(t) would be a straight line. The plots of these linearization's are depicted in Figures 5.7, 5.8 and 5.9 below:

Figure 5.7 - Plots of $1-(1-X)^{1/3}$ vs time to determine suitability of chemical reaction control model to fit experimental data (key – Temp(°C), vol% CO)

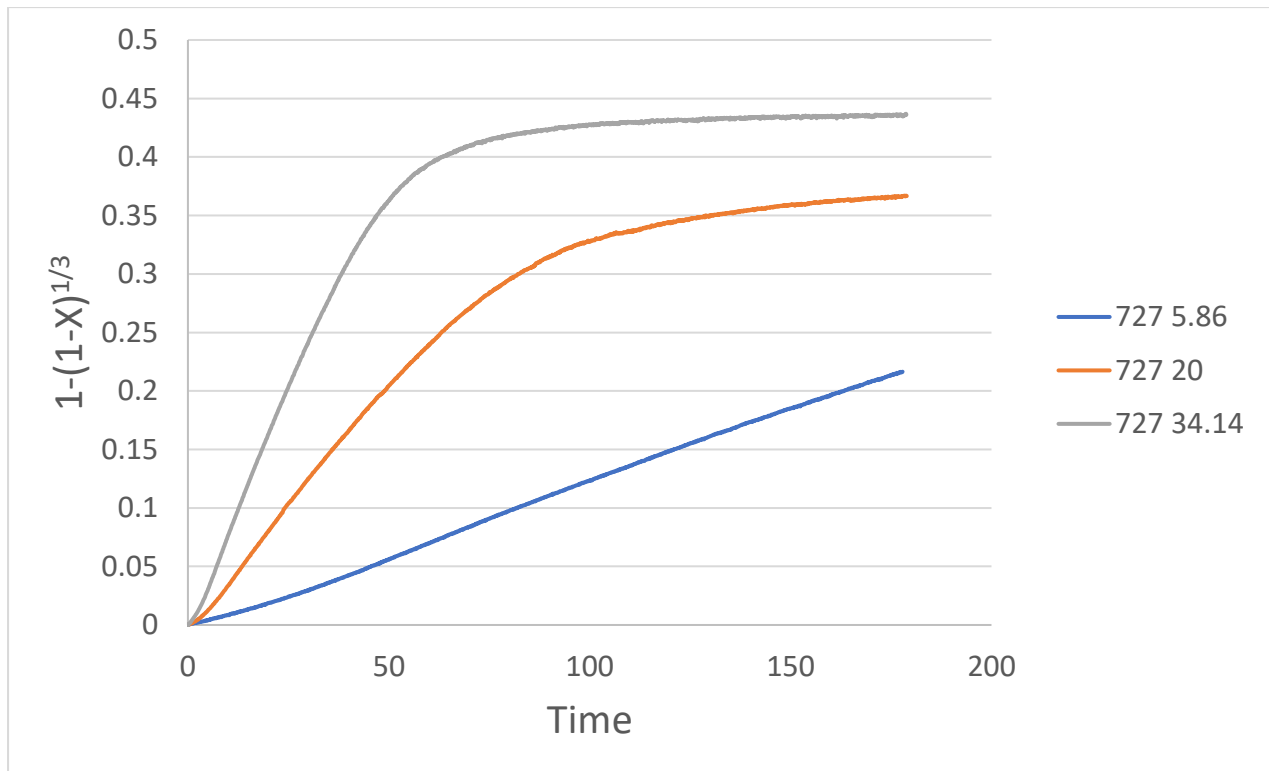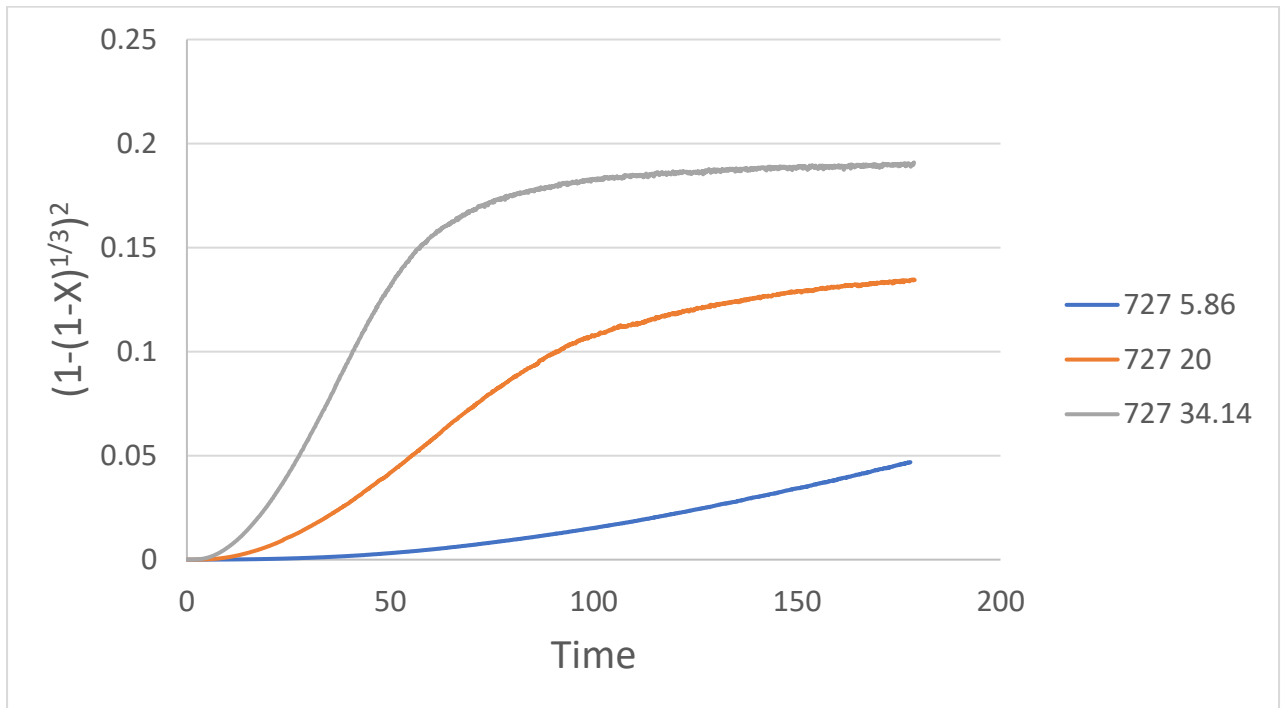*Figure 5.8 - Plots of $(1-(1-X)^{1/3})^2$ vs time to determine the suitability of the Jander model to fit experimental data (key – Temp(°C), vol% CO)*
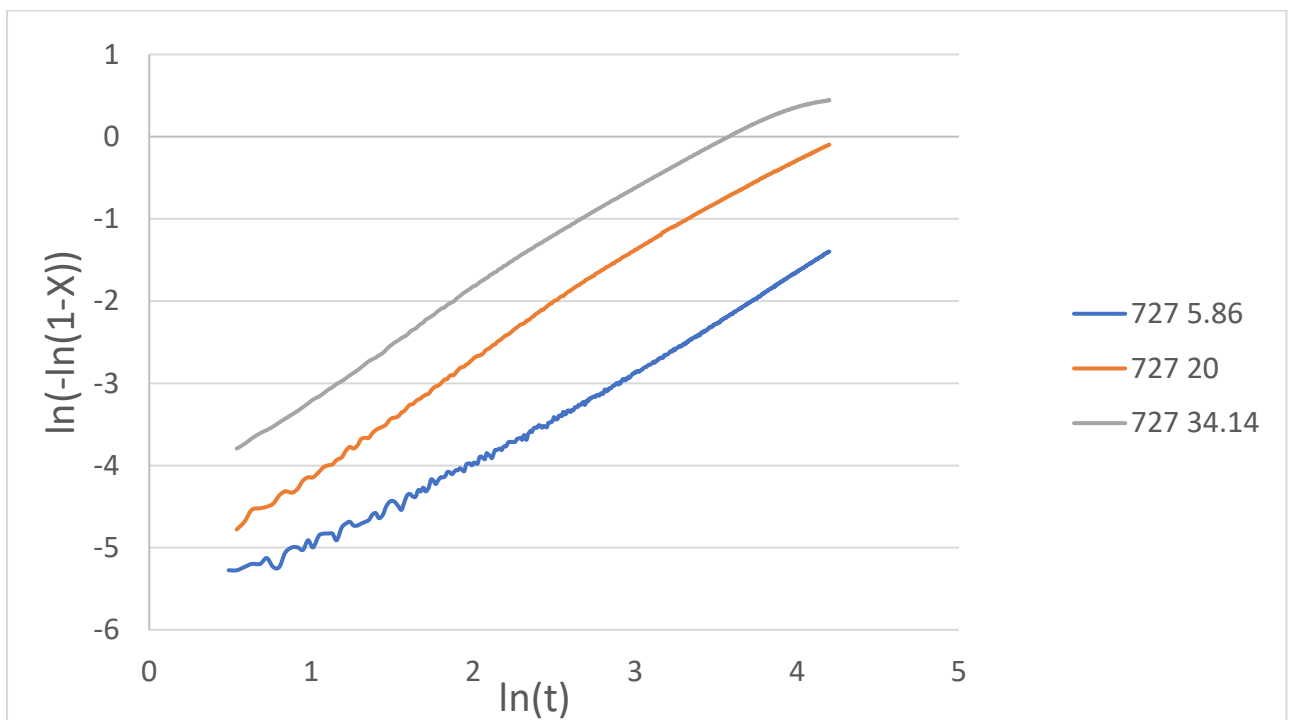

Figure 5.9 - Plots of $\ln(-\ln(1-X))$ vs $\ln(t)$ to determine the suitability of the Avrami model to fit experimental data (key - Temp(°C), vol% CO)

From Figures 5.7, 5.8 and 5.9, it is evident that the reduction reaction is likely controlled by nucleation and growth, as the linearisation of the Avrami model is the only model that resulted in approximately straight lines under all conditions. In order to confirm this, a second method was applied to fit the 3 models described above. This second method involved a minimization of the Sum Squared Error (SSE) using Excel. The data used to fit the models is from the centre point of the central composite design – 727°C and 20 vol% CO.

The plots of the experimental data vs time and calculated data vs time are depicted below:
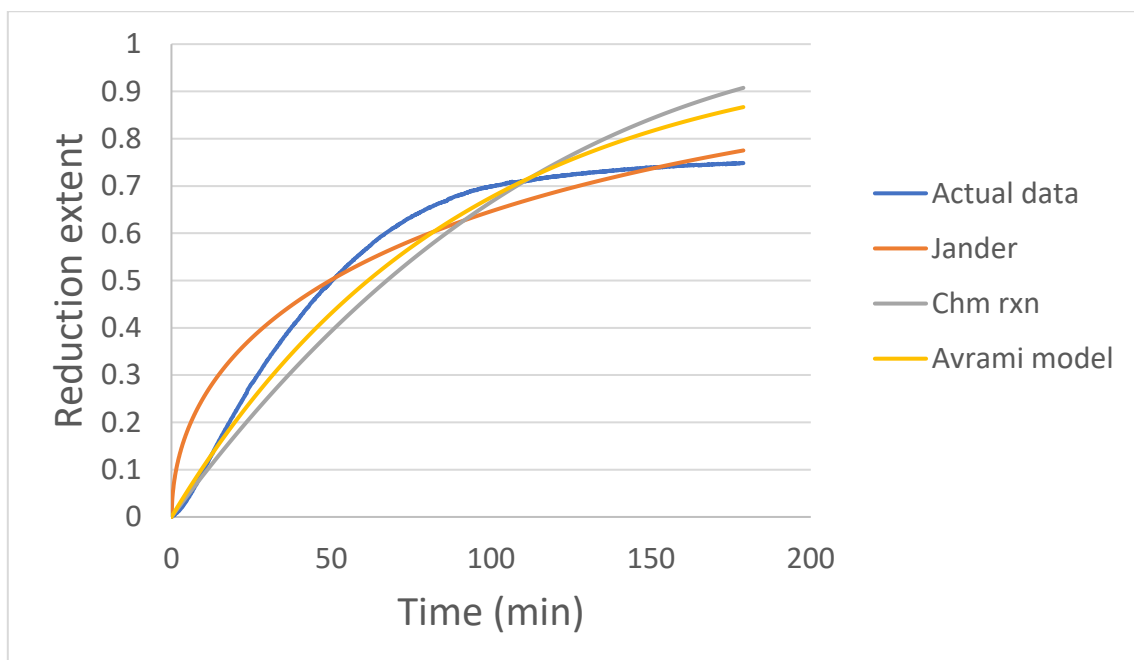
Figure 5.10 - Best fit of the 3 models considered compared with actual data

From Figure 5.10, it is evident that the reaction is likely best modelled by the Avrami model. The Jander model predicts a very rapid initial reaction rate, where it overestimates the experimental data. This is then followed by a rapid decline in the reaction rate, and a slight underestimation of the experimental data. Both, the chemical reaction control model and the Avrami model, follow a similar trend – both models underestimate experimental data initially and then overestimate the experimental data. The Avrami model estimations are, however, a more accurate depiction of the experimental data. A plot of the percent error (Figure 5.11) and a plot of the

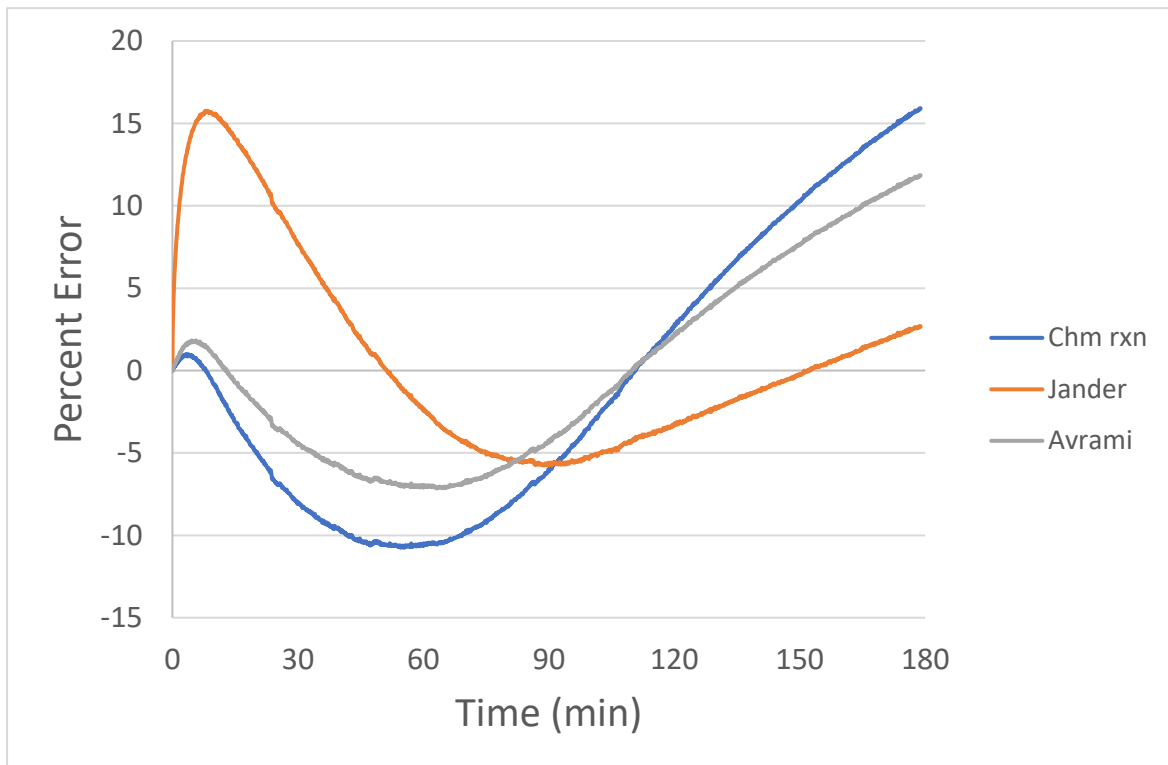experimental data vs calculated data (Figure 5.12) for each of the 3 models was also made to depict these trends.

Figure 5.11 – Percent error vs time for the 3 evaluated models (Error = Calculated value - Experimental value) at the centre point of the central composite design (727°C, 20 vol% CO)

.

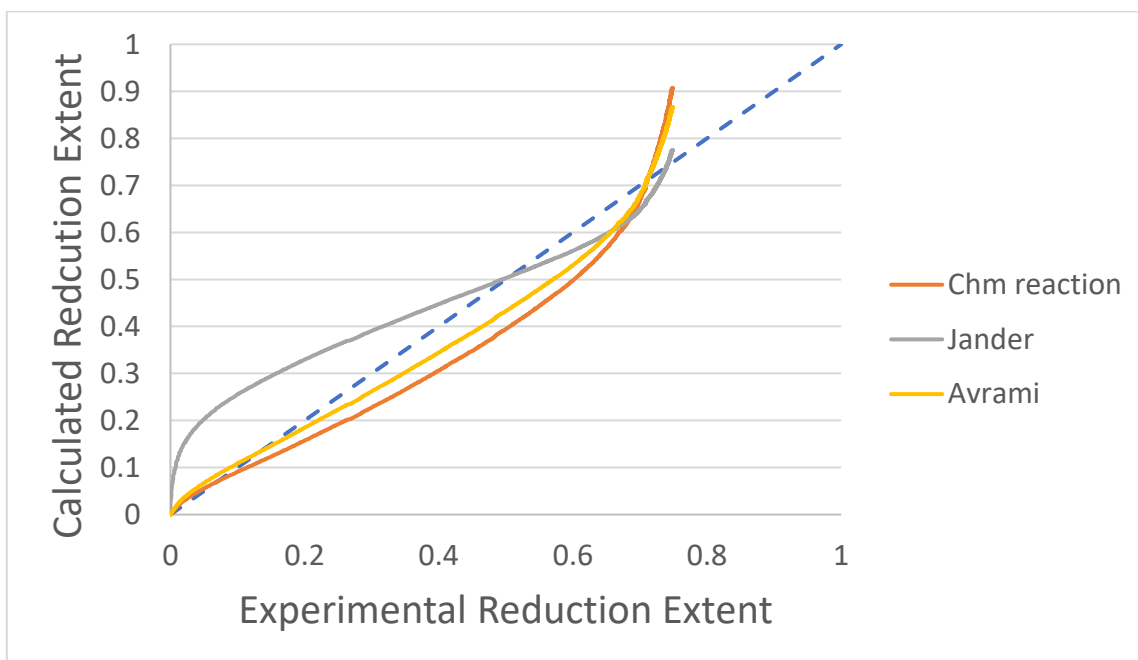*Figure 5.12 - Experimental value vs Calculated value at the centre point of the central composite design (727°C, 20 vol% CO)*

From the 2 model fitting methods described above, the best fit for the experimental data was the Avrami model (it should be noted that the selection of the Avrami model is based solely on the model fitting methods described, and may not be the actual reaction mechanism), which is used to describe a nucleation and growth rate limited process. The Avrami model, also known as the Kolmogorov-Johnson-Mehl-Avrami (JMAK) model describes chemical reactions in terms of 3 processes that occur simultaneously. Firstly, the nucleation of solid domains, also known as "islands", followed by the growth of existing islands and finally, coalescence, which occurs when expanding islands merge. One of the assumptions made in this model is that these islands can nucleate anywhere within the sample (homogenous nucleation). Once an island has nucleated, it grows at a constant velocity in all directions. This velocity remains constant as long as the temperature remains constant. When two neighbouring islands meet and impinge on each other, growth stops at the points of contact, but continues elsewhere (Jun et al., 2005). In terms of the system being investigated, the "solid domains" could be MnO nucleating from manganese oxides or Fe_3O_4 nucleating from Fe_2O_3.

The next step was to determine the variables associated with the Avrami model, which is depicted below:

$$[-\ln(1-X)]^{1/n} = k_{app}t \qquad\qquad 5.2$$

Where:

- X – Reduction extent
- k_{app} – apparent rate constant
- t – time

The apparent rate constant, k_{app}, takes into consideration the effects of the partial pressures of the reducing gas mixture, according to the following equation:

$$k_{app} = k[p_{CO}^m - (\frac{P_{CO_2}}{K})^m] \qquad\qquad 5.3$$

Where:

- k – effective rate constant
- P_{CO} – CO partial pressure
- P_{CO2} – CO_2 partial pressure

- m – reaction order
- K – equilibrium constant

It can be assumed that the value of K (equilibrium constant) for this reduction process will be sufficiently large to result in the contribution of the $(\frac{P_{CO_2}}{K})^m$ term being negligible (for example, the K value for hematite reduction with CO at 1000 K is 42604 J/mol and the K value for the reduction of bixbyite with CO at 1000 K is 3,90 x 10^8 J/mol). This then simplifies the expression for k_{app} to the following:

$$k_{app} = k(p_{CO}^m)$$
<div align="right">5.4</div>

The calculation for the partial pressures of CO and CO_2 is carried out with the following equation:

$$P = P_T X$$
<div align="right">5.5</div>

Where:

- P – partial pressure of either CO or CO_2
- P_T – total pressure. In this case the P_t is taken to be 0,86 atm, which is the atmospheric pressure in Pretoria, South Africa.
- X – volume fraction of either CO or CO_2

In order to determine the value of "n" in the Avrami equation, the plots of [ln(-ln(1 – X)] vs ln(t) at different temperatures were used. These plots are shown in Figure 5.13. The slope of these plots represents the value of the exponent, n.
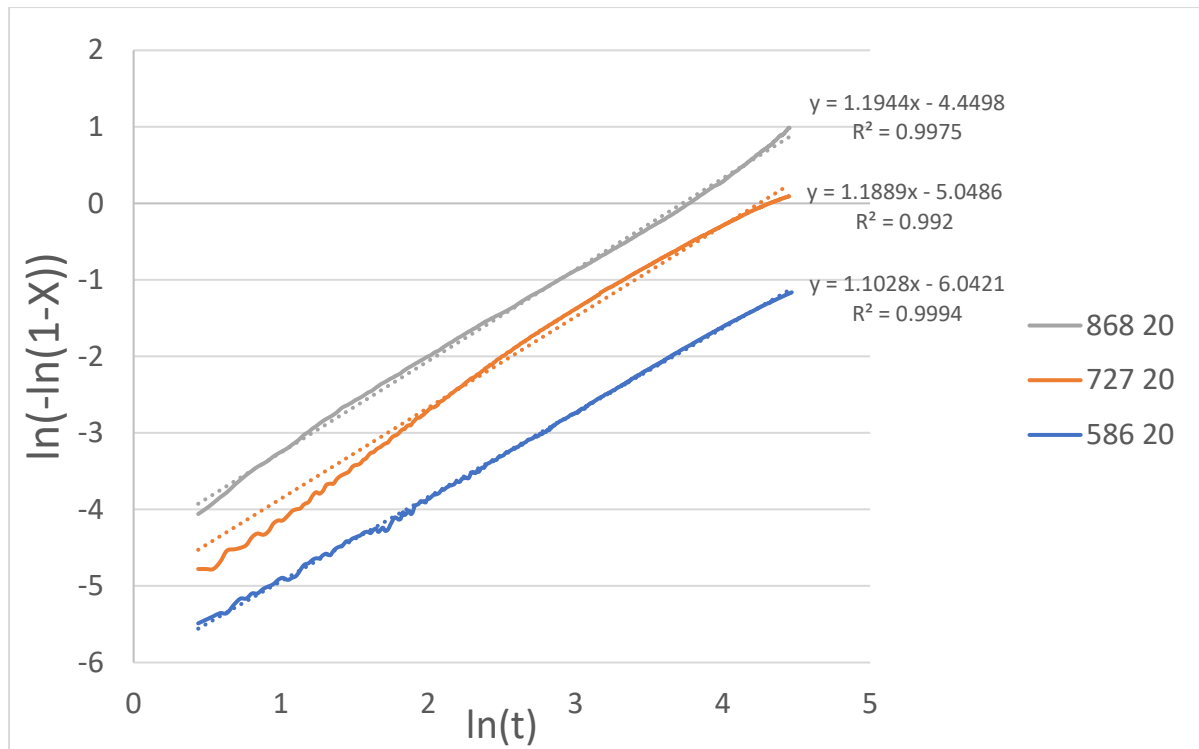
Figure 5.13 - Linearisation plots of Avrami model at different temperatures (constant P_{CO}). Slope used for determination of "n" (key – Temp(°C), vol% CO)

The slopes were from line the of best fit depicted on Figure 5.13.

Table 5.4 - Values of the slope (n) at different temperatures

Temperature (K)	Slope
859 (586°C)	1,103
1000 (727°C)	1,189
1141 (868°C)	1,194
Average	1,163

The value of the exponent "n" is therefore equal to 1,163. This is an indication of one-dimensional nucleation according to the Avrami model.

The next term that was calculated was the exponent "m". In order to determine the value of this, a plot of $\ln(k_{app,CO})$ vs $\ln(P_{CO})$ was made. The value of $\ln(k_{app,CO})$ was determined from the y-intercept of the linearised plots of the Avrami model at different concentrations of CO (constant temperature). This plot is depicted in Figure 5.9 but is repeated in Figure 5.14 with the addition of the best fit lines.
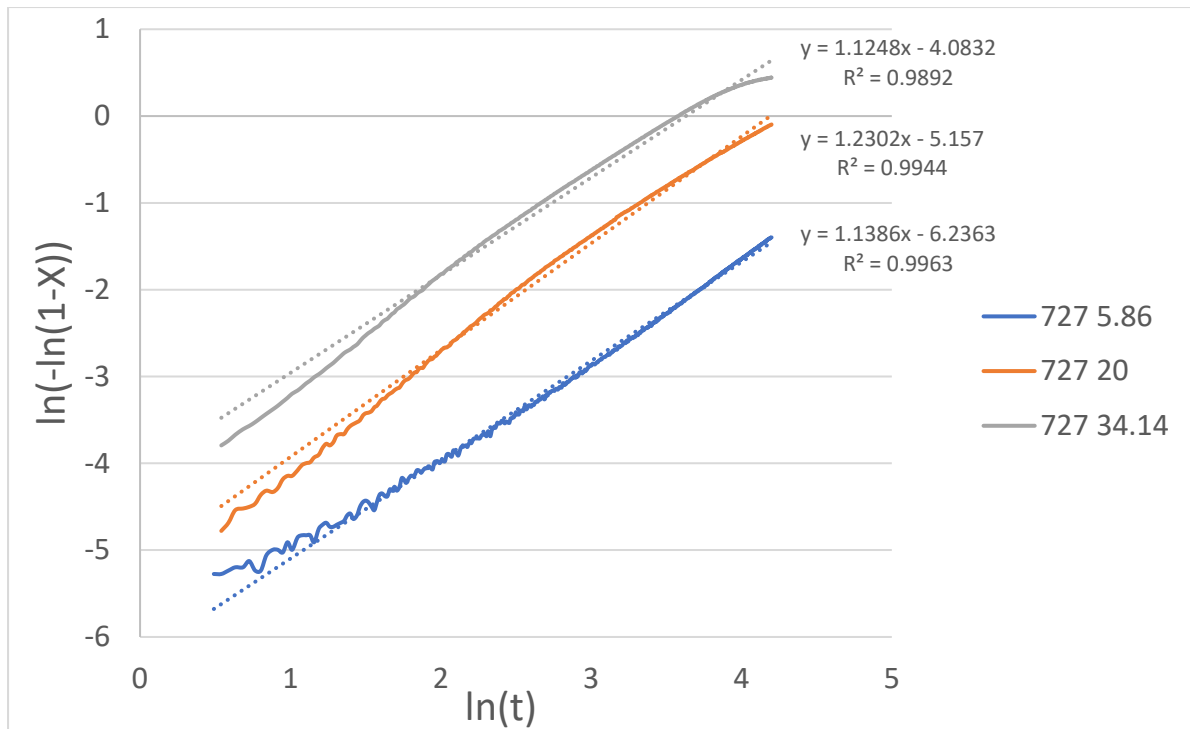
Figure 5.14 - Linearisation plots of Avrami model at different CO contents (constant temperature). Y-int used for determination of "m" (key – Temp(°C), vol% CO)

The values of $\ln(k_{app,CO})$ and those of P_{CO} used for the determination of the exponent "m" are summarised in Table 5.5 below:

Table 5.5 - Values of P_{CO} and $\ln(k_{app,CO})$

Vol% CO	P_{CO}	$\ln(k_{app,CO})$
5,86	0,05	-6,24
20	0,172	-5,16
34,14	0,294	-4,08

*$k_{app,CO}$ in min^{-1}

The values of $\ln(P_{CO})$ and $\ln(k_{app,CO})$, were then plotted. The results are depicted in Figure 5.15.

Figure 5.15 - Plot of ln(p_{CO}) vs ln($k_{app,CO}$) for the determination of the exponent "m"

The slope of the line of best fit of the plot of ln(P_{CO}) vs. ln($k_{app,CO}$) represents the value of the exponent m. From Figure 5.15, this value is taken as 1,1591.

Placing the values of the two exponent terms into the Avrami equations yields the following result:

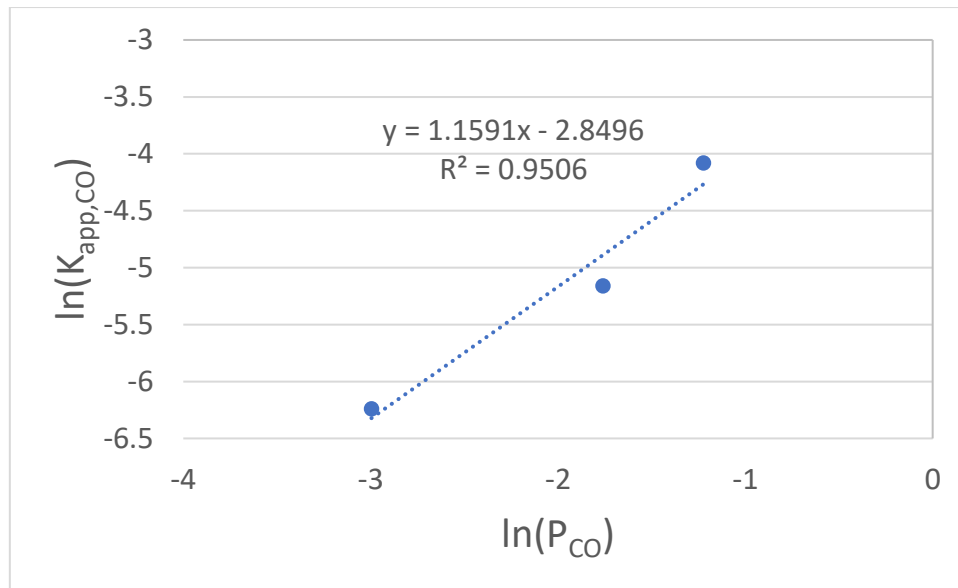$$[-ln\,(1-X)]^{1/1.163} = kP_{CO}^{1,1591}t \qquad 5.6$$

This leaves the determination of k, the effective rate constant. The value of k follows an Arrhenius relationship according to the following equation:

$$k = k_0 e^{\frac{-E_a}{RT}} \qquad 5.7$$

Where:

- K_0 – pre-exponential constant ($atm^{-1}min^{-1}$)
- E_a – Activation energy (J/mol)
- R – Gas constant (J/mol.K)
- T – Temperature (K)

In order to determine the value of k_0 and E_a, Excel's Solver function was used to minimise the Sum Squared Error (SSE) of the fit between the calculated and experimental data. This led to the determination of the 3 different values for k, at different temperatures. A plot of ln(k) vs 1000/T was then made to determine the values of k_0 and E_a, shown in Figure 5.16.

Table 5.6 - calculated values of the effective rate constant at different temperatures

T(K)	k (atm^{-1}min^{-1})
859	0.012049
1000	0.047849
1141	0.102449
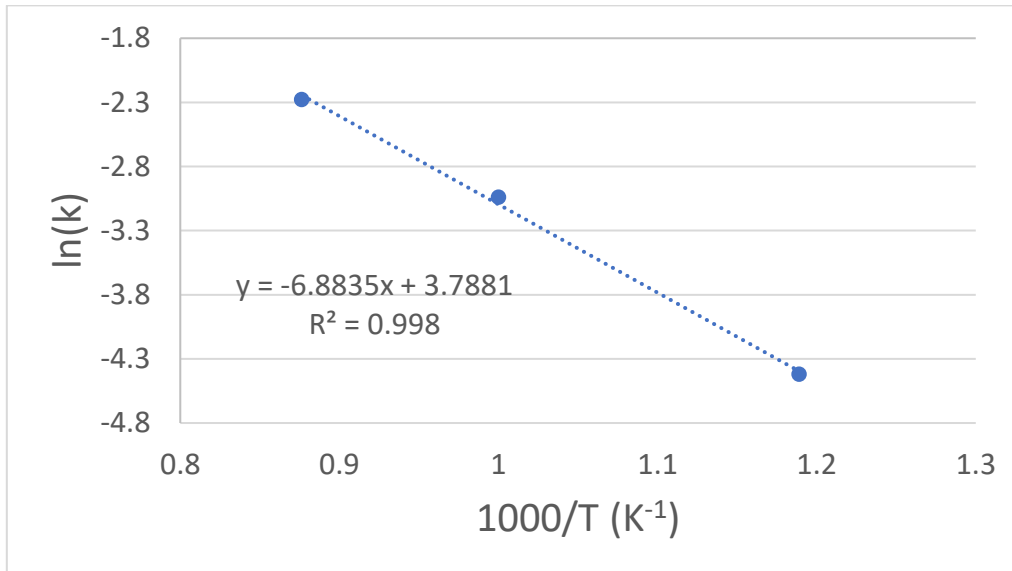
Figure 5.16 - Plot of ln(k) vs 1000/T to determine the values of k_0 and E_a

The value of E_a can be determined from the slope of Figure 5.16, and a value of 57229,4 J/mol is obtained for the activation energy. The value of k_0 is obtained from the y-intercept. The calculated value of k_0 is 44,172 atm^{-1}min^{-1}.

Based on the above kinetic analysis, the overall rate equation for the CO reduction process is as follows:

$$[-ln\,(1-X)]^{1/n} = kP_{CO}^{m}t \qquad\qquad 5.8$$

With:

$$k = k_0 e^{\frac{-E_a}{RT}} \qquad\qquad 5.7$$

Where:

- k_0 – 44,172 atm^{-1}min^{-1}
- E_a – 57229,4 J/mol
- n – 1,163
- m – 1,1591

And the units for t and p_{CO} are minutes and atm, respectively.

5.2.3 Evaluation of model

The figures below compare the actual data and calculated data, considering the points of the central composite design that were not used to fit the model or determine the rate equation. These points are points 1-4 from Table 5,2.

Figure 5.17 - Comparison between actual and calculated data for CO reduction at 827°C (1100 K) and 10 vol% CO

Figure 5.18 - Comparison between actual and calculated data for CO reduction at 827°C (1100 K) and 30 vol% CO

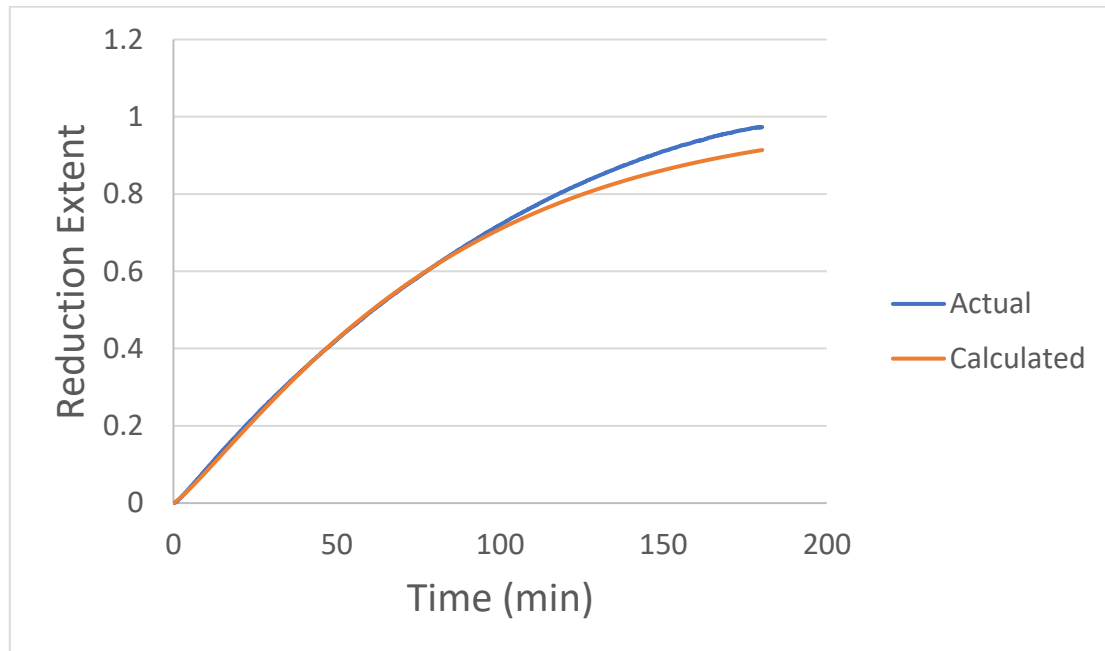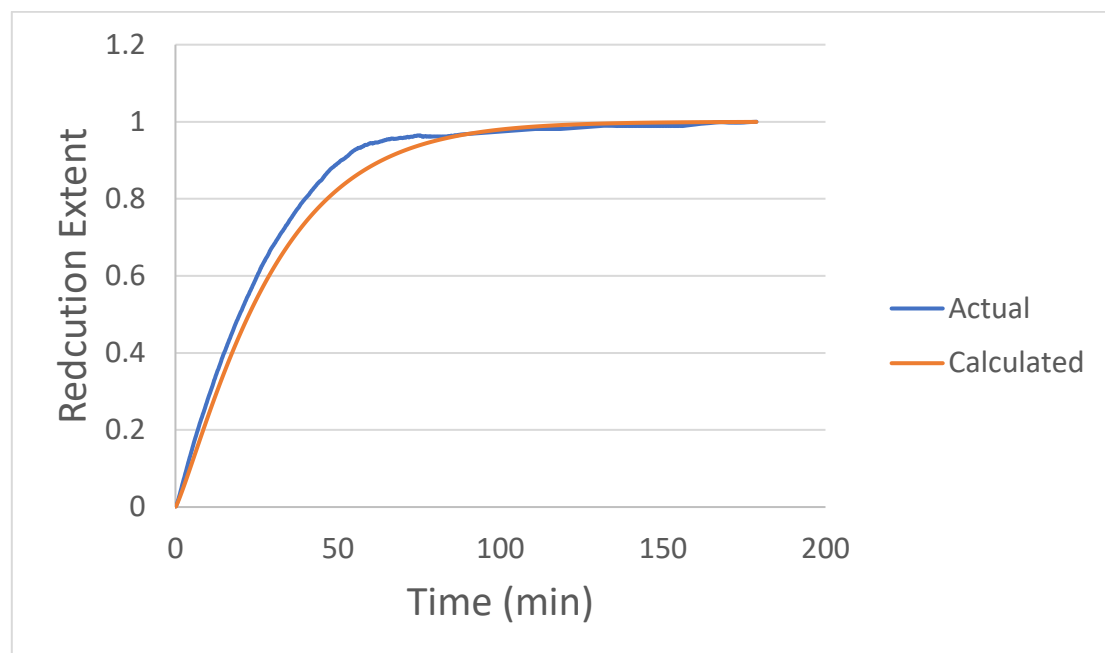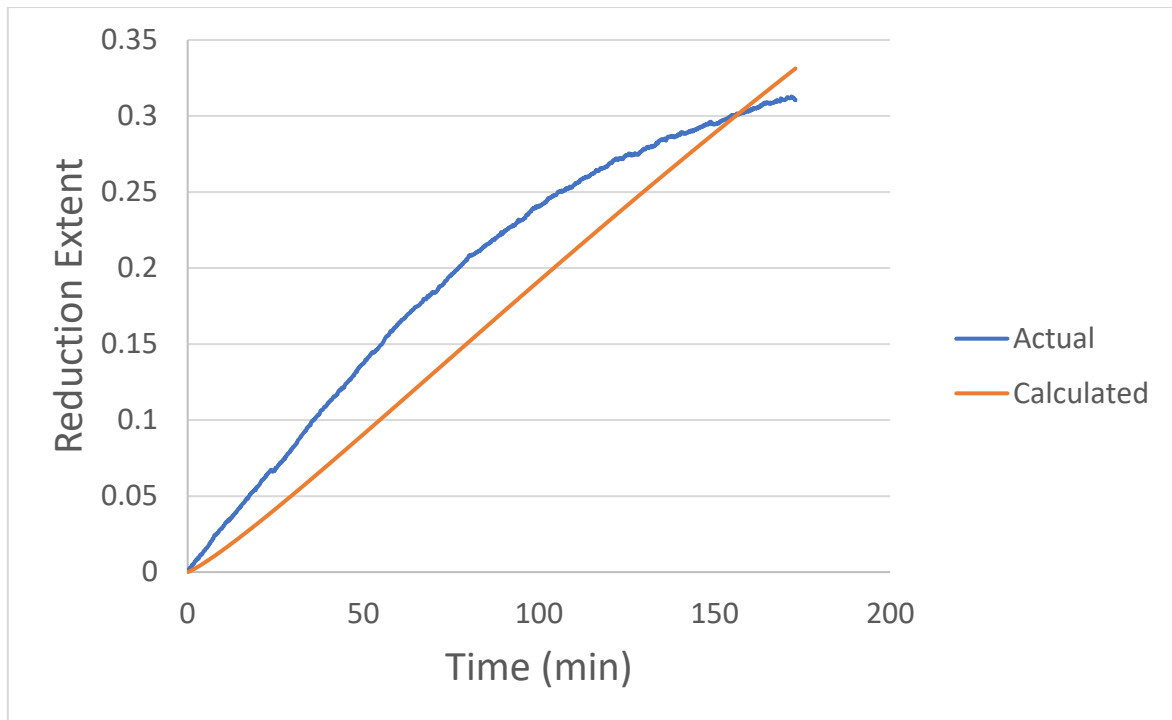*Figure 5.19 - Comparison between actual and calculated data for CO reduction at 627°C (900 K) and 10 vol% CO*
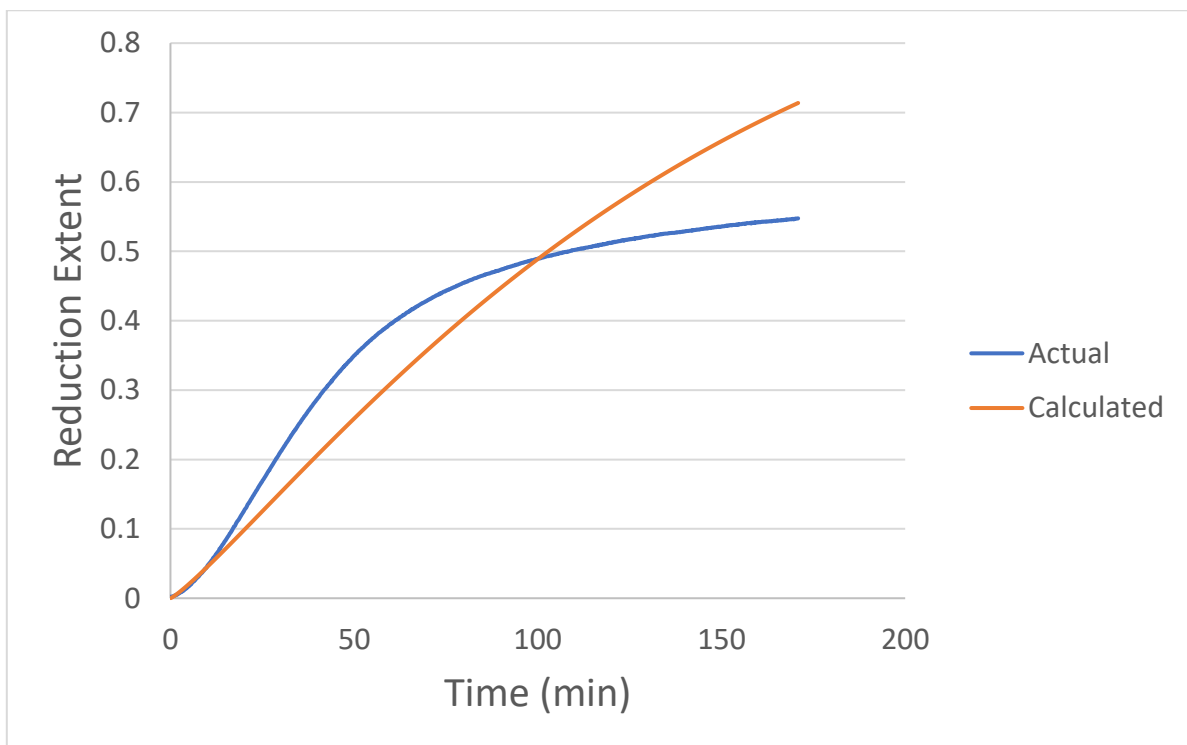

Figure 5.20 - Comparison between actual and calculated data for CO reduction at 627°C (900 K) and 30 vol% CO

From the figures above it can be seen that at higher temperatures, the calculated data show good agreement with the actual data. However, at low temperatures, there exists

a discrepancy between the two respective sets of data for each set of conditions. The initial underestimation by the model is likely due to the Avrami equation itself - data that is input into this equation is evaluated in a logarithmic form. This causes the initial values to be weighted less.

As observed in Figure 5.20, the actual reduction extent at 900K seems to be reaching a peak at about 0,6. An explanation for this can be found in Figure 4.21 – in the reduction progress tests. In this figure, it depicts that braunite I and braunite II, which make up large parts of the ore, do not reduce well under these low temperatures. This is likely the cause of the reduction extent peaking at such low values for the lower temperatures and the cause of the calculated reduction extent overestimating actual data under these conditions.

5.3 H_2/H_2O kinetic study

In efforts to align this work with current environmentally friendly trends, hydrogen was also considered as a reductant. A kinetic evaluation, similar to that carried out with CO as reductant, was done for hydrogen reduction. The conditions considered (temperature and reductant ratio) were the same used for the CO kinetic study – this allowed for a direct comparison in reduction kinetics between the two different reductants.

Central composite design using H_2 as reductant

The temperatures and H_2/H_2O ratios used for the hydrogen reduction tests were obtained from the respective Mn and Fe Chaudron diagrams. For illustrative purposes, the Chaudron diagram with the central composite experimental design is shown in Figure 5.21.
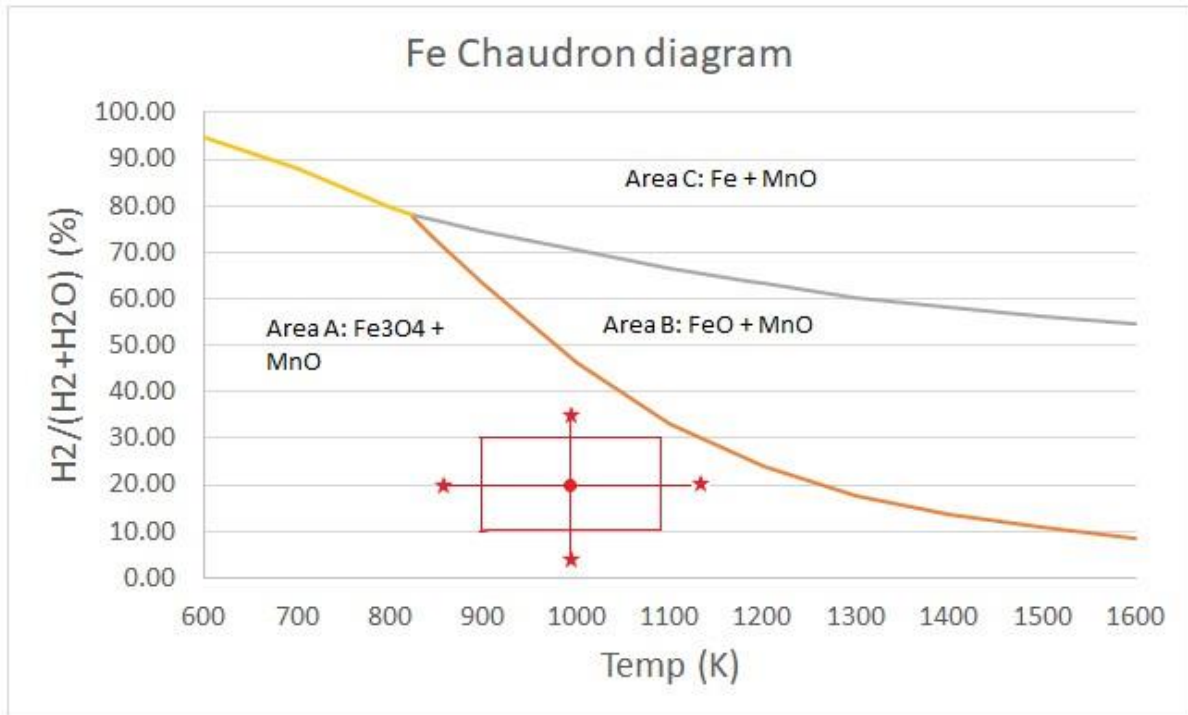
Figure 5.21 - Iron Chaudron diagram, for H_2 reduction, depicting the central composite experimental design

The factorial design is a 2^2 design – similar to the CO study. There are therefore, again, 4 factorial points, 4 star/axial points (2k) and n_c centre points. The 2 factors are temperature and H_2/H_2O ratio, each with a higher and a lower level (+1, -1). The relationship between the coded variables (x_1, x_2) and the natural variables (Temperature and H_2/H_2O) ratio are as follows:

$$x_1 \ (Temperature) = \frac{Temp-1000}{100} \qquad 5.9$$

$$x_2 \left(\frac{H_2}{H_2O}\right) = \frac{\frac{H_2}{H_2O}-20}{10} \qquad 5.10$$

The relationships described above can be used to formulate the different levels for each natural variable. These levels are depicted in Table 5.7.

Table 5.7 - Values of natural variables for different levels of coded variables for H_2 reduction tests

Parameter	Code	Higher level (+1)	Lower Level (-1)	Central point (0)	Higher axial point (+1.414)	Lower axial point (-1.414)
Temperature(K)	X_1	1100K	900K	1000K	1141.4K	858.6K
H_2/H_2O ratio	X_2	30%	10%	20%	34.14%	5.86%

The complete experimental design for the H_2/H_2O test is depicted in Figure 5.22.
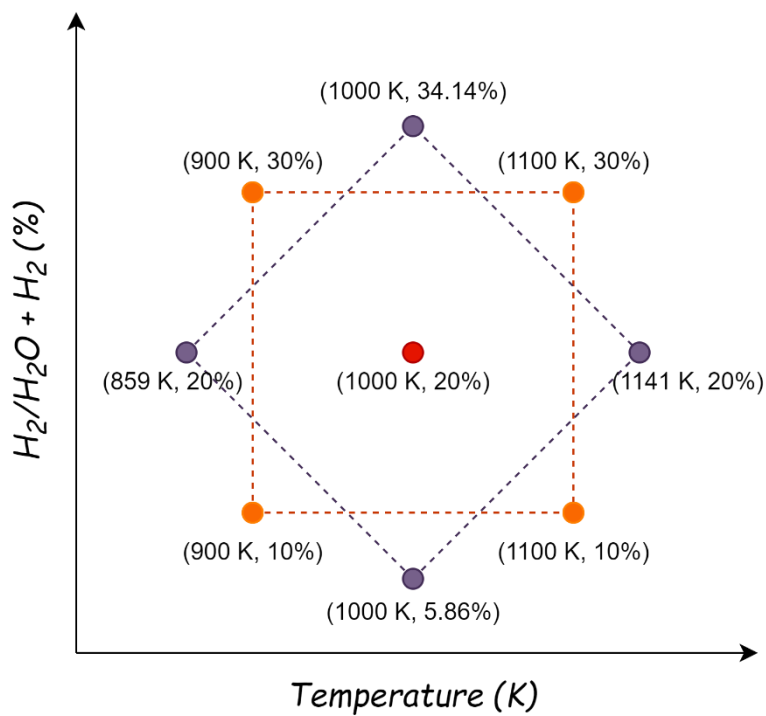

Figure 5.22 - Depiction of the experimental design for the H_2/H_2O test (including values of the natural variables)

The experimental runs are shown in Table 5.8 below.

Table 5.8 - Central composite design for H_2/H_2O tests

Std. order	X_1	X_2	T (K)	Reductant (H_2/H_2O)
1	-1	-1	900	10
2	1	-1	1100	10
3	-1	1	900	30
4	1	1	1100	30
5	-1.41421	0	858.58	20
6	1.414214	0	1141.42	20
7	0	-1.41421	1000	5.86
8	0	1.414214	1000	34.14
9	0	0	1000	20
10	0	0	1000	20

Experimental setup

The same procedure and experimental setup that was used for the CO kinetic study was used for the H_2 kinetic study. The only change that was made to the setup was that a bubbler was added to introduce H_2O into the gas stream. The carrier gas used was N_2. In order to achieve the desired H_2/H_2O ratios, the bubbler was run at a constant temperature and with a constant N_2 carrier gas flow (1,5 Nl/min) and the gas flow of H_2 was varied using a mass flow controller. In order to prevent condensation of water vapour at the gas inlet in the furnace, a copper coil was installed from the furnace gas inlet to an area closer to the hot zone of the furnace.

5.3.1 Results and discussion

The raw data of each test run, specified by the central composite design, is shown in Figure 5.23.
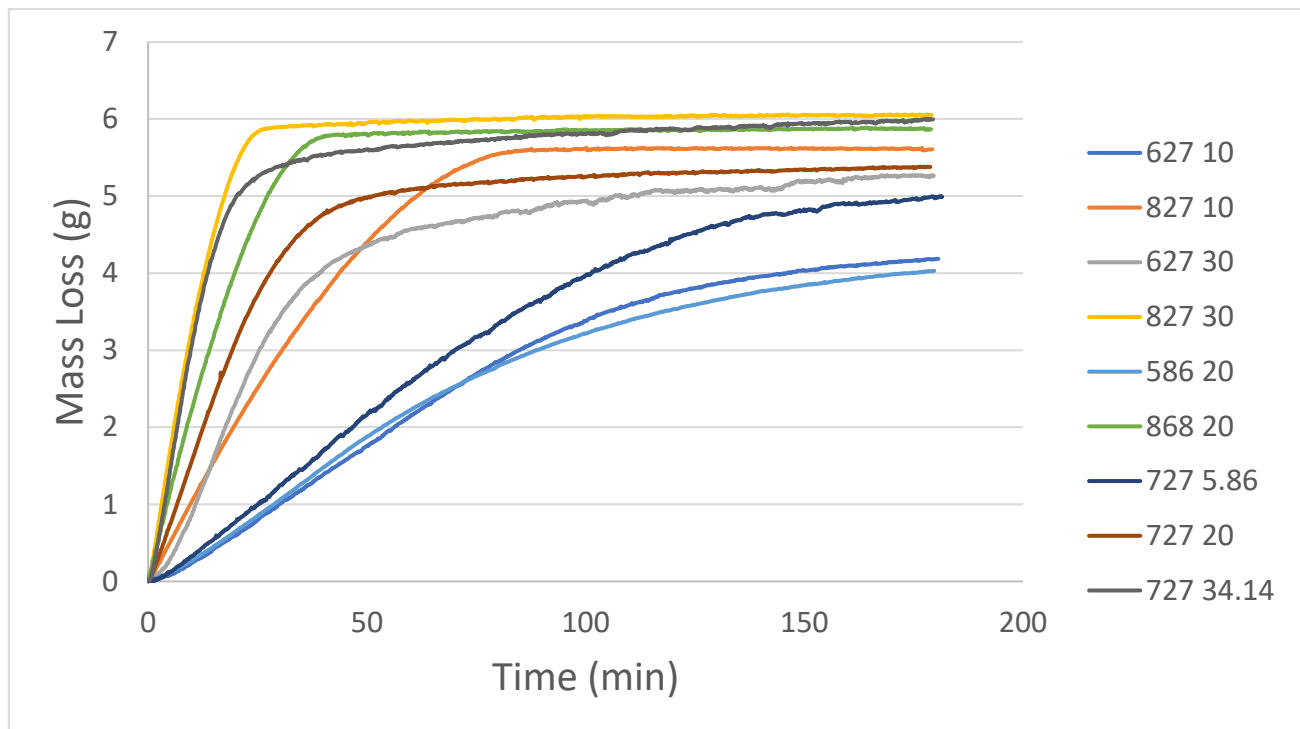
Figure 5.23 - Raw data for H_2 kinetic study in the form of mass loss vs time curves. (Key: Temp (°C), vol% H_2)

Reproducibility of experiments

The reproducibility of the kinetic experiments was tested by employing the conditions represented by the centre point of the central composite design, i.e., a temperature of 1000 K and a H_2 content of 20%. Figure 5.24 indicates that there is little significant difference between original and repeat test in terms of reduction extent.
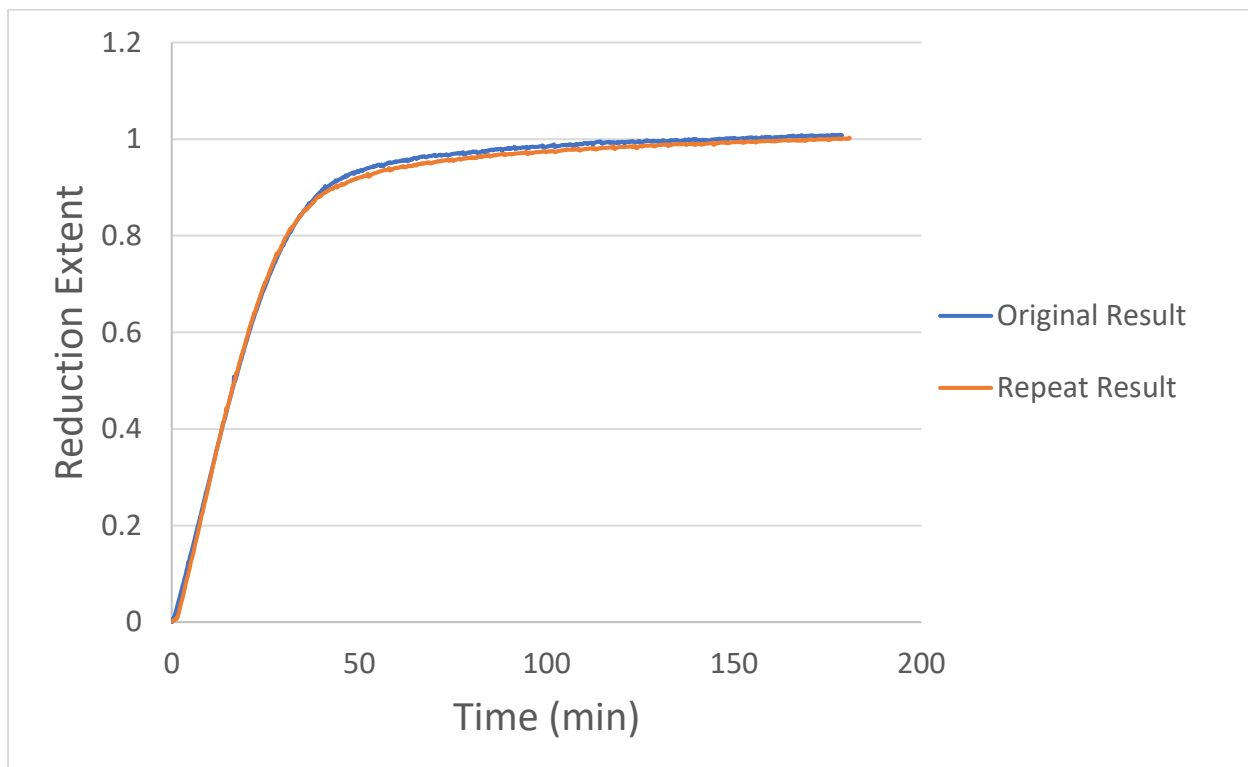
Figure 5.24 - Reduction extent of original and repeat results for H_2 reduction

Effect of temperature

The effect of temperature on the reduction process was studied by considering tests 5, 6 and 9 (listed in Table 5.8). These tests were carried out at the following temperatures: 858K, 1141K and 1000K (586°C, 868°C and 1000°C) respectively. The reducing gas for each of these 3 tests was a mixture of H_2 and H_2O with a volume ratio of $H_2/H_2O = 20/80$.

The reduction extent vs. time curves are depicted in Figure 5.25. From these curves it is evident that an increase in temperature leads to an increase in the reduction rate.
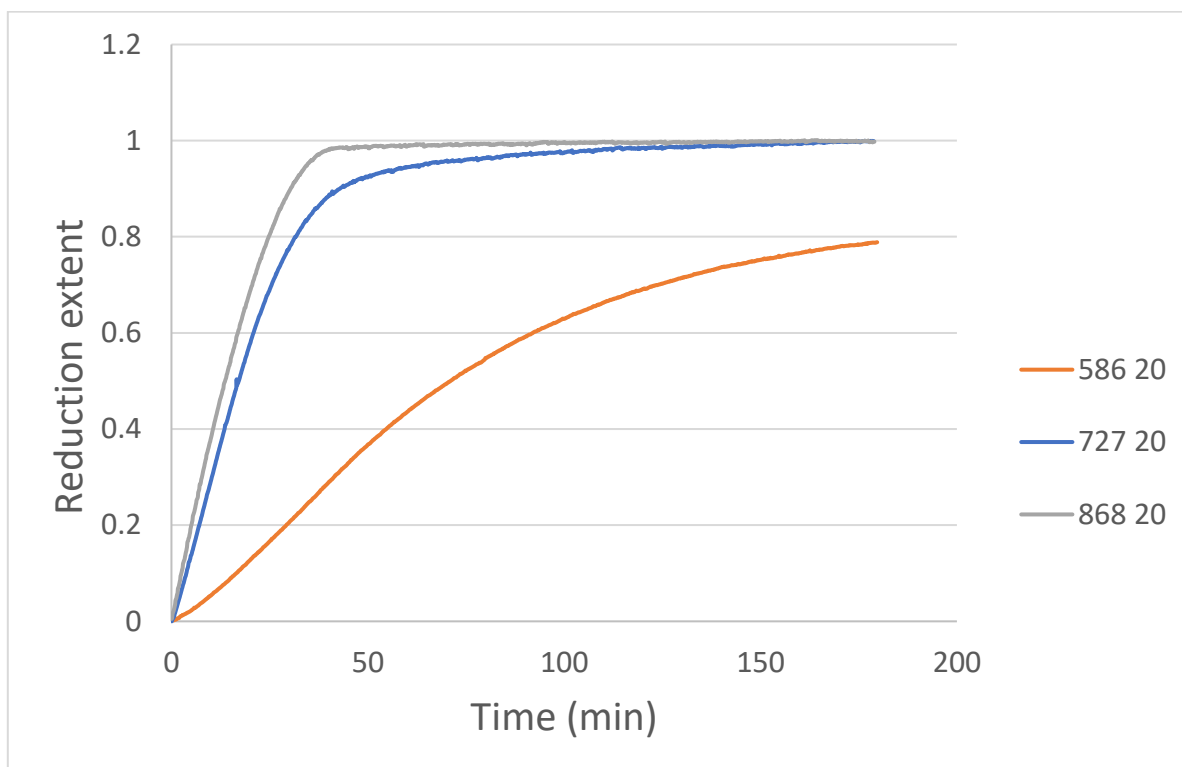
Figure 5.25 - Reduction extent vs time curves for tests at different temperatures. $H_2 = 20$ vol%. (Key - Temp(°C), vol% H2)

From Figure 5.25, it can be determined that temperature does have a significant effect on reaction rate. It can be seen that the reaction reaches completion in ±40 minutes at 868°C, while it takes ±140 minutes to reach completion at 727°C and at 586°C, the reaction is not completed within the 3-hour experimental time.

Effect of H_2 content

The effect of H_2 content on the reduction process was observed by considering tests 7, 8 and 9; listed in Table 5.8. These isothermal tests were carried out at 1000K (727°C), under different H_2/H_2O volume ratios – 5,86 vol% H_2, 20 vol% H_2 and 34,14 vol% H_2.

The reduction extent vs time curves are depicted in Figure 5.26.
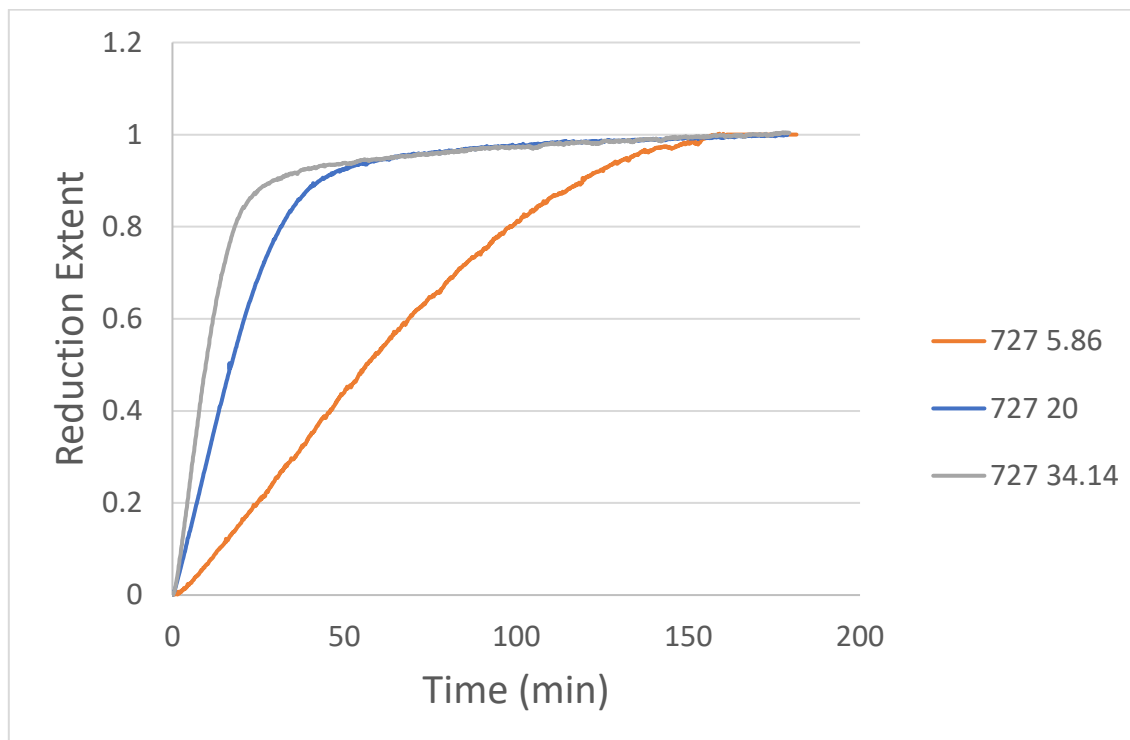
Figure 5.26 - Reduction extent vs time for isothermal tests at different H_2 contents. Temperature = 727°C. (Key - Temp(°C), vol% H_2)

Figure 5.26 gives the first indication that the P_{H2} may not have a significant effect on the overall reduction extent – particularly when compared to the large dependence of P_{CO} for CO reduction. While it is observed that as the concentration of H_2 increases, the reduction extent also increases, at higher concentrations of H_2, this increase becomes small. At lower concentrations of H_2, the supply of reactant is likely rate controlling, resulting in the significantly slower reduction extent, however as the concentration of H_2 increases, the supply of reactant no longer significantly affects the initial reduction extent. Figure 5.26 indicates that at 34,14 vol% H_2, the initial reaction rate is higher than at 20 vol% H_2, however above a reduction extent of about 0,85, the rates become similar up to reaction completion.

5.3.2 Kinetic analysis

The kinetic analysis carried out for H_2 reduction is identical to the analysis carried out for CO reduction, described in Section 5.2.2. For convenience, the rate controlling mechanisms and the integral form of their equations are repeated in Table 5.9.

Table 5.9 - Rate equations for different rate controlling mechanisms

Rate controlling mechanism	Integral form $g(X) = kt$
Chemical reaction control	$1 - (1 - X)^{1/3}$
Diffusion control – Jander model	$(1 - (1 - X)^{1/3})^2$
Nucleation and growth – Avrami model	$(-\ln(1 - X))^{1/n}$

In order to determine which of the rate equations best fit the experimental data, 2 methods were applied:

Firstly, the rate models were linearized and plotted against time or $\ln(t)$ depending on the model. If the model fit the data, this linearization would result in a linear plot. If the reduction was controlled by chemical reaction, a plot of $[1 - (1 - X)^{1/3}]$ vs time would result in straight lines, if the reaction was controlled by diffusion, a plot of $[(1 - (1 - X)^{1/3})^2]$ vs time would be linear and if the reaction was controlled by nucleation and growth, a plot of $[\ln(-\ln(1-X))]$ vs $\ln(t)$ would be a straight line. The plots of these linearisation's are depicted in Figures 5.27, 5.28 and 5.29. For H_2 reduction, most of the experimental runs reached a reduction extent of 100%. Due to uncertainties in the terminative part of the reduction reaction, the linearization plots were only plotted up until a reduction extent of 0,95.
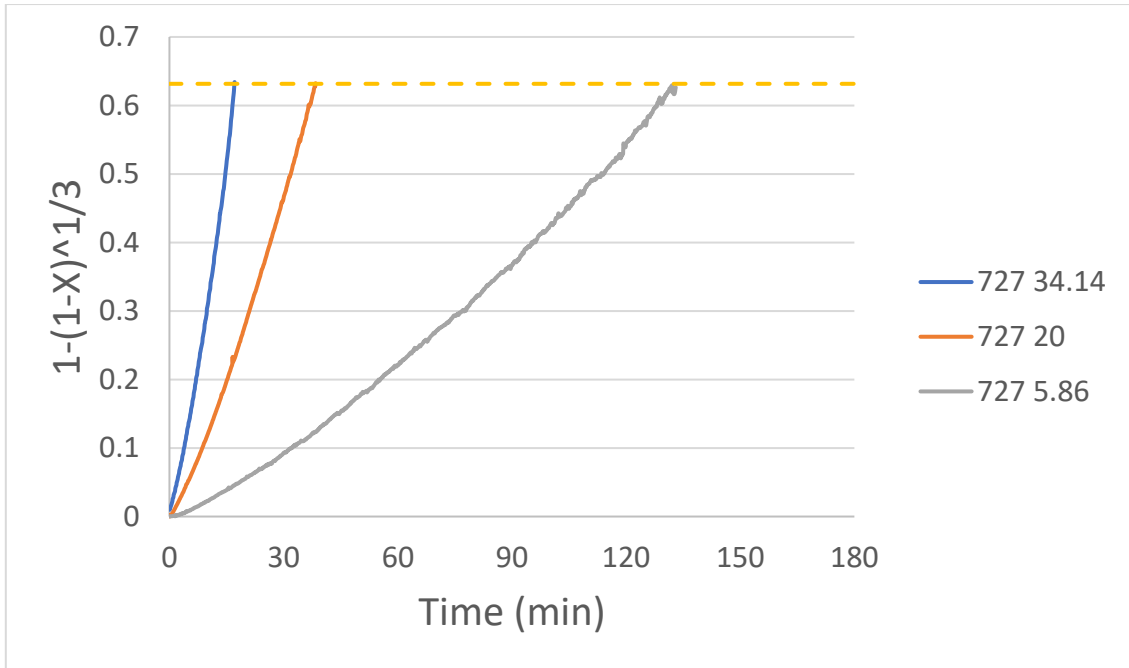
Figure 5.27 - Plots of 1-(1-X)1/3 vs time to determine suitability of chemical reaction control model to fit experimental data (key – Temp(°C), vol% H₂)
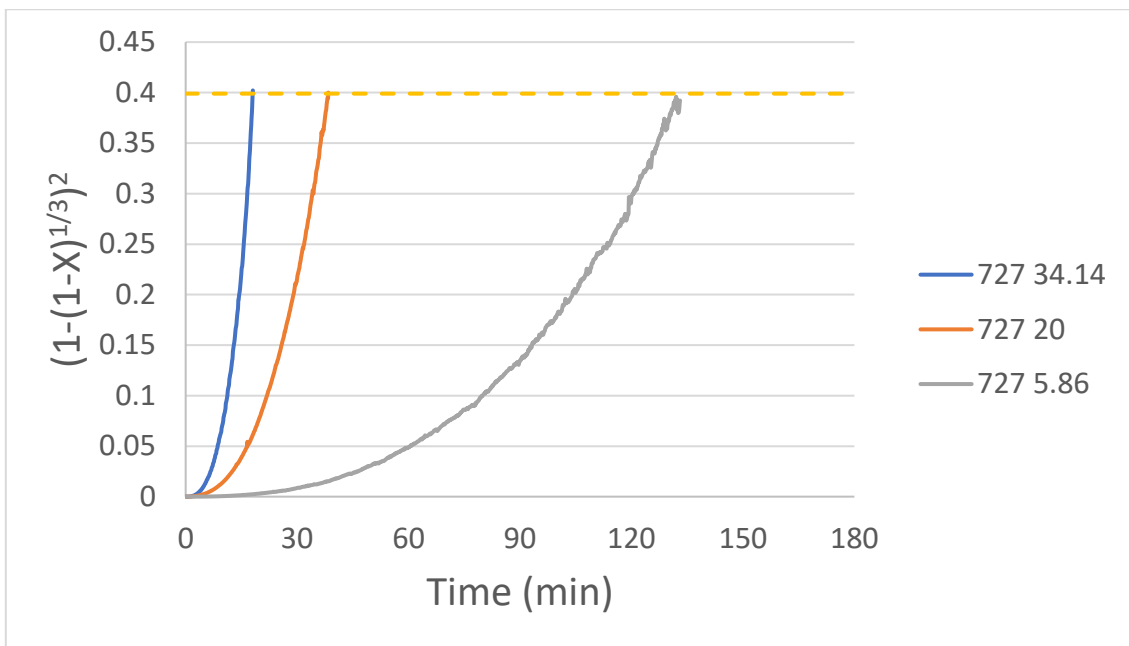
Figure 5.28 - Plots of (1-(1-X)1/3)2 vs time to determine the suitability of the Jander model to fit experimental data (key – Temp(°C), vol% H₂)
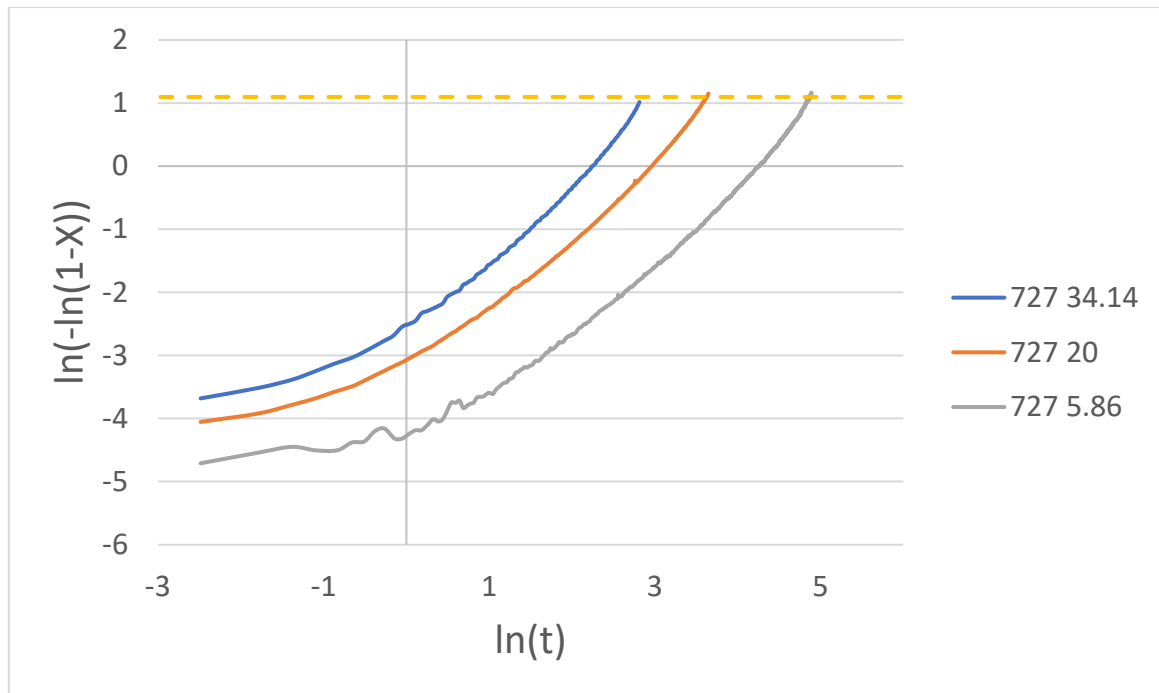
Figure 5.29 - Plots of ln(-ln(1-X)) vs ln(t) to determine the suitability of the Avrami model to fit experimental data (key - Temp(°C), vol% H_2)

From Figures 5.27, 5.28 and 5.29, it is evident that the reduction reaction with H_2 is likely controlled by chemical reaction control, as the linearization of this model is the only one that resulted in a straight line. In order to confirm this, a second method was applied to fit the 3 models described above. This second method involved a minimization of the Sum Squared Error (SSE) using Excel. The data used to fit the models is from the centre point of the central composite design – 727°C and 20 vol% H_2.

The plots of the experimental data vs time and calculated data vs time are depicted below:
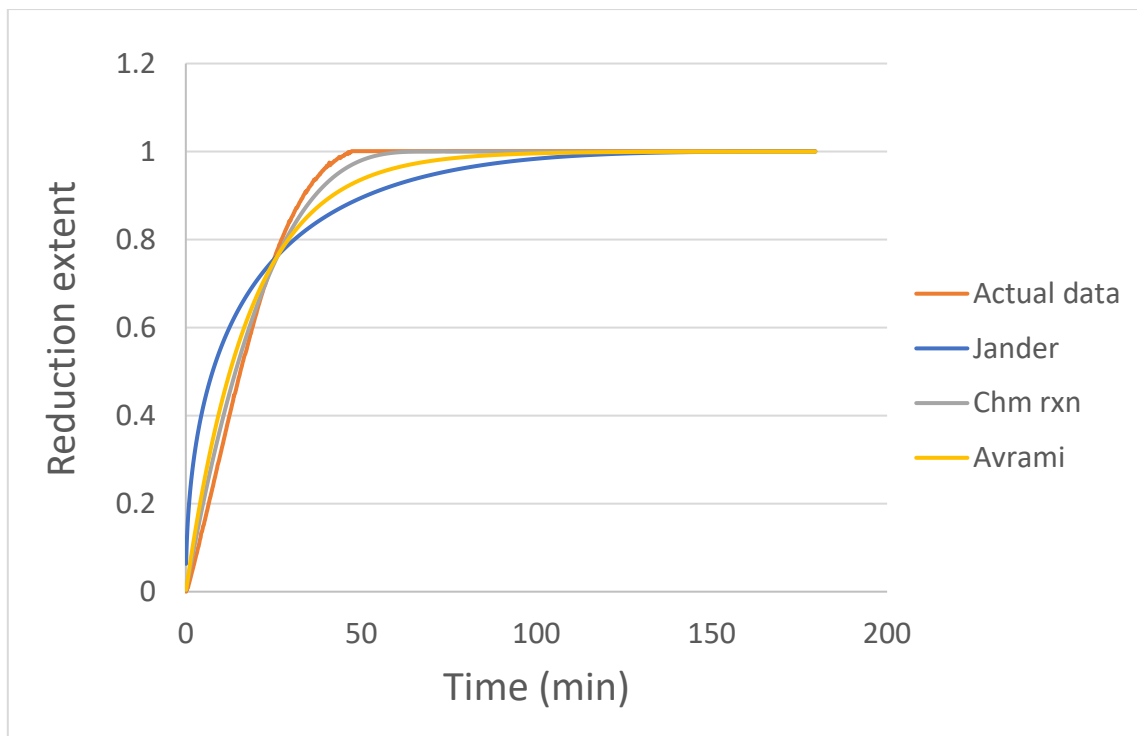
Figure 5.30 - Best fit of the 3 models considered compared with actual data

From Figure 5.32, it is likely that the H_2 reduction is chemical reaction controlled. This is backed up by the plots depicting the effect of temperature and the effects of P_{H2} which indicated that the P_{H2} did not have a very significant effect on the reaction rate at higher P_{H2}'s, but that temperature did have a significant effect. The chemical reaction rate controlling mechanism for H_2 also makes sense due to the small size of the H_2 molecule allowing for very rapid diffusion to occur, either through the pores of the briquettes or through any formed product layers. If the mass transfer rate is controlled by the diffusion of product species away from the reaction site, then it can be concluded that the diffusion rate of H_2O is faster than that of CO_2.

To further confirm these observed trends, plots of "Percent error vs time" (Figure 5.31) and "Experimental values vs Calculated values" (Figure 5.32) were also plotted.

Figure 5.31 – Percent error vs time for the 3 evaluated models (Error = Calculated value - Experimental value) at the centre point of the central composite design (727°C, 20 vol% H_2)

Figure 5.32 - Experimental value vs Calculated value at the centre point of the central composite design (727°C, 20 vol% H_2)
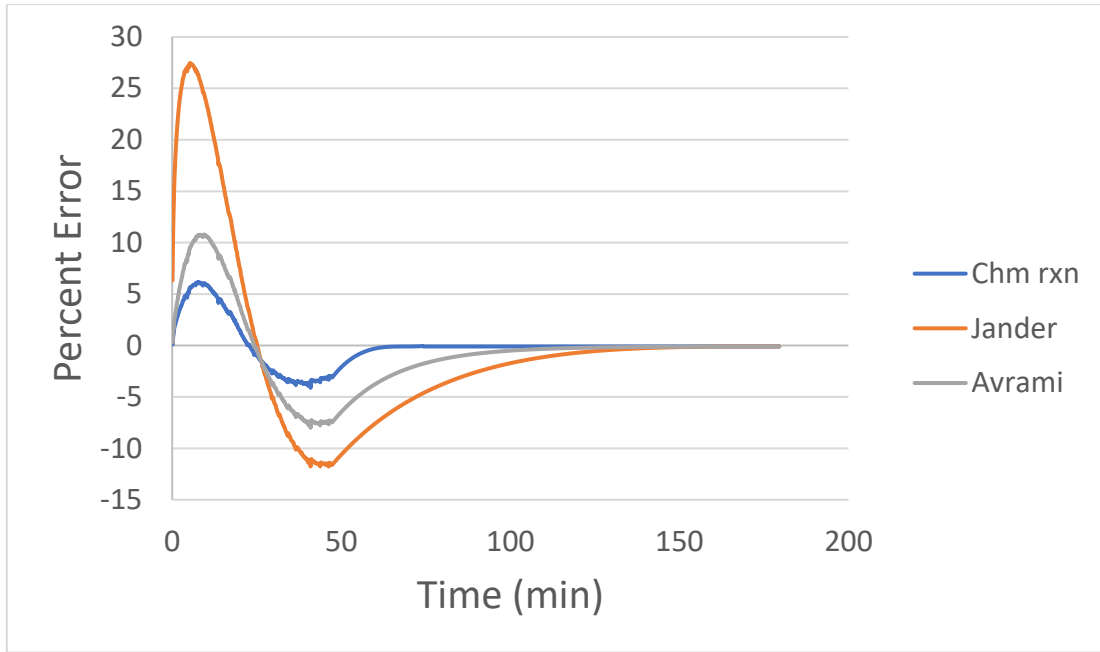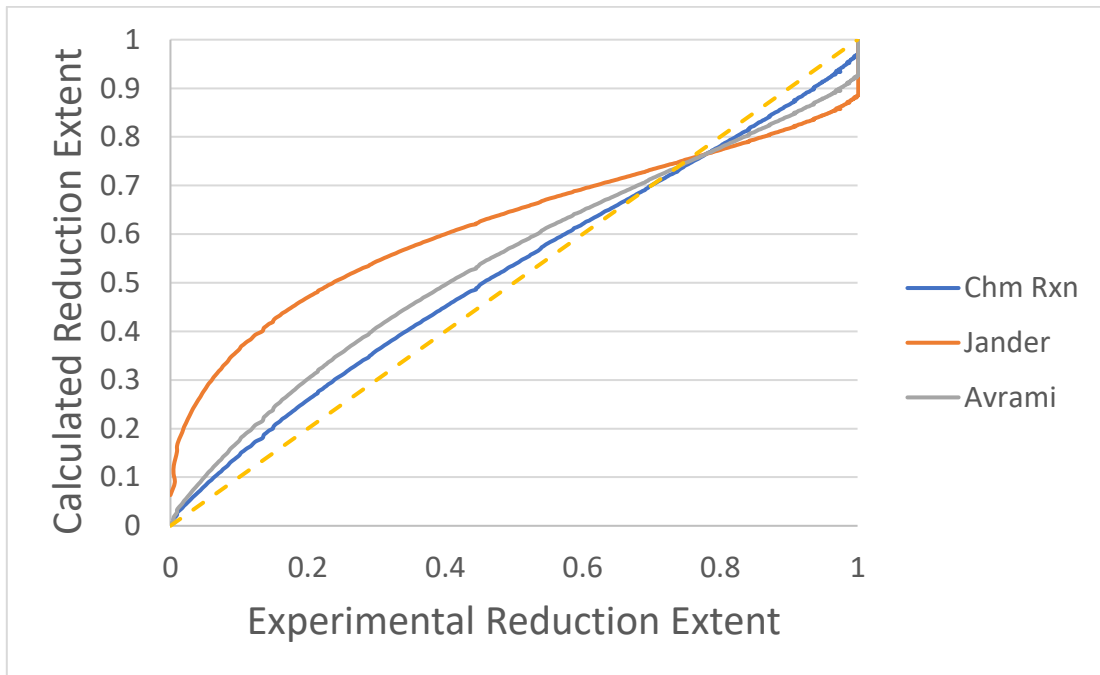
From the 2 model fitting methods described, the best fit for the experimental data was the chemical reaction control model. The next step was to determine the variables associated with this model, which is depicted below:

$$1 - (1 - X)^{\frac{1}{3}} = k_{app}t \qquad\qquad 5.11$$

Where:

- X – Reduction extent
- k_{app} – apparent rate constant
- t – time

The apparent rate constant, k_{app}, takes into consideration the effects of the partial pressures of the reducing gas mixture, according to the following equation:

$$k_{app} = k[p_{H2}^m - (\frac{P_{H_2O}}{K})^m] \qquad\qquad 5.12$$

Where:

- k – effective rate constant
- P_{H2} – H_2 partial pressure
- P_{H2O} – H_2O partial pressure
- m – reaction order
- K – equilibrium constant

It can be assumed that the value of K (equilibrium constant) for this reduction process will be sufficiently large to result in the contribution of the $(\frac{P_{CO_2}}{K})^m$ term being negligible. This then simplifies the expression for k_{app} to the following:

$$k_{app} = k(p_{H2}^m) \qquad\qquad 5.13$$

The calculation for the partial pressures of H_2 and H_2O is carried out with the following equation:

$$P = P_T X \qquad\qquad 5.5$$

Where:

- P – partial pressure of either H_2 or H_2O
- P_T – total pressure. In this case the P_t is taken to be 0,86 atm, which is the atmospheric pressure in Pretoria, South Africa.
- X – volume fraction of either H_2 or H_2O

The first term that was calculated was the exponent "m". In order to determine the value of this, a plot of $\ln(k_{app,H2})$ vs $\ln(P_{H2})$ was made. The value of $\ln(k_{app,H2})$ was determined from the y-intercept of the linearised plots of the chemical reaction model at different concentrations of H_2 (constant temperature). This plot is depicted in Figure 5.27 but is repeated in Figure 5.33 with the addition of the best fit lines.
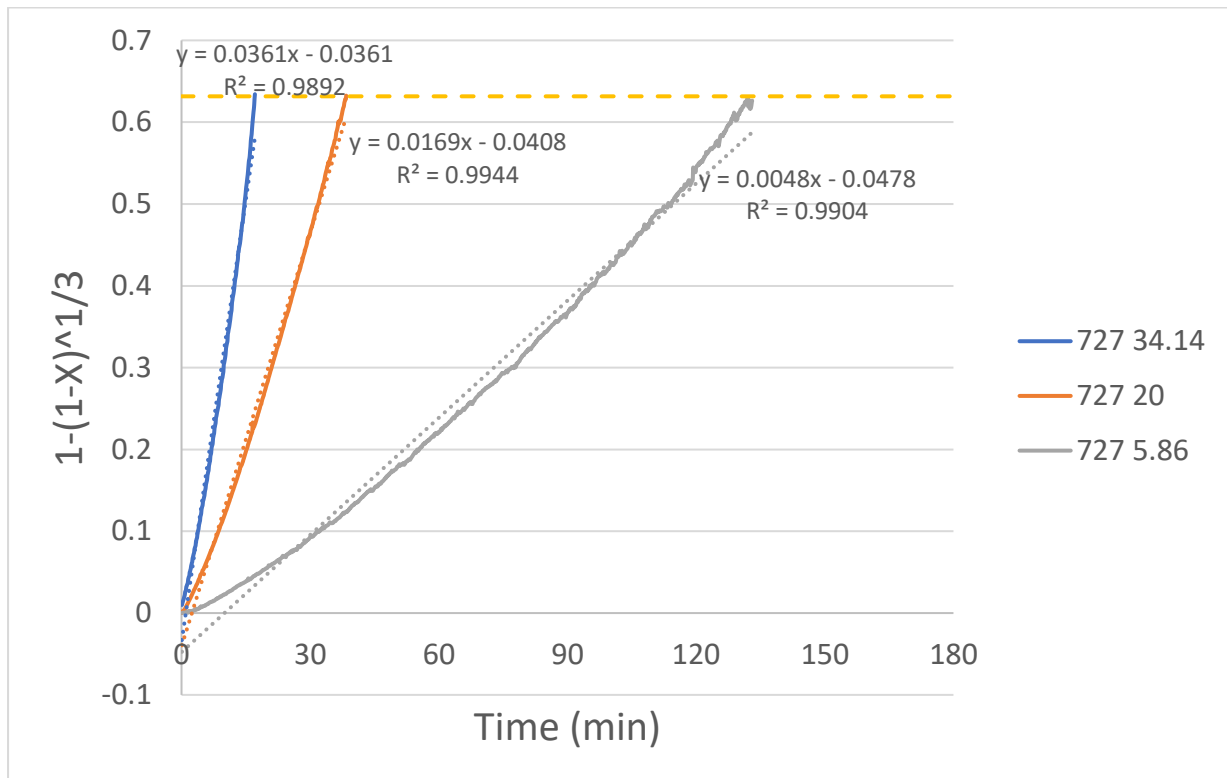
Figure 5.33 - Linearisation plots of chemical reaction control model at different H_2 contents (constant temperature). Y-int used for determination of "m" (key – Temp(°C), vol% H_2)

The values of $\ln(k_{app,H2})$ and those of P_{H2} used for the determination of the exponent "m" are summarised in Table 5.10 below:

Table 5.10 - Values of P_{H2} and $\ln(k_{app,H2})$

Vol% H_2	P_{H2}	$\ln(k_{app,H2})$
5,86	0,05	-0,0478
20	0,172	-0,0408
34,14	0,294	-0,0361

*$k_{app,H2}$ in min^{-1}

The values of $\ln(P_{H2})$ and $\ln(k_{app,H2})$, were then plotted. The results are depicted in Figure 5.34.
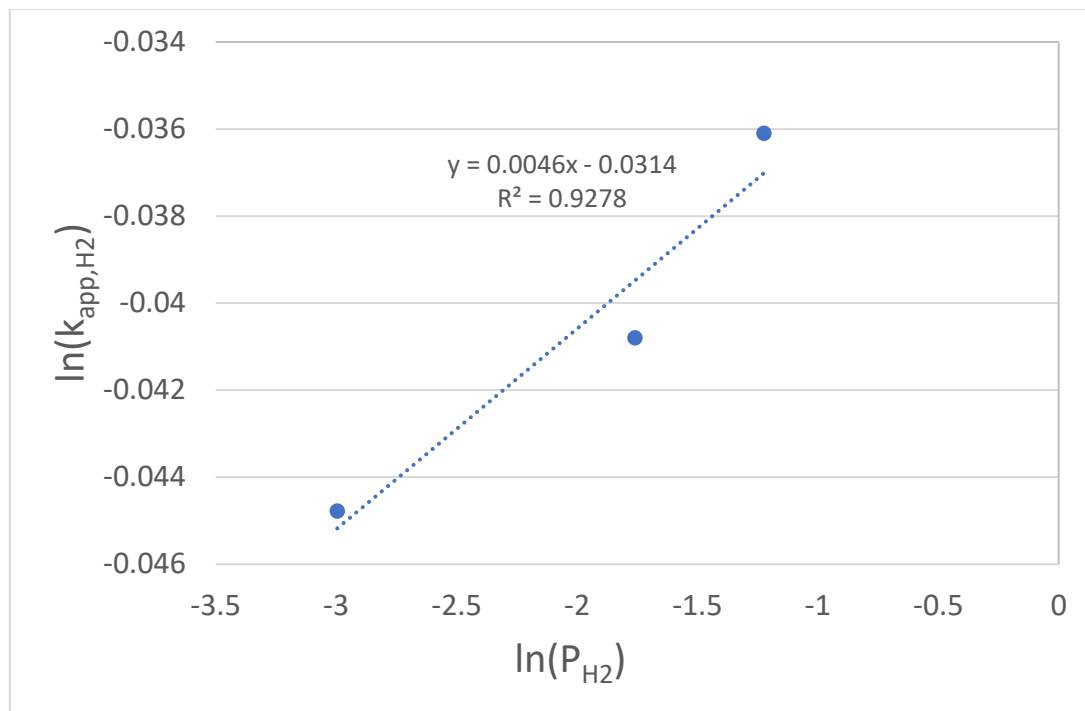
Figure 5.34 - Plot of ln(P_{H2}) vs ln(k_{app,H2}) for the determination of the exponent "m"

Figure 5.34 - Plot of $ln(P_{H2})$ vs $ln(k_{app,H2})$ for the determination of the exponent "m"

The slope of the line of best fit of the plot of $ln(P_{H2})$ vs. $ln(k_{app,H2})$ represents the value of the exponent m. From Figure 5.34, this value is taken as 0,0046.

Placing the value of this exponential term into the chemical reaction control equation yields the following result:

$$1 - (1 - X)^{\frac{1}{3}} = kP_{H_2}^{0.0046}t \qquad\qquad 5.14$$

This leaves the determination of k, the effective rate constant. The value of k follows an Arrhenius relationship according to the following equation:

$$k = k_0 e^{\frac{-E_a}{RT}} \qquad\qquad 5.7$$

Where:

- K_0 – pre-exponential constant (atm^{-1}min^{-1})
- E_a – Activation energy (J/mol)
- R – Gas constant (J/mol.K)
- T – Temperature (K)

In order to determine the value of k_0 and E_a, Excel's Solver function was used to minimise the Sum Squared Error (SSE) of the fit between the calculated and experimental data. This led to the determination of the 3 different values for k, at

different temperatures. A plot of ln(k) vs 1000/T was then made to determine the values of k_0 and E_a.

Table 5.11 - calculated values of the effective rate constant at different temperatures

T(K)	k (atm^{-1}min^{-1})
859	0.00265
1000	0.0132
1141	0.0163
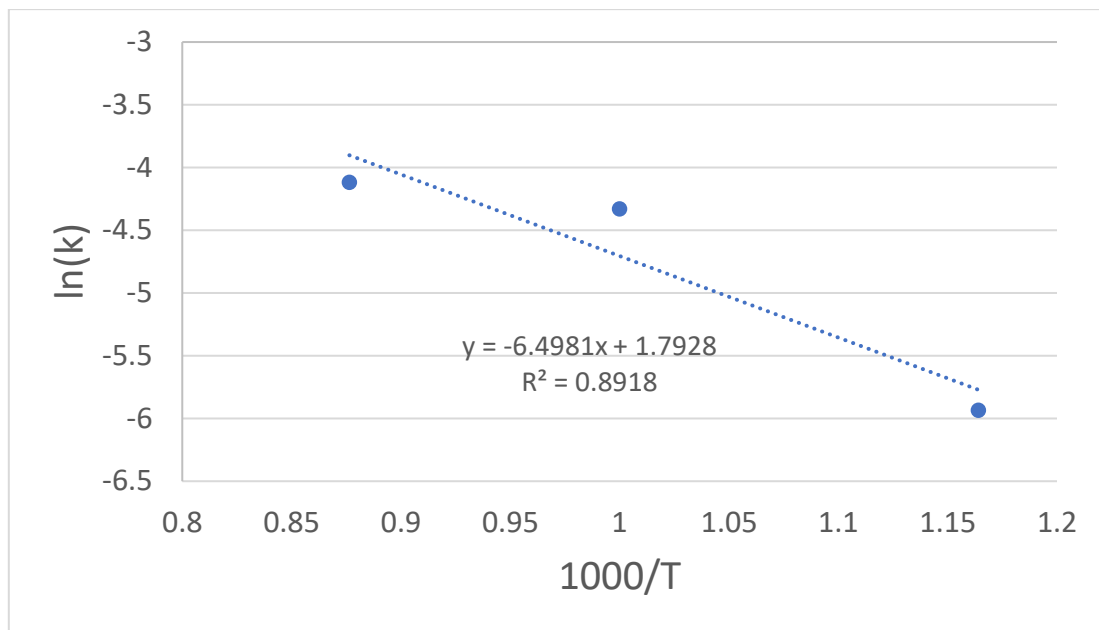
Figure 5.35 - Plot of ln(k) vs 1000/T to determine the values of k_0 and E_a

The value of E_a can be determined from the slope of Figure 5.35, and a value of 54025,2 J/mol is obtained for the activation energy. The value of k_0 is obtained from the y-intercept. The calculated value of k_0 is 6,01 atm^{-1}min^{-1}.

Based on the above kinetic analysis, the overall rate equation for the H_2 reduction process is as follows:

$$1 - (1 - X)^{\frac{1}{3}} = kP_{H_2}^m t \qquad\qquad 5.15$$

With:

$$k = k_0 e^{\frac{-E_a}{RT}} \qquad\qquad 5.7$$

Where:

- k_0 – 6,01 atm^{-1}min^{-1}

- E_a – 54025,2 J/mol
- m – 0,0046

And the units for t and P_{H2} are minutes and atm, respectively.

5.3.3 Evaluation of model

The figures below compare the actual data and calculated data, considering the points of the central composite design that were not used to fit the model or determine the rate equation. These points are points 1-4 from Table 5.8.

Figure 5.36 - Comparison between actual and calculated data for H_2 reduction at 827°C (1100 K) and 30 vol% H_2

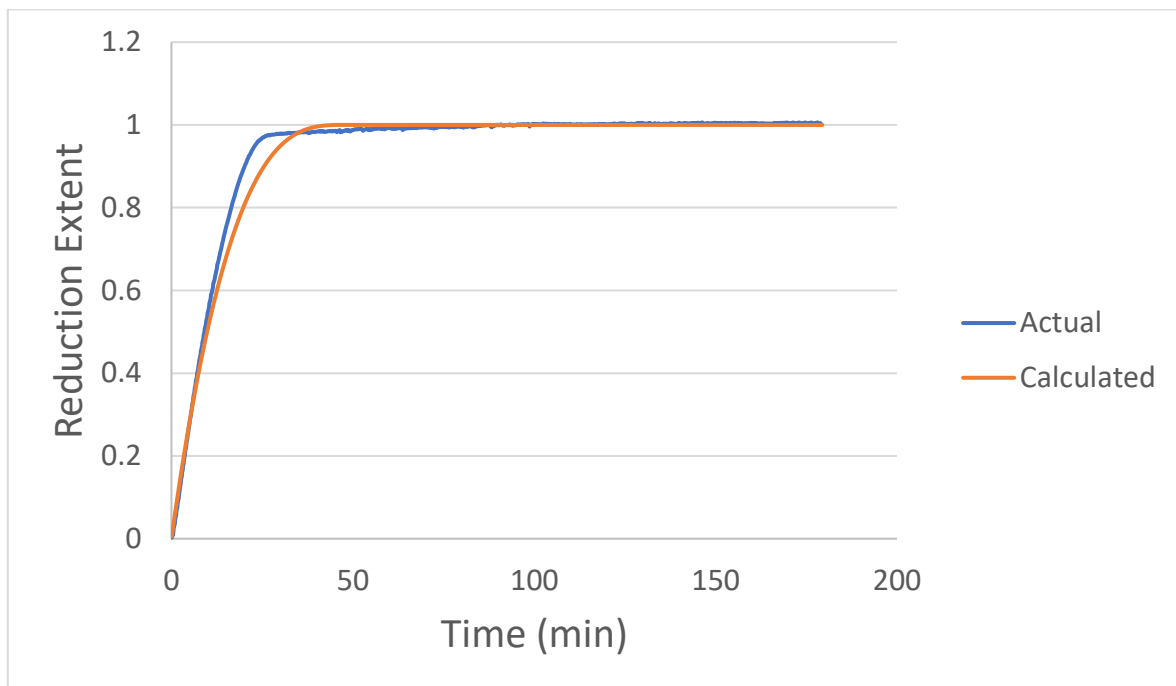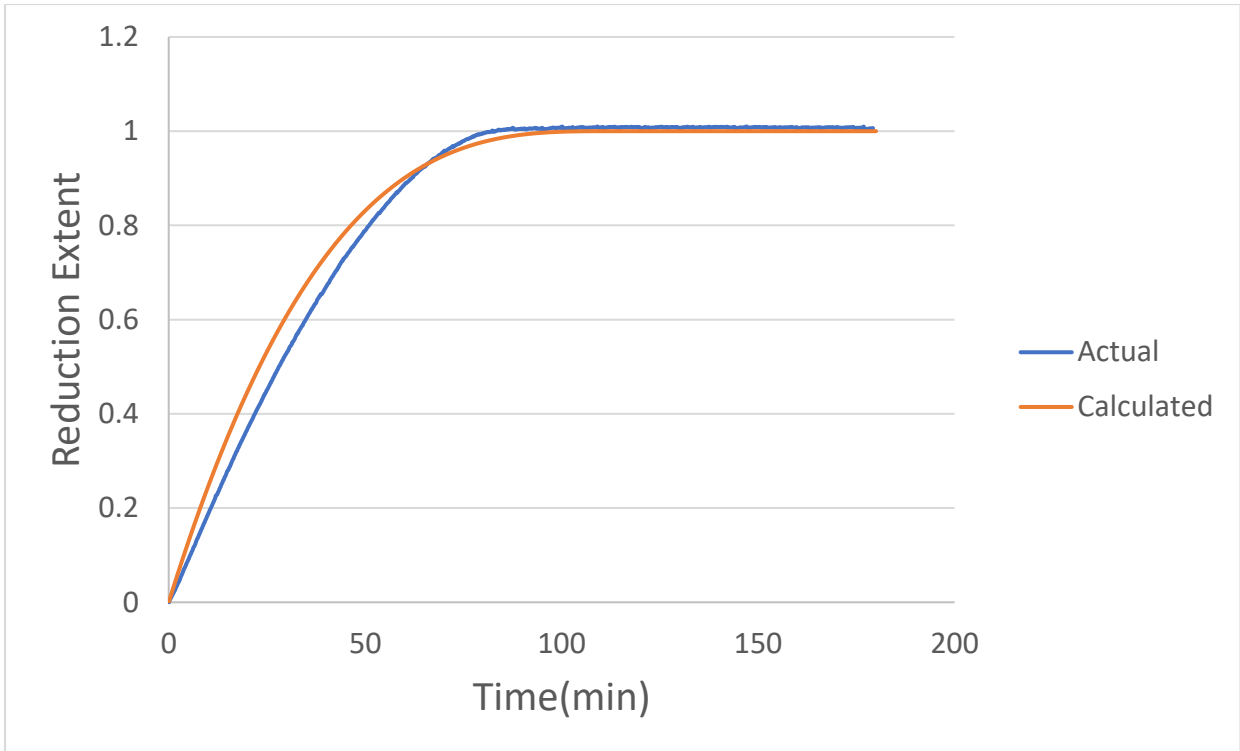*Figure 5.37 - Comparison between actual and calculated data for H2 reduction at 827°C (1100 K) and 10 vol% H_2*
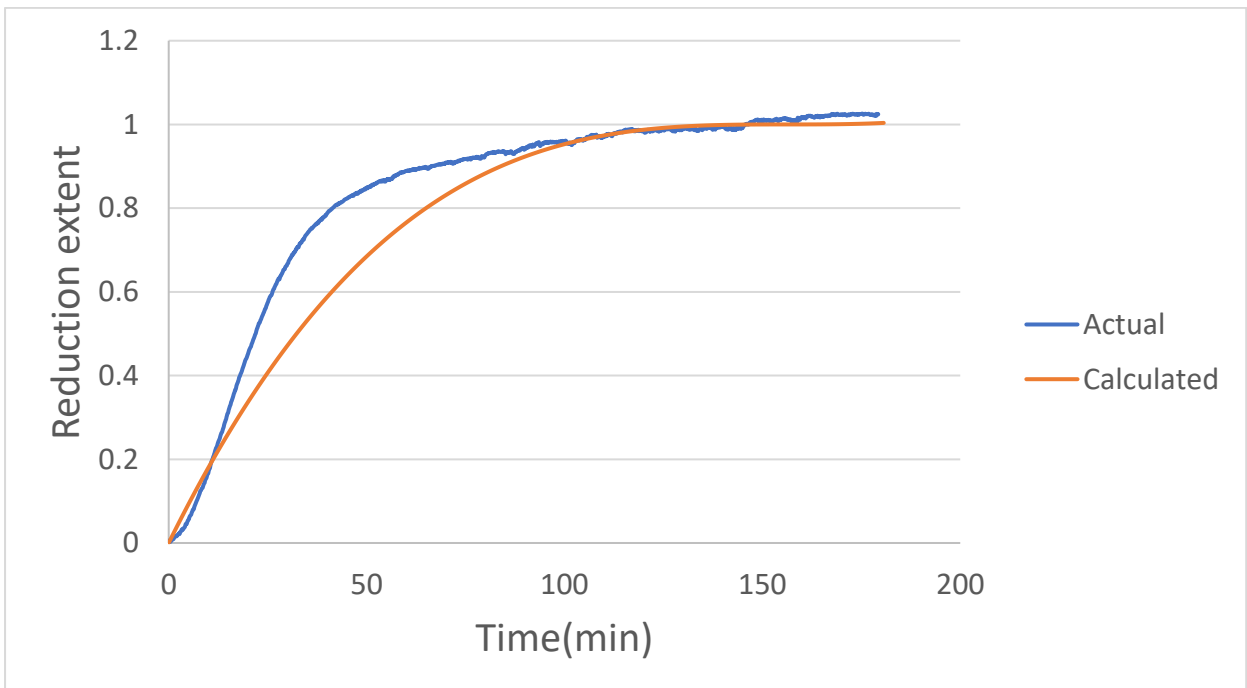

Figure 5.38 - Comparison between actual and calculated data for H2 reduction at 627°C (900 K) and 30 vol% H_2
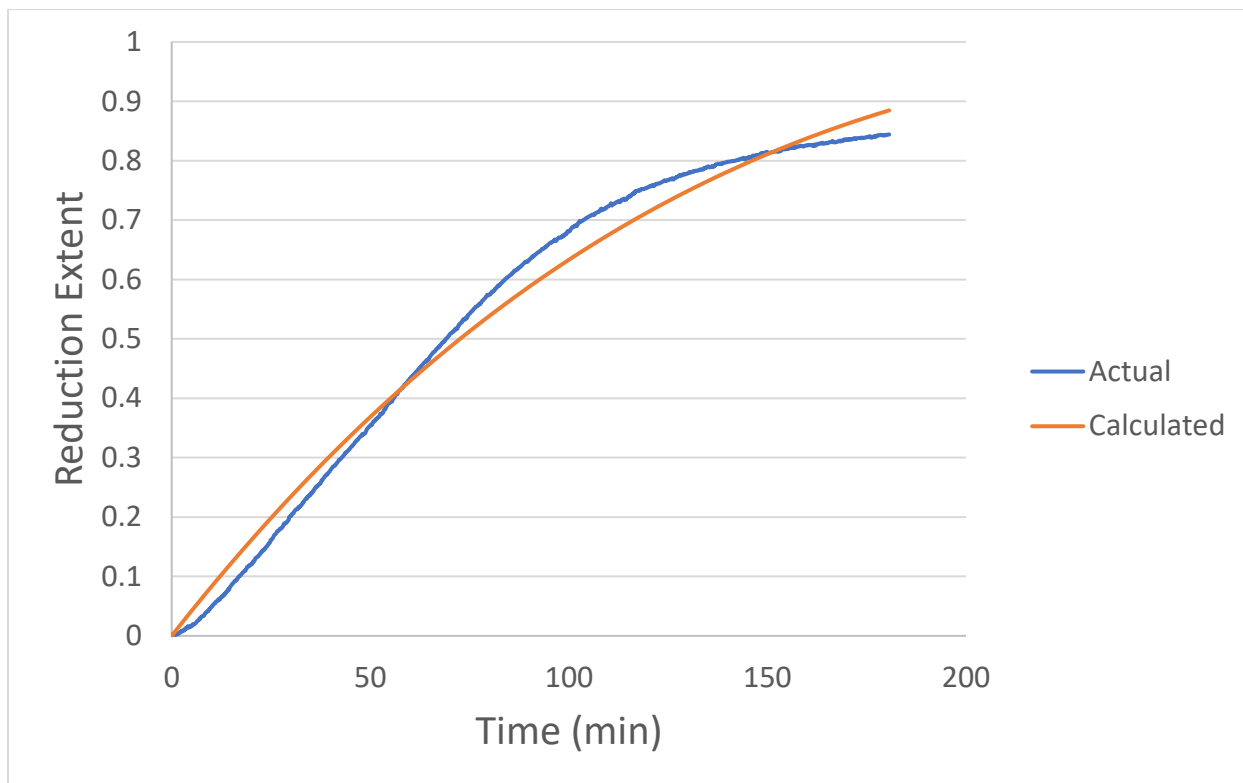
Figure 5.39 - Comparison between actual and calculated data for H2 reduction at 627°C (900 K) and 10 vol% H_2

From the Figures above it can be seen that the model seems to show good agreement with experimental data at the different sets of conditions, with a better fit at higher temperatures.

5.4 Comparison between CO and H_2 reduction kinetics

As interest grows in the use of green, environmentally friendly reductants, comparing key aspects such as reduction kinetics between these new green reductants and currently used reductants, such as CO is of vital importance. As industry begins to make the switch to alternate reductants, it is vital that the efficiencies of various processes are not affected negatively.

From the plots comparing CO and H_2 reduction below (Figures 5.44 – 5.48), it can be seen that for H_2 reduction, the reduction kinetics are significantly faster. It can also be seen that the reduction reaction reached completion more often with H_2 than with CO. This indicates that the use of H_2 is not only environmentally advantageous (depending on the production method of H_2) but is also advantageous in terms of throughput (faster kinetics) and energy requirements for the process (the reduction reached completion at lower temperature with H_2 than with CO within the experimental time).

Figure 5.40 - Comparison of H₂ and CO reduction at 727°C (1000 K) and 5,86 vol% reductant

Figure 5.41 - Comparison of H2 and CO reduction at 727°C (1000K) and 20 vol% reductant

Figure 5.42 - Comparison of H2 and CO reduction at 727°C (1000 K) and 34,14 vol% reductant
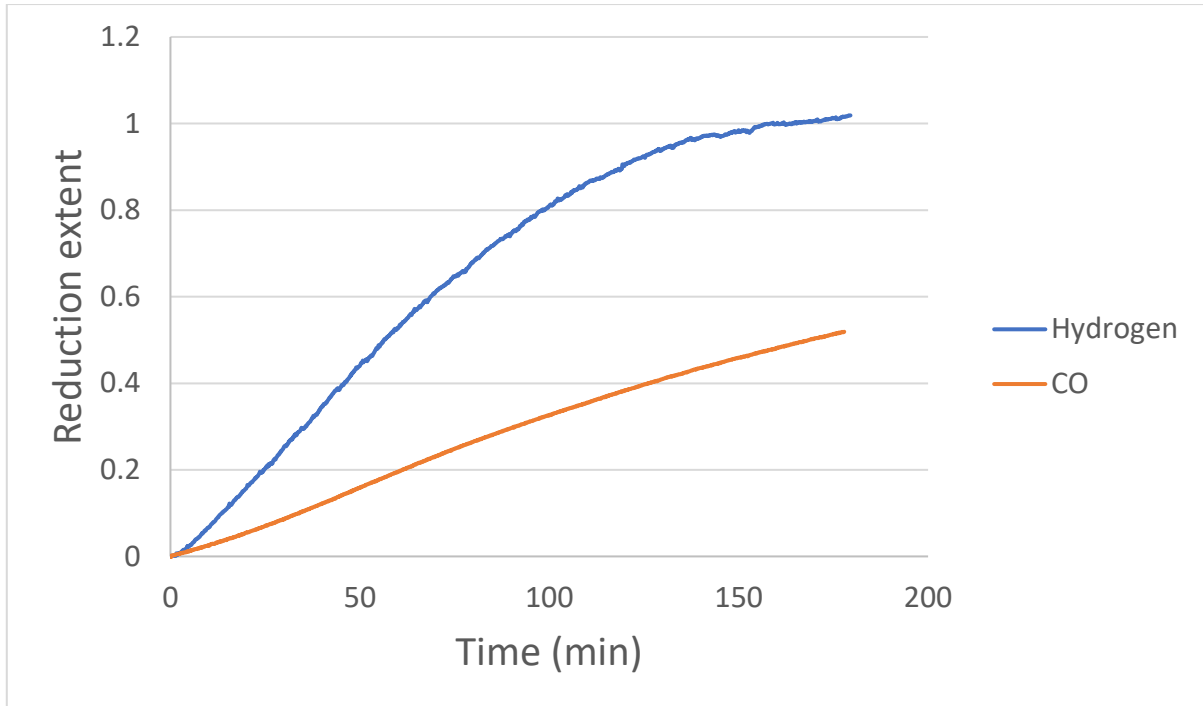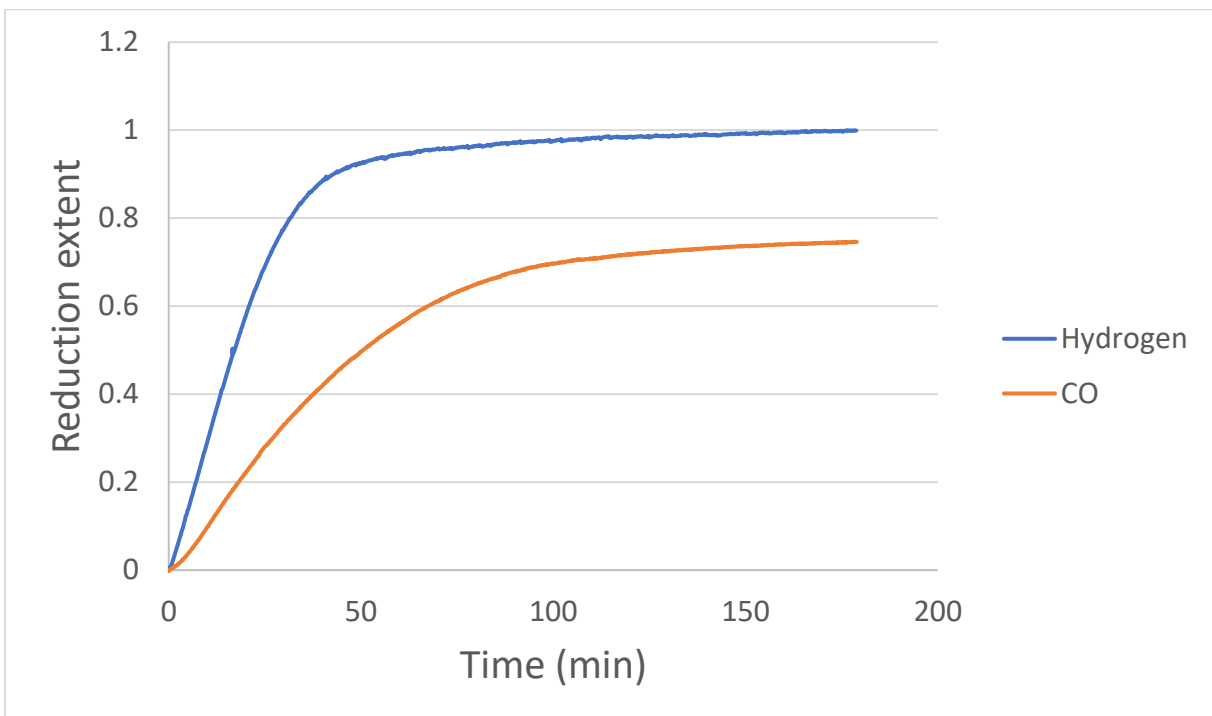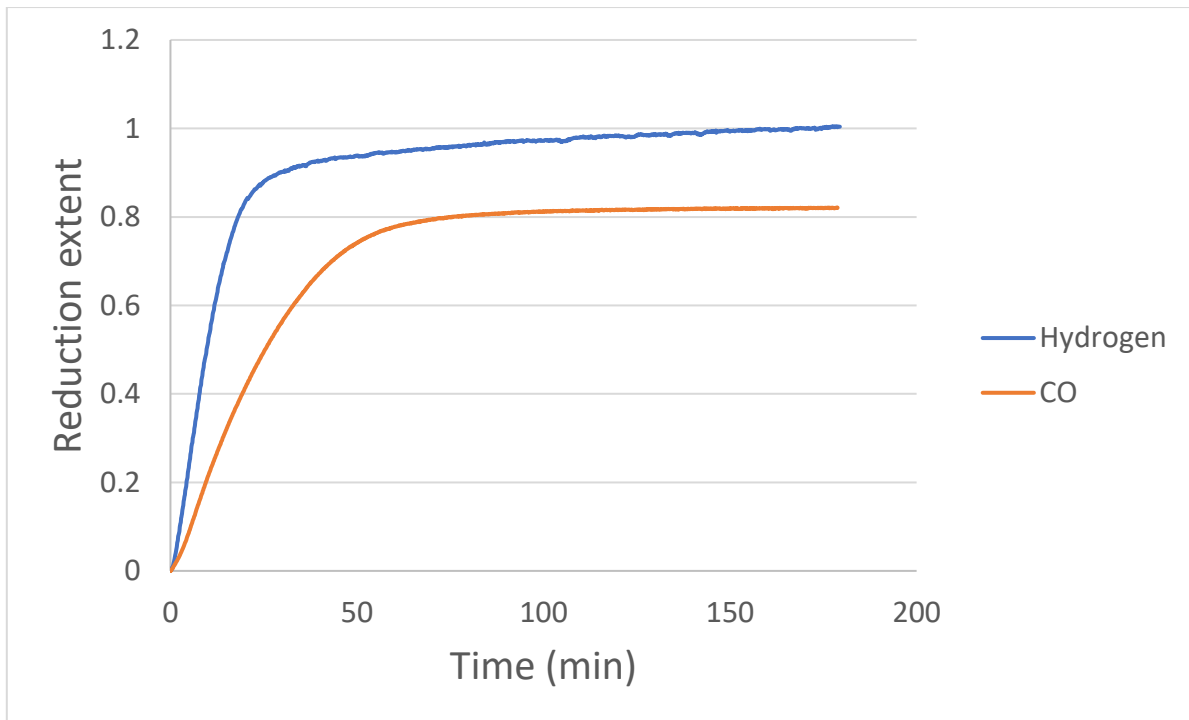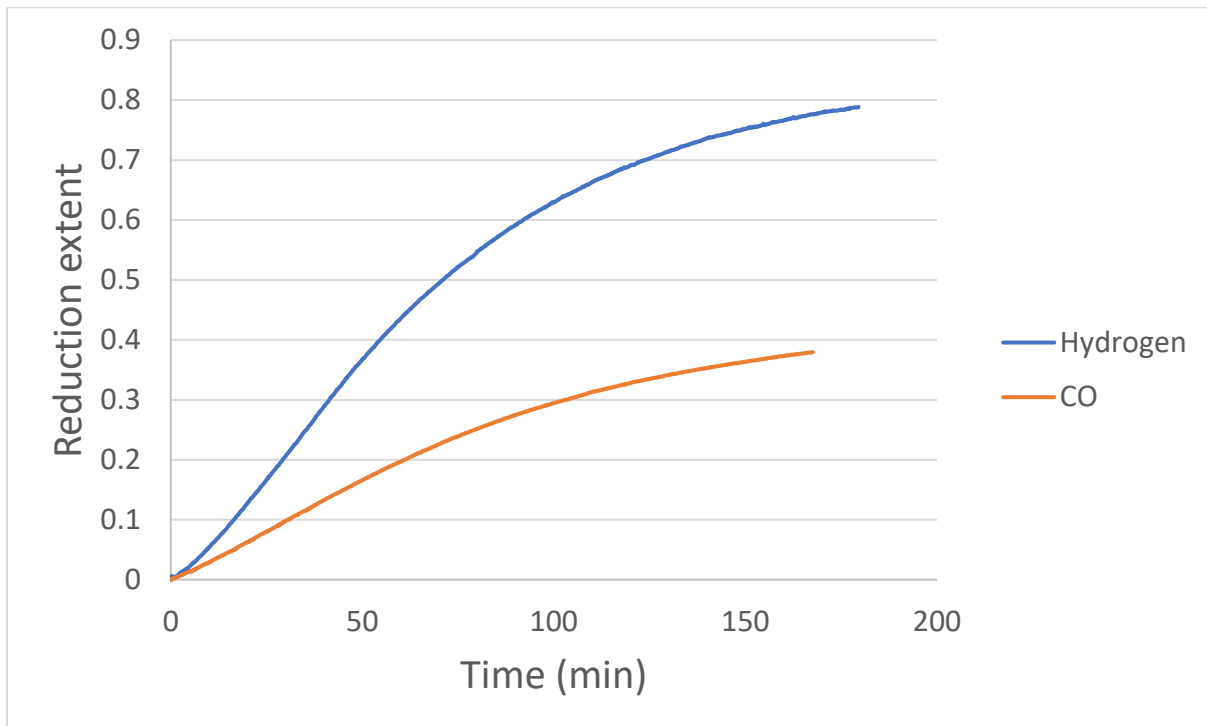

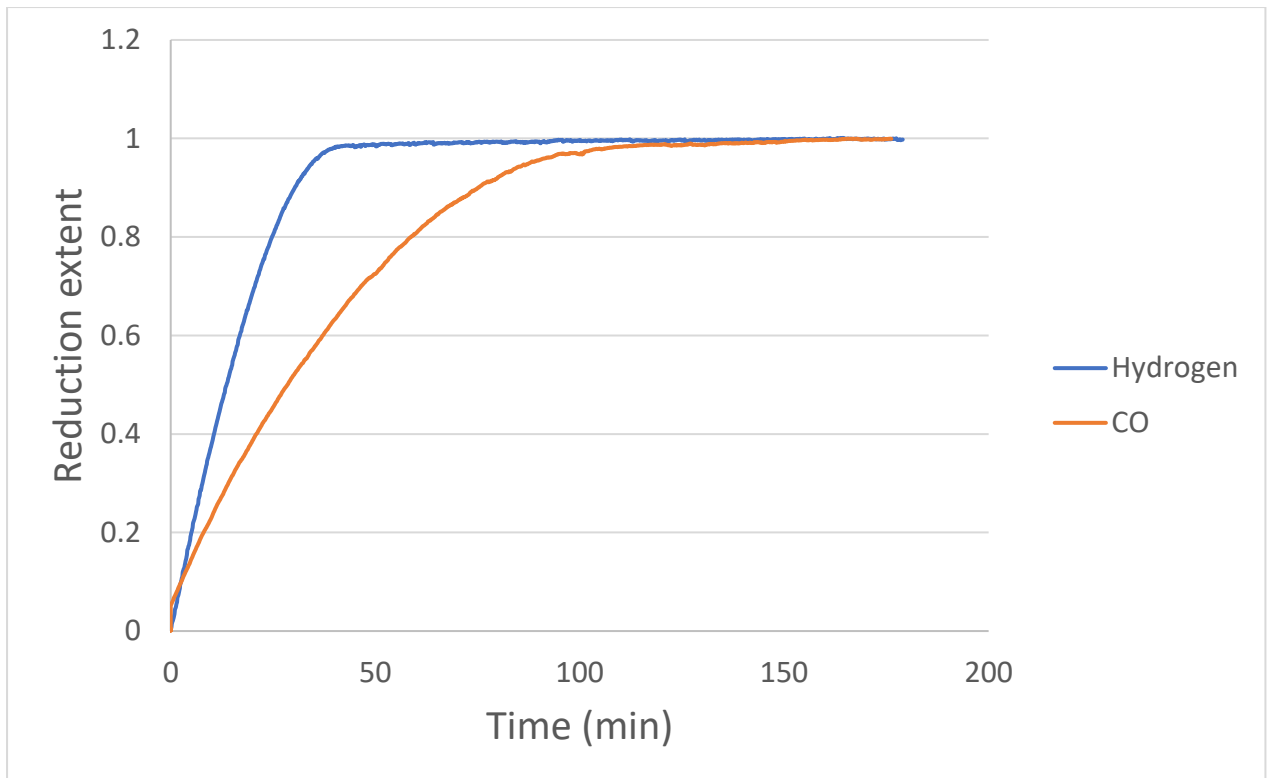*Figure 5.43 - Comparison of H2 and CO reduction at 586°C (859 K) and 20 vol% reductant*

Figure 5.44 - Comparison of H2 and CO reduction at 868°C (1141 K) and 20 vol% reductant

6 Conclusion and further work

The reduction roast – magnetic separation process was investigated for its suitability to upgrade low grade ferruginous manganese ore fines obtained from the Nchwaning mine slimes dam. The process was subject to an optimization study, in which the main variables investigated were temperature and reductant ratio. A kinetic study on the reduction step was also carried out using CO and reductant as well as a separate study using H_2 as reductant.

Nchwaning ore fines were found to have a manganese grade of 44 wt%, which constitutes a high-grade ore, and a Mn/Fe ratio of 3 which is too low for ferromanganese production. The main manganese phases were found to be braunite I and braunite II, with some bixbyite and hausmannite. The main iron phase was hematite and a large amount of calcite was also found.

The main aim of this work was to upgrade the fines to a grade suitable for ferromanganese production, i.e., a manganese content greater than 40 wt% and a Mn/Fe ratio greater than 7,5. The results of the optimization study indicate that this level of upgradation was not possible, with optimum conditions yielding a grade of 47 wt% Mn and a Mn/Fe ratio of 3,7. While the upgrading was not as good as expected, the review metrics; namely Mn/Fe ratio, percentage Fe removed and percentage Mn lost, were still modelled. These models were found to be largely statistically significant. Use of desirability functions also allowed the optimum conditions to be determined. These conditions are temperatures between 850K – 900K and a CO content of the reducing gas between 30 – 35 vol%.

To determine the reasons behind this poor separation between Mn and Fe, SEM imaging was carried out as well as reduction progress tests. SEM EDS elemental maps indicated the presence of solid solution phases. In order to determine the cause of the solid solution phase formation, reduction progress tests were carried out, in which reduction temperature and time were investigated. It was found that temperature and time did not have an effect on the formation of the solid solution phases and their formation is likely due to the mineralogy of the ore itself.

The kinetics of the reduction process was investigated, both with a CO-CO_2 gas mixture and with a H_2-H_2O gas mixture. In the case of CO reduction, it was found that

the Avrami model, which describes nucleation and growth rate limiting reaction, was the best fit to experimental data. For the H_2 reduction is was found that the rate limiting step was activation control. When comparing H_2 and CO reduction, it was found that the reduction rate and extent of reduction reached higher levels with H_2.

Further work

It is believed that the work presented in this study conclusively indicates the lack of suitability of the reduction roast-magnetic separation process to upgrade the specific ore used in this study. It is recommended that an alternative process be investigated. One process that does show some potential is a modified ITmk3 type process. The ITmk3 process is used for the production of iron nuggets. It is believed that a slight modification of this process would yield the iron nuggets and a Mn rich "slag" phase.

7 Bibliography

Aderibigbe, D. A., & Szekely, J. (1981). Studies in coke reactivity: Part 1. Reaction of conventionally produced coke with CO-CO2 mixtures over temperature range 850-1000 C. *Ironmak. Steelmak*, *1*, 11–19.

Ahmed, A., Ghali, S., El-Fawakhry, K., & Eissa, M. (2014). Silicomanganese production utilising local manganese ores and manganese rich slag. *Ironmak. Steelmak*, *41*(4), 310–320.

Allibert, M., Gaye, H., Geiseler, J., Janke, D., Keene, B. J., Kirner, D., Kowalski, M., Lehmann, J., Mills, K. C., Neuschtitz, D., R.Parra, Saint-Jours, C., Spencer, P. J., Susa, M., Tmar, M., & Woermann, E. (1995). *Slag Atlas v15*.

Berg, K. . (1998). *Gaseous Reduction of Manganese Ores*. The Norwegian University of Science and Technology.

Berg, K. L., & Olsen, S. E. (2000). Kinetics of manganese ore reduction by carbon monoxide. *Metallurgical and Materials Transactions B: Process Metallurgy and Materials Processing Science*, *31*(3), 477–490. https://doi.org/10.1007/s11663-000-0154-4

Bhalla, A. (2018). *Hydrocarbon Reduction of Manganese ores*. University of Witwatersrand.

Bloch, D., Feron, J. L., Georges, R., & Jacobs, I. S. (1967). Field-dependent magnetic susceptibility of MnO. *Journal of Applied Physics*, *38*(3), 1474–1475. https://doi.org/10.1063/1.1709674

Bradley, S., Van Gosen, L., & Verplanck, R. (2013). Manganese. *Critical Mineral Resources of the United States—Economic and Environmental Geology and Prospects for Future Supply*. https://pubs.usgs.gov/pp/1802/o/pp1802o.pdf

Chopra, S. (2011). *Antiferromagnetism*. https://www.britannica.com/science/antiferromagnetism

Coetsee, T. (2019). The role of manganese ore reduction morphology development in setting reduction mechanisms. *Minerals Engineering*, *137*(April), 217–231. https://doi.org/10.1016/j.mineng.2019.04.006

David, R. (2004). *Magnetic susceptibility of the elements and inorganic compounds, in Handbook of Chemistry and Physics*. CRC Press.

De Villiers, J. (2020). *Reduction and Subsequent XRD, SEM and XRF Analysis of Wessels Manganese ore Feedstock for Electrolytic Manganese Production*.

Derringer, G., & Suich, R. (1980). Simultaneous Optimization of Several Response Variables. *Journal of Quality Technology, 12*(4), 214–219. https://doi.org/10.1080/00224065.1980.11980968

Dwivedi, D., Singh, N., Sanjay, R., Ranjeet, S., & Jana, K. (2017). An Overview of Manganese Recovery by Hydro and Pyro-Metallurgical Routes. *Journal of The Institution of Engineers (India): Series D, 98*(1), 147–154. https://doi.org/10.1007/s40033-016-0119-7

El-Faramawy, H., Mattar, T., Eissa, M., El-Fawakhry, K., & Ahmed, A. M. (2004). Demanganisation of high manganese pig iron to produce high manganese slag. *Ironmak. Steelmak, 31*(1), 23–30.

El-Geassy, A. ., Nasr, M. ., Yousef, M. A., Khedr, M. H., & Bahgat, M. (2000). Behaviour of manganese oxides during magnetising reduction of baharia iron ore by CO-CO2 gas mixture. *Ironmak. Steelmak, 27*(2), 117–122.

El-Hussiny, N. ., El-Gawad, H. H. ., Mohamed, F. ., & Shalabi, M. E. H. (2015). Pelletization and Reduction of Egyptian Low Grade Manganese Ore Pellets via Hydrogen at 750-950°C. *International Journal of Scientific and Engineering Research, 6*(5), 339–346.

Elliott, R., & Barati, M. (2020). A review of the beneficiation of low-grade manganese ores by magnetic separation. *Canadian Metallurgical Quarterly, 59*(1), 1–16. https://doi.org/10.1080/00084433.2020.1711654

Gao, L., Liu, Z., Chu, M., Wang, R., & Wang, Z. (2018). Upgrading of low-grade manganese ore based on reduction roasting and Upgrading of low-grade manganese ore based on reduction roasting and magnetic separation. *Separation Science and Technology, 54*(1), 195–206. https://doi.org/10.1080/01496395.2018.1504795

Gao, L., Liu, Z., Chu, M., Wang, R., Wang, Z., & Feng, C. (2019). Upgrading of low-

grade manganese ore based on reduction roasting and magnetic separation technique. *Separation Science and Technology (Philadelphia)*, *54*(1), 195–206. https://doi.org/10.1080/01496395.2018.1504795

Gao, L., Liu, Z., Pan, Y., Feng, C., Chu, M., & Tang, J. (2019). Systematic study on separation of Mn and Fe from ferruginous manganese ores by carbothermic reduction roasting process: Phase transformation and morphologies. *Journal of Materials Research and Technology*, *8*(6), 5591–5609. https://doi.org/10.1016/j.jmrt.2019.09.028

Gao, L., Liu, Z., Pan, Y., Feng, C., Ge, Y., & Chu, M. (2020). A study on separation of Mn and Fe from high-alumina ferruginous manganese ores by the carbothermal roasting reduction process. *Advanced Powder Technology*, *31*(1), 51–60. https://doi.org/10.1016/j.apt.2019.09.036

Gao, Y. ., Kim, H. G., & Sohn, H. Y. (2012). Kinetics of pre-reduction of manganese ore by CO. *Mineral Processing and Extractive Metallurgy Review*, *9*(2), 307–311.

Gao, Y., Olivas-Martinez, M., Sohn, H. Y., Kim, H. G., & Kim, C. W. (2012). Upgrading of low-grade manganese ore by selective reduction of iron oxide and magnetic separation. *Metallurgical and Materials Transactions B: Process Metallurgy and Materials Processing Science*, *43*(6), 1465–1475. https://doi.org/10.1007/s11663-012-9731-6

Grant, R. W., Geller, S., Cape, J. A., & Espinosa, G. P. (1968). Magnetic and crystallographic transitions in the Mn2O3-Fe2O3 system. *Physical Review*, *175*(2), 686–695. https://doi.org/10.1103/PhysRev.175.686

Huang, Z., Chai, B., & Yi, L. (2013). Reduction and separation of high iron content manganese ore and its mechanism. *4th Internation Symposium on High Temperature Metallurgical Processes*, 367–375.

Hunt, C. ., Moskowitz, B. ., & Banerjee, S. . (1995). Magnetic Properties of Rocks and Minerals. *Treatise on Geophysics: Second Edition*, *3*, 189–204. https://doi.org/10.1016/B978-0-444-53802-4.00048-8

Ishak, R. J. (2002). *Reaction Kinetics for Reduction of Manganese Ore with Carbon Monoxide in the Presence of Carbon*. Norwegian University of Science and

Technology.

Jun, S., Zhang, H., & Bechhoefer, J. (2005). Nucleation and growth in one dimension. I. The generalized Kolmogorov-Johnson-Mehl-Avrami model. *Physical Review E - Statistical, Nonlinear, and Soft Matter Physics*, *71*(1), 1–8. https://doi.org/10.1103/PhysRevE.71.011908

Kivinen, V., Krogerus, H., & Daavittila, J. (2010). Upgrading of MN /FE ratio of low-grade manganese ore for ferromanganese production. *Proceedings of the 12th International Ferroalloys Congress: Sustainable Future*, 467–476.

Kropáček, V., Krs, M., & Bucha, V. (1975). Magnetic properties of natural Mn-oxides. *Studia Geophysica et Geodaetica*, *19*(3), 261–274. https://doi.org/10.1007/BF01614255

Larssen, T. A. (2020). *Prereduction of Comilog- and Nchwaning-ore* (Issue October). Norwegian University of Science and Technology.

Liu, B., Zhang, Y., Lu, M., Su, Z., Li, G., & Jiang, T. (2019). Extraction and separation of manganese and iron from ferruginous manganese ores: A review. *Minerals Engineering*, *131*(248), 286–303. https://doi.org/10.1016/j.mineng.2018.11.016

Liu, B., Zhang, Y., Wang, J., Wang, J., Su, Z., Li, G., & Jiang, T. (2018a). New understanding on separation of Mn and Fe from ferruginous manganese ores by the magnetic reduction roasting process. *Applied Surface Science*. https://doi.org/10.1016/j.apsusc.2018.02.234

Liu, B., Zhang, Y., Wang, J., Wang, J., Su, Z., Li, G., & Jiang, T. (2018b). New understanding on separation of Mn and Fe from ferruginous manganese ores by the magnetic reduction roasting process. *Applied Surface Science*, *444*(March), 133–144. https://doi.org/10.1016/j.apsusc.2018.02.234

Lui, Y., Lin, Q., Li, L., Fu, J., Zhu, Z., & Wang, C. (2014). Study on hydrometallurgical process and kinetics of manganese extraction from low-grade manganese carbonate ores. *International Journal of Mining Science and Technology*, *24*(4), 567–571.

Meisenheimer, R. G., & Cook, D. L. (1959). Magnetic susceptibility of manganese sesquioxide at temperatures from 4 to 700°K. *The Journal of Chemical Physics*,

30(2), 605–606. https://doi.org/10.1063/1.1730016

MiningTechnology. (2019). *Assmang Manganese Mines, Northern Cape Province, South Africa.*

Mpho, M., Samson, B., & Ayo, A. (2013). Evaluation of reduction roasting and magnetic separation for upgrading Mn/Fe ratio of fine ferromanganese. *International Journal of Mining Science and Technology*, *23*(4), 537–541. https://doi.org/10.1016/j.ijmst.2013.07.012

NS Energy. (2020). *Top five manganese ore mining countries across the globe.* https://www.nsenergybusiness.com/features/manganese-producing-countries/

Pereira, M. J., Lima, M. M. F., & Lima, R. M. F. (2014). Calcination and characterisation studies of a Brazilian manganese ore tailing. *International Journal of Mineral Processing*, *131*, 26–30. https://doi.org/10.1016/j.minpro.2014.08.003

Ratshomo, K. (2011). *South Africa's manganese industry developments*.

Sant, B. R., Parida, K. M., & Kanungo, S. B. (1981). Studies on MnO_2 , -I . Chemical composition, microstructure and other characteristics of some synthetic MnO_2 of various crystalline modifications. *Electrochimica Acta.*, *26*, 435–443.

Schanche, T. L., Mukono, T., Reiersen, H. S., Wallin, M., & Tangstad, M. (2022). Prereduction Behavior of Manganese Ores With Solid Carbon and in CO/CO_2 Gas Atmosphere. In *Metallurgical and Materials Transactions B: Process Metallurgy and Materials Processing Science* (Vol. 53, Issue 5). https://doi.org/10.1007/s11663-022-02611-5

Schrettlea, F., Kant, C., Lunkenheimer, P., Mayr, F., Deisenhofer, J., & Loidl, A. (2012). Wüstite: Electric, thermodynamic and optical properties of FeO. *European Physical Journal B*, *85*(5). https://doi.org/10.1140/epjb/e2012-30201-5

Singh, V. (2020). *Development of a Smelting Reduction Process for Low-Grade Ferruginous Manganese Ores to Produce Valuable Synthetic Manganese Ore and Pig Iron.* 1681–1692.

Singh, V., Chakraborty, T., & Tripathy, S. K. (2020). A Review of Low Grade Manganese Ore Upgradation Processes. *Mineral Processing and Extractive Metallurgy Review*, *41*(6), 417–438.

https://doi.org/10.1080/08827508.2019.1634567

Singh, V., Ghosh, T. K., Ramamurthy, Y., & Tathavadkar, V. (2011). Beneficiation and agglomeration process to utilize low-grade ferruginous manganese ore fi nes. *International Journal of Mineral Processing*, *99*, 84–86. https://doi.org/10.1016/j.minpro.2011.03.003

Singh, V., Reddy, K. V., Tripathy, S. K., Kumari, P., Dubey, A. K., Mohanty, R., Satpathy, R. R., & Mukherjee, S. (2021). A sustainable reduction roasting technology to upgrade the ferruginous manganese ores. *Journal of Cleaner Production*, *284*, 124784. https://doi.org/10.1016/j.jclepro.2020.124784

Suharno, B., Noegroho, A., Ferdian, D., & Nurjaman, F. (2018). *Effect of basicity on ferromanganese production from beneficiated low-grade manganese ore Effect of Basicity on Ferromanganese Production from Beneficiated Low-Grade Manganese Ore. 040002*(January 2017). https://doi.org/10.1063/1.4974423

Szekely, J., Evans, J. ., & Sohn, H. . (1976). *Gas-solid reactions*. Elsevier.

Tang, Q., Zhong, H., Wang, S., Li, J. ., & Liu, G. . (2014). Reductive leaching of manganese oxide ores using waste tea as reductant in sulfuric acid solutions. *Transactions of Nonferrous Metals Society of China*, *24*(3), 861–867.

Towhidi, N., & Szekely, J. (1983). The influence of carbon deposition on the reduction kinetics of commercial grade hematite pellets with CO, H 2, and N 2. *Metallurgical and Materials Transactions B: Process Metallurgy and Materials Processing Science*, *14*(3), 359–367.

Van Deventer, J. S. J. (1988). The effect of catalysts during the carbothermic reduction of manganese dioxide. *Thermochimica Acta*, *125*(C), 107–109. https://doi.org/10.1016/0040-6031(88)87215-0

Welham, N. J. (2002). Activation of the carbothermic reduction of manganese ore. *International Journal of Mineral Processing*, *67*(1–4), 187–198. https://doi.org/10.1016/S0301-7516(02)00045-5

Wellbeloved, D. B., Craven, P. M., & Waudby, J. W. (2000). Manganese and Manganese Alloys. *Ullmann's Encyclopedia of Industrial Chemistry*. https://doi.org/10.1002/14356007.a16_077

Wills, B. (2016). *Wills' Mineral Processing Technology* (8th ed.). Elsevier Ltd.

Zhang, W., & Cheng, C. Y. (2007). Manganese metallurgy review. Part I: Leaching of ores/secondary materials and recovery of electrolytic/chemical manganese dioxide. *Hydrometallurgy*, *89*(3–4), 137–159. https://doi.org/10.1016/j.hydromet.2007.08.010

Zhang, Y., Du, M., Liu, B., Su, Z., Li, G., & Jiang, T. (2017). Separation and recovery of iron and manganese from high-iron manganese oxide ores by reduction roasting and magnetic separation technique. *Separation Science and Technology (Philadelphia)*, *52*(7), 1321–1332. https://doi.org/10.1080/01496395.2017.1284864